ARC RATE PREDICTIONS AND FLIGHT DATA ANALYSIS FOR THE SOLAR ARRAY MODULE PLASMA INTERACTIONS EXPERIMENT (SAMPIE)

by

Carmen Perez de la Cruz

S.B. Aeronautics and Astronautics
Massachusetts Institute of Technology, Cambridge, 1993

Submitted to the Department of
Aeronautics and Astronautics in Partial Fulfillment of
the Requirements for the
Degree of

MASTER OF SCIENCE in
Aeronautics and Astronautics
at the
Massachusetts Institute of Technology
June 1995

Signature of Author ______________________________
Department of Aeronautics and Astronautics
May 12, 1995

Certified by ______________________________
Professor Daniel E. Hastings, Thesis Supervisor
Department of Aeronautics and Astronautics

Accepted by ______________________________
Professor Harold Y. Wachman, Chairman
Department Graduate Committee

ARC RATE PREDICTIONS AND FLIGHT DATA ANALYSIS FOR THE SOLAR ARRAY MODULE PLASMA INTERACTIONS EXPERIMENT (SAMPIE)

Submitted to the Department of Aeronautics and Astronautics
on June, 1995 in partial fulfillment of the
requirements for the Degree of Master of Science in
Aeronautics and Astronautics

The increasing demand for high power systems may require that these systems operate at high voltages. The operation of solar cells at high negative voltages in the ionospheric plasma, however, may lead to arcing. Analytical and numerical models of the arcing process have been developed and show excellent agreement with previous experimental data. Using these models the arcing activity for the conventional cells in NASA's Solar Array Module Plasma Interactions Experiment (SAMPIE) and the Japanese Space Agency ISAS' High Voltage Solar Array (HVSA) experiment were predicted. Comparisons between the experimental and predicted arc rates for the SAMPIE experiment showed excellent agreement. Analysis of the SAMPIE flight data, along with the computer simulations, was conducted to examine the relationships between the arcing rate and the various solar cell properties, environmental variables, and solar cell parameters. No cell temperature dependence could be supported by the data, but a possible critical ion flux and critical neutral density is implied. The dependence of arc rate on voltage was fitted using a power law, an exponential form, and a form suggested by the analytical model. The last two fits showed an onset voltage supported by the data. The coefficients from these fits could not be interpreted physically, but they could be scaled with ion flux and electron work function to give accurate arc rates at the new conditions.

Acknowledgements

I must first thank my thesis advisor, Professor Hastings, who has always believed in me. Thanks for all the encouragement and support.

I'd also like to thank Dale Ferguson who patiently answered all my phone calls regarding the SAMPIE experiment.

Thanks to all my friends at the SSPL lab: Graeme, Derek, Guy, Jim, Mike, and Folusho who have made my past two years very enjoyable and entertaining. Karen, my partner in crime, I wish you the best of luck. I am especially thankful to Jim for all the white chocolates which made me smile countless times and for being always there for me. Mark, thanks for the sanity check.

Mom and Dad thanks for giving me the opportunity to pursue my dreams and for always being there for me. Nacho, thanks for being Nacho. Thanks to Cristina for all those chocolate hugs and kisses, and to David for giving me the solar cell kit so I could learn about solar cells.

Aoy thanks for being the best friend anyone could have. I'll miss you.

This work has been sponsored by NASA Lewis Research Center. I would like to thank Dale Ferguson and Barry Hillard for supplying me with the invaluable data from the SAMPIE experiment and Dr. Kuninaka and Dr. Cho for providing the information for the HVSA experiment.

Contents

List of Figures

List of Tables

List of Symbols

A	Fowler Nordheim coefficient ($1.54 \times 10^{-6} \times 10^{4.52\phi_W^{-1/2}}/\phi_W$ A/V^2)
B	Fowler Nordheim coefficient ($6.53 \times 10^9 \phi_W^{1.5}$ V/m)
C_{diele}	capacitance of dielectric (F/m^2)
C_{front}	capacitance of coverglass front surface (F)
d	thickness of dielectric (m)
d_1	thickness of coverglass (m)
d_2	thickness of adhesive (m)
d_{gap}	gap distance between cathode and anode (m)
d_i	distance of electron first impact point from triple junction (m)
d_o	overhang distance of coverglass (m)
d_o^c	critical overhang distance of coverglass (m)
E_e	electric field at emission site (V/m)
E_i	electron incident energy on dielectric plate (eV)
E_{max}	electron incident energy for maximum secondary electron yield (eV)
E_{TJ}	electric field at triple junction (V/m)
E_1	electric field of coverglass (V/m)
E_2	electric field of adhesive (V/m)
j_{ec}	electron current density from conductor (A/m^2)
j_{ee}	secondary electron current density from dielectric (A/m^2)
j_{FN}	Fowler-Nordheim current density from the conductor (A/m^2)
j_{id}	ion ram current density to the dielectric (A/m^2)
n_e	plasma number density (m^{-3})
n_{es}	emission site number density (m^{-2})
m_e	electron mass (kg)
m_i	ion mass (kg)
$\dot{R}$	arc rate (sec^{-1})
r_s	sheath radius (m)
S_{FN}	emission site area determined from F-N plot (m^2)

S_{real}	emission site area determined by accounting for electron space charge effects (m^2)
T_e	electron temperature (eV)
T_i	ion temperature (eV)
V_{arc}	voltage at which last arc occurred V
V_{bias}	bias voltage of interconnector/conductor V
V_e	voltage which minimizes arcing time V
V_i	initial voltage before solar cell charging V
v_{ion}	mean speed of ions entering sheath (m/sec)
v_x	electron velocity in the x direction (m/sec)
v_y	electron velocity in the y direction (m/sec)
y	distance of emission site from the triple junction (m)
β	field enhancement factor
ΔQ	charge lost from one coverglass by one discharge (C)
ϵ_{d_1}	relative dielectric constant of coverglass
ϵ_{d_2}	relative dielectric constant of adhesive
$\mathcal{E}_1$	energy at $\gamma_{ee} = 1$ (eV)
ϕ_c	potential of conductor (V)
ϕ_i	potential of coverglass-adhesive interface (V)
ϕ_w	work function (eV)
γ_{ee}	secondary electron yield
γ_{max}	maximum secondary electron yield at normal incidence
η	factor accounting for difference in electric field at emission site and triple junction
θ_i	incident impact angle of electron onto the dielectric surface
σ	surface charge density (C/m^2)
τ_{arc}	time between arcs (sec)
τ_{efee}	EFEE charging time (sec)
τ_{ion}	ion charging time (sec)
τ_{exp}	experiment time (sec)
ξ	factor accounting for difference of dielectric constants between coverglass and adhesive

Chapter 1

Introduction

The power system chosen for a space mission depends upon the mission duration and objectives. For short time and low energy requirements, the best power systems are electrochemical systems such as fuel cells, but for missions with power requirements in the range of 0.1 W to 100 kW, photovoltaic power is the most commonly used power system. Currently, most of these systems operate at low voltage levels, typically 28 V. Future missions may require these systems to be operated at higher power levels, in the range of 10 kW to 1 MW. To meet these requirements the systems may be operated at high voltage levels or high current levels. Operation at high voltage levels is preferred for two reasons. The first is that the resistive loss during power transmission for a given power system is lower when the power system operates at high voltages rather than high currents. The second reason is that the mass of the distribution cables will be reduced by distributing the power at high voltages rather than high currents. Thus, power distribution at high voltage levels is desired. In this research, the term high voltage is used to refer to voltages with an absolute value higher than 100 V. Proposed systems range from -160 V for the International Space Station Alpha to thousands of volts for orbital transfer vehicles using solar electric propulsion.

A schematic of a conventional solar cell is shown in Fig. 1.1. The coverglass protects the semiconductor (the solar cell) from the radiation environment. Adhesive is used to bond the coverglass, semiconductor, and substrate. Metal interconnectors allow the current to flow between adjacent cells. The required voltage is attained by connecting the cells in series and the required power level is attained by placing these strings of cells in parallel.

As seen in Fig. 1.1, conventional solar cells will have some part of the metallic interconnector exposed to the environment. This design choice allows the arrays to be flexible and to thermally expand or contract when entering or leaving eclipse. The metallic interconnector, along with other surfaces of the spacecraft which allow the passage of current, will collect current from the space plasma. The charge accumulated by the spacecraft must satisfy

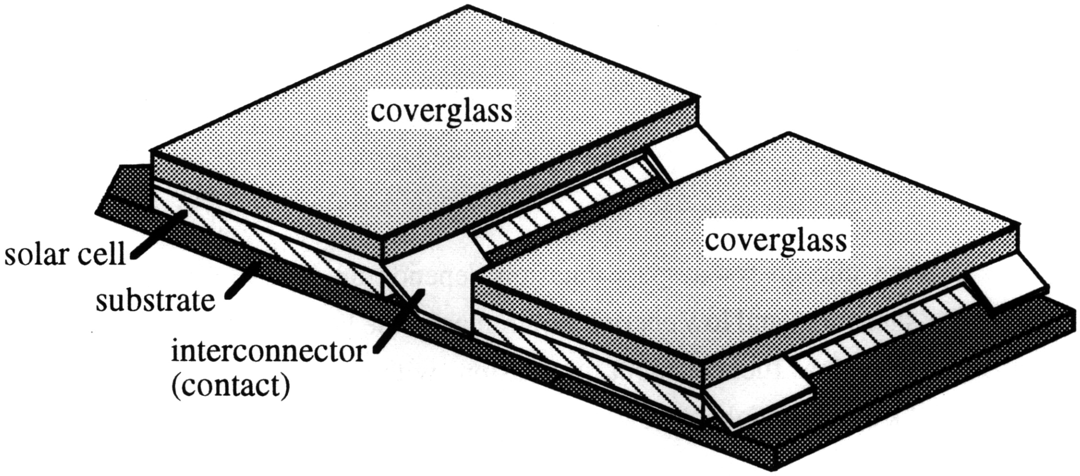

Figure 1.1: Schematic of a Conventional Solar Cell

$$\frac{\partial \rho}{\partial t} + \nabla \cdot \vec{j} = 0, \tag{1.1}$$

derived from Gauss' law and Ampere's law. In steady state, the net current collected by the spacecraft is zero. Hence, to satisfy this condition, some of the surfaces in the spacecraft will be negatively biased and collect ions and the rest will be positively biased and collect electrons. Because the mass of an electron is much smaller than the mass of an ion, the electron current collected by a positively biased surface will be much larger than the ion current collected by the same surface if negatively biased at a comparable voltage. Thus, to satisfy the zero net current condition, most of the surfaces of the spacecraft, including the solar arrays, will float negatively with respect to the plasma. For example, major parts of the Space Station are expected to float at approximately -130 V relative to the plasma [3], which is close to the maximum operational voltage, -160 V.

High voltage solar arrays have been found to interact with the ambient plasma in several detrimental ways, resulting in operational inefficiencies. When positively biased, arrays can collect an anomalously large current, a phenomenon known as "snapover". For large voltages this may lead to a significant leakage power loss [42]. When the cells are operated at large negative voltages, arc discharges may occur. An arc is defined as a sudden current pulse up to an order of an ampere lasting a few microseconds or less. It is often accompanied

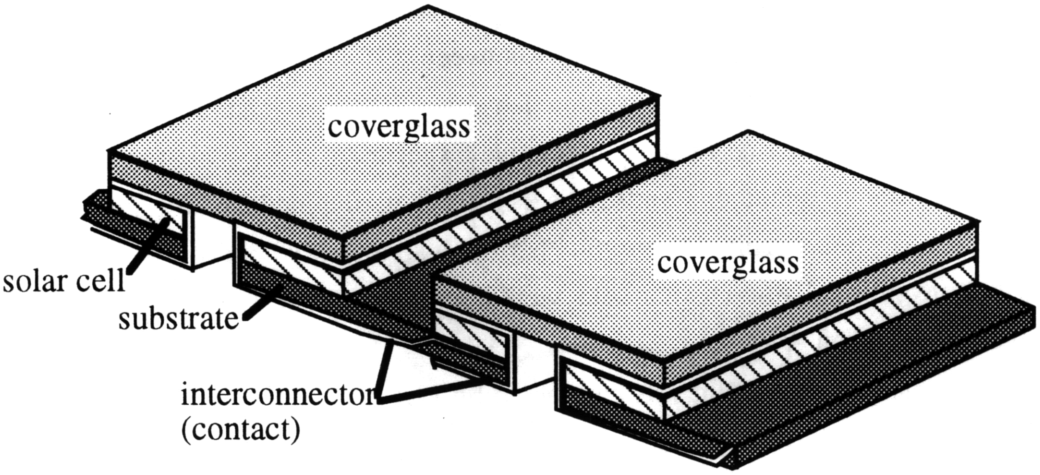

Figure 1.2: Schematic of a Wrap-Through-Contact Solar Cell

by a flash of light at the edge of the coverglass. These arc discharges may give rise to electromagnetic interference (EMI), enhance the local plasma density, and cause damage to the solar cell. Lastly, high accelerated ions will collide with the arrays and give rise to enhanced drag on the spacecraft [14].

To eliminate the interaction between the conducting surfaces and the ambient plasma, these surfaces may be covered with an insulator. This is the principle behind the design of a new type of solar cell, the wrap-through-contact (WTC) solar cell, developed by NASA for the Space Station [44]. A schematic of this type of cell is shown in Fig. 1.2. The interconnectors of these cells are no longer exposed to the plasma but instead pass underneath the substrate and connect to the middle of adjacent cells under the coverglasses. However, in this new design, the semiconductor is still exposed to space along the edge of the cell. Even if all conducting surfaces were to be covered, the problem is not permanently solved. While in orbit, cracks may develop due to severe thermal cycles or particulates striking the insulating surfaces and again leave some parts of the interconnector or semiconductor exposed.

1.1 Background

1.1.1 Space and Ground Experiments

Arcing on high voltage solar arrays has been observed in both ground and space experiments. The first observation of arcing on solar cells in a plasma chamber was made by Herron et al. [18] in 1971. The solar cells were biased between ±16 kV and arcing was observed at bias voltages as low as -6 kV with a plasma density of 10^8 m^{-3}. The occurrence of arcs in space was verified by the first Plasma Interactive Experiment (PIX I) [12] in 1978. PIX I, flown as an auxiliary payload on Landsat 3's Delta rocket, obtained data for a period of four hours in a 920 km polar orbit. During this period, a solar array consisting of twenty four 2cm×2cm conventional silicon solar cells were biased to ±1000 V. Arcing was observed at voltages greater than -750 V.

A more extensive experiment was conducted by PIX II in 1983. A more sophisticated version of PIX I, PIX II was also flown as an auxiliary payload on a Delta launch vehicle into a 900km polar orbit. In this experiment the solar array consisted of five hundred conventional silicon cells again biased to ±1000V. Arcing was observed at voltages as low as -255V. A few problems were encountered when interpreting the flight data. Unexpected tumbling of the spacecraft placed the Langmuir probe in the spacecraft wake, making the Langmuir probe readings unreliable. Furthermore, if an arc occurred at high voltages, the power supply was often shut down for the rest of the data taking cycle. The data from the PIX II flight and ground tests was studied by Ferguson [7], who concluded that the arc rate $\dot{R}$ was directly proportional to the plasma density. Ferguson obtained the following relationship where the arc rate varies with bias voltage in a power law fashion given by

$$\dot{R} = 1.4 \times 10^{-10} \, (-V)^{3.093} \left(\frac{n}{6.3 \times 10^3} \right) \tag{1.2}$$

for the flight data, and

$$\dot{R} = 1.82 \times 10^{-18} \, (-V)^{5.51} \tag{1.3}$$

in ground tests at high density, with a mean plasma density of 1.5×10^4 cm^{-3}, where V is the bias voltage and n is the plasma density in cubic centimeters.

Other ground experiments offer some insight on the characteristics of the arcing phenomenon. Experiments conducted by Miller [30], Kuninaka [25], and Fujii et al. [11] confirm that the presence of a dielectric material near a biased conductor is essential for arcing to occur. Fujii et al. [11] tested three metallic samples under the same plasma conditions. The two samples that were covered with 200 μm thick fused silica, simulating a coverglass, arced at voltages as low as -450 V. The third sample without a coverglass did not show arcing until -1000 V when the arcing occurred at the substrate. In the wrap-through-contact cells, where the conductive surfaces have been shielded from the plasma, the arcing threshold observed in ground experiments ranged from -210 V to -457 V with respect to the plasma potential [33].

In an experiment conducted by Snyder [37], the potential just over the coverglass surface was measured. Before an arc occurred the potential was near the plasma potential, but when an arc occurred the potential dropped significantly, on the order of a hundred volts. In a different experiment, Snyder et al. [38] observed current emission after the plasma source was no longer in operation. Inouye and Chaky [22] observed that the current emitted from the solar array sample during arcing was greater that the value expected from photoemission.

Several experimental observations have led to qualitative relationships between the arcing rate and different parameters. Many experiments have shown that the arcing rate decreases as the experiment continues, suggesting that the surface conditioning affects the arcing rate. Kuninaka [24] varied the temperature of the array from 100°C to 500°C and observed that the arc rate decreased as the temperature increased. Leung [27] observed that the wrap-through-contact cells arced less than the conventional cells. Upschulte et al. [45] observed that overhanging the coverglass over the adhesive by 10$\sim$20μm, somewhat shielding the interconnector, suppressed the arcing activity considerably.

1.1.2 Arcing Onset Models

There are two different types of theoretical models which offer an explanation of the arcing onset mechanism. The first, proposed by Parks et al. [34] based on the previous work of Jongeward et al. [23], attributes the arcing onset to the Malter [29] effect at a thin dielectric layer on the conductor surface. The second, proposed by Cho and Hastings [4] based on previous work of Hastings et al. [16], attributes the arcing onset to a discharge in the neutral gases desorbed from the dielectric surface.

The arcing mechanism proposed by Parks et al. [34] is described by the following sequence:

(1) A dielectric impurity layer is formed on the conductor surface.
(2) Ions attracted to the negatively biased conductor are accumulated on the dielectric layer and enhance the electric field in the layer.
(3) Fowler-Nordheim field emission causes electrons to be emitted from the conductor into

the dielectric.

(4) The emitted electrons have ionization collisions while being accelerated within the dielectric, leaving positive charges behind as they are emitted from the dielectric-vacuum interface.

(5) The remaining positive charge further enhances the electric field within the dielectric layer.

(6) The resulting rate of change of the electric field in the insulating layer is given by a combination of Gauss' Law and Ampere's Law,

$$\epsilon\frac{d}{dt}(\epsilon_r E_{m-d} - E_{d-v}) = j_i + j_{m-d}e^{\alpha_d d_d}P_{d-v} - j_{m-d}, \tag{1.4}$$

where ϵ_r is the dielectric constant of the insulating layer, E_{m-d} is the electric field in the dielectric layer, E_{d-v} is the ambient electric field at the dielectric-vacuum interface, j_i is the ion current density, α_d is the ionization rate per unit distance inside the layer, d_d is the dielectric layer thickness, P_{d-v} is the probability that the electrons are emitted from the dielectric-vacuum interface, and j_{m-d} is the Fowler-Nordheim emission current at the metal-dielectric interface which is given by

$$j_{m-d} = AE_{m-d}^2 e^{-\frac{B}{E_{m-d}}}, \tag{1.5}$$

where A and B are the Fowler-Nordheim emission coefficients are given by

$$A = \frac{1.54 \times 10^{-6} 10^{4.52/\sqrt{\phi_w}}}{\phi_w}(A/V^2), \tag{1.6}$$

$$B = 6.53 \times 10^9 \phi_w^{1.5}(V/m), \tag{1.7}$$

where ϕ_w is the work function of the metal in eV.

If the factor $e^{\alpha_d d_d}P_{d-v}$ is greater than unity, a positive feedback mechanism is created at the metal-dielectric interface, leading to a runaway of the field and the emission current by increasing E_{m-d} monotonically in time.

The arcing onset mechanism proposed by Cho and Hastings [4] modeled the geometry of a conventional cell as shown in Fig. 1.3. The dielectric consists of the coverglass and the adhesive. The conductor is the interconnector between the cells which connects the adhesive-solar cell interface to the substrate-solar cell interface of the adjacent cell. Since the voltage drop across the actual solar cell is much lower than that across the dielectric, the solar cell has not been included in the model. Through the use of computer particle simulations, the above system was used to study the arc initiation process at the triple

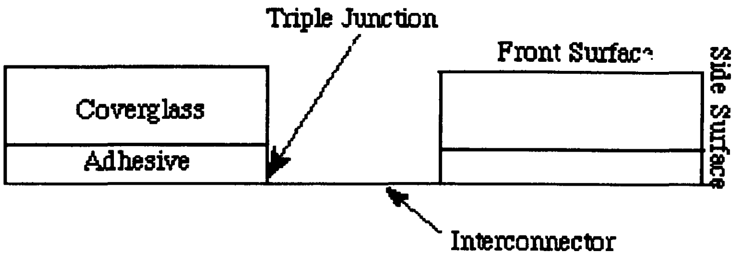

Figure 1.3: Model of the Conventional Solar Array Used for Numerical Simulations

junction, the point where the dielectric, conductor and plasma meet. The arcing onset mechanism that resulted form the numerical simulations is illustrated in Fig. 1.4 and is described by the following sequence:

(1) Ambient ions, attracted by the negatively biased conductor, charge the dielectric front surface (parallel to the conductor), but leave the side surface effectively uncharged.
(2) As the potential of the front surface approaches zero, a strong electric field, given by E=V/d (where V is the bias voltage and d the dielectric thickness), is set up between the triple junction and the front surface.
(3) This strong electric field, aided by field enhancement at sites in the conductor surface, induces a pre-breakdown enhanced field electron emission (EFEE) current showing the characteristic of the Fowler-Nordheim emission current shown in Eqn. 1.5. In addition, electrons are also released due to the bombardment of the conductor surface by the ambient ions.
(4) Some of the emitted electrons strike the side surface of the dielectric causing the release of secondary electrons and the electron stimulated desorption of neutrals adsorbed on the dielectric surface. If the secondary electron yield is greater than unity and the electrons have an escape path, the side surface charges up positively, providing a positive feedback mechanism to further enhance the electric field at the conductor surface.
(5) As the electric field increases, the electron emission current increases until it is limited by the negative space charge of the emitted electrons.
(6) Once the neutral density becomes high enough, ionization begins due to collisions between electrons and neutrals.
(7) If the neutral density is very high, Townsend breakdown occurs as proposed by Hastings et al. [16]. Even if the density is not high enough for Townsend breakdown to

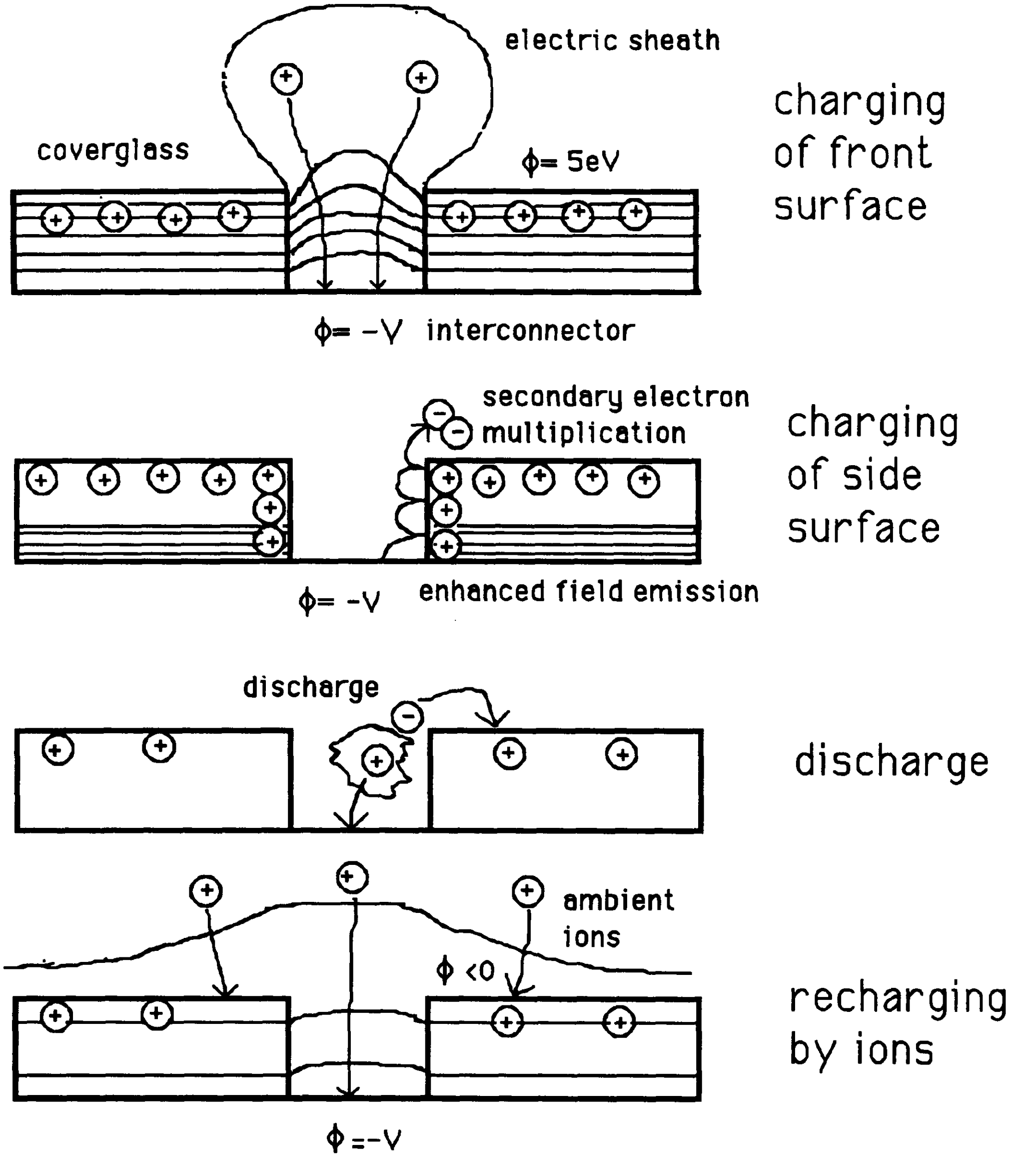

Figure 1.4: Arcing Sequence of a High Voltage Solar Array

occur, breakdown is still possible if the positive ion space charge can cancel the negative electron space charge and enhance the field at the conductor.

(8) The arcing time is the minimum of the sum of the ion and EFEE charging times for all the emission sites on the conductor.

(9) A discharge wave created by the arc resets the charging process at all of the emission sites within the area covered by the wave.

Cho [4] suggested several possible mitigation strategies. Among them was to hide the triple junction from the plasma by causing the coverglass to overhang over the adhesive and solar cell. Numerical simulations conducted by Cho [4] and Mong [31] showed that the EFEE charging time increased dramatically, resulting in a decrease in the arcing rate. The numerical results showed that the first impact point of the electrons emitted from the conductor will be in the back surface of the coverglass. The secondary electrons emitted from the back surface cannot escape because the coverglass is blocking their trajectories. The accumulation of these electrons will decrease the potential of the back surface and consequently lower the electric field at the triple junction. When electrons begin to hit the adhesive, they release secondary electrons which leave the side surface positively charged. The electric field at the triple junction then begins to increase. However, this increase in the electric field at the triple junction was found to occur at a much later time compared to the one for the conventional geometry. Mong [31] derived an expression for the critical overhang distance, such that overhangs greater than this length will decrease the arcing activity dramatically.

1.2 Recent Flight Experiments

Three recent flight experiments have been designed to study the interaction of high voltage solar arrays with the plasma environment. In these experiments, different solar cells, space materials, and arc mitigation strategies were tested. The Solar Array Module Plasma Interactions Experiment, SAMPIE, was developed by the National Aeronautics and Space Administration (NASA). SAMPIE was among the experiments flown in the payload bay of the Space Shuttle Columbia in March, 1994. The shuttle placed itself in a circular orbit at a 39° inclination and a 300 km altitude. The Photovoltaic Array Space Power Plus Diagnostics (PASP Plus) experiment, is the primary experiment on the Advanced Photovoltaic and Electronics Experiments (APEX) satellite. This satellite is part of the Space Test Program (STP) of the Air Force's Space and Missiles Center. Launched in August, 1994, this experiment will operate from one to three years. The satellite was placed in a 355 × 2544 km orbit at a 70° inclination, thus allowing the solar cells to be exposed to a large range of the space plasma, neutral, and radiation environments. Lastly, the High Voltage Solar Array (HVSA) experiment, developed by the Institute of Space and Astronautical Sciences (ISAS) is integrated as one of the eleven experiments conducted on the first flight of the Space Flyer Unit (SFU). SFU was launched in the Japanese H-II rocket on March, 1995, injected into a 486 km altitude and 28.5° inclination orbit, and retrieved by the Space Shuttle after six months of operation.

1.3 Overview of This Research

In the future, solar arrays may be chosen to satisfy high power requirements. To save mass and reduce the resistive losses, the solar arrays may be operated at high voltages rather than high currents. Yet, when solar arrays are biased to high negative voltages, the current collecting surfaces interact with the plasma environment, leading to operational inefficiencies. The occurrence of arcs will degrade the solar array performance and produce electromagnetic interference which may affect nearby instruments. Cho and Hastings [4, 15] developed a semi-analytical model based on the numerical and theoretical work to predict the arcing rates for a solar array given the environmental parameters. This model has predicted arc rates that showed a good agreement with the data for ground experiments and PIX II flight data.

The objectives of this research are the following

1. To use the semi-analytical model to predict the arc rates for the SAMPIE and HVSA flight experiments and assess its agreement with the experimental data.
2. To determine the correlations between arcing rate and the various material properties, environmental variables and experimental parameters as suggested by the model by using the flight data from the SAMPIE experiment .

In Chapter 2, the semi-analytical model for the conventional geometry cells developed by Cho and Hastings is reviewed and a possible mechanism through which WTC cells arc is presented. In Chapter 3, the SAMPIE and HVSA experiments are described. The arc rates predicted for these experiments, obtained using the semi-analytical model, are shown in Chapter 4. In Chapter 5, the flight data obtained from the SAMPIE experiment is analyzed. Finally, conclusions are made about the arcing behavior of the different cells and the validity of the model to predict the arcing activity.

Chapter 2

Numerical and Semi-Analytical Models

Cho and Hastings developed a semi-analytical code based on the numerical simulation of their proposed arcing onset mechanism for conventional geometry cells, shown in Fig. 1.4. The code predicts the arcing activity for a given solar array using parameters chosen from probability distribution functions obtained from numerical simulations using a particle-in-cell (PIC) code. The semi-analytical code was then modified by Soldi and Hastings [39] to model the physics more accurately and to include experimental limitations. This chapter will review the semi-analytical formulas in the current code and describe a proposed arcing mechanism for the WTC cells.

2.1 Semi-Analytical Model for Conventional Cells

When an arc occurs, some of the stored charges on the coverglass are lost. Experimentally it has been observed that during the arc discharge, the potential of the coverglass drops by a few hundred volts from its steady state value of about +5 volts [37]. Since the electric field at the triple junction also drops during the arc discharge, the field emission ceases to charge the coverglass and the lost charge will be restored through ambient ions. When sufficient charge is restored, the electric field becomes high enough to restart the enhanced electron field emission (EFEE) charging of the dielectric until the next discharge occurs.

The numerical results have shown that the critical condition for arcing onset after EFEE charging has been initiated is whether the desorbed neutral density is larger than the critical value of approximately 6×10^{21} m^{-3} [4]. If the neutral density is above this value, a breakdown occurs and this mechanism is labeled as a "big arc." Big arcs are typically seen as current pulses on the order of amps. The surface discharge wave created from the breakdown will expand radially away from the arc spot. Assuming that the wave front is expanding semispherically, the expansion speed of the wave front v_d is inversely proportional to the area covered by the wave. Therefore, $v_d = c_0/{r_{dis}}^2$ where r_{dis} is the radius of the wavefront.

From a fit to experimental measurements, the c_0 coefficient was found to be 6.0 [4]. Thus, assuming a maximum arc duration of 10 μs the discharge wave can cover an area of 0.01 m^2. The charging processes in the sites within the discharge wave area, also known as the area of correlation, will be reset.

If the density is below the critical value, the electron current just becomes space charge limited and will eventually relax without leading to a breakdown. In this case, a very short current pulse would be seen, without an arc flash or arc damage. This current pulse, referred to as a "small arc", will not create a discharge wave. Thus the charging processes within the correlated area will not be affected until another "big arc" occurs. Results from numerical simulations showed that the current seen from a small arc is on the order of microamps to a few milliamps. For experiments such as SAMPIE and HVSA, the minimum current levels detectable by equipment are 20 mA and 300 mA respectively. Consequently, only the occurrence of big arcs would be recorded by these experiments.

In the simulations, the total area of the array is divided into correlated areas and the arcing rates in each correlated area are calculated independently of each other. The arc rates in each correlated area are then summed to obtain the total arc rate for the solar array. The arcing rate is obtained by dividing the number of arcs with currents above the threshold by the experiment time.

From the above discussion, the time between big arcs, τ_{arc}, is the minimum charging time of all the sites on the conductor within a correlated area which satisfy the critical condition for arcing onset and is given by

$$\tau_{arc} = \min(\tau_{ion} + \tau_{efee}), \tag{2.1}$$

where τ_{ion} is the time during which the ions restore the lost charge in the dielectric and τ_{efee} is the enhanced field electron emission charging time. In this section the semi-analytical formulas for the EFEE charging time, ion charging time, total charging time, and the breakdown condition will be reviewed. A detailed derivation of these formulas can be found in Ref. [4].

2.1.1 EFEE Charging Time

The geometry considered for EFEE charging is shown in Fig. 2.1. The dielectric surface is charged by $j_{ec}(y)$, the electron emission current emitted from location y on the conductor and $j_{ee}(x)$, the secondary electron current density emitted from location x. The rate of change of the surface charge density on the dielectric surface is given by

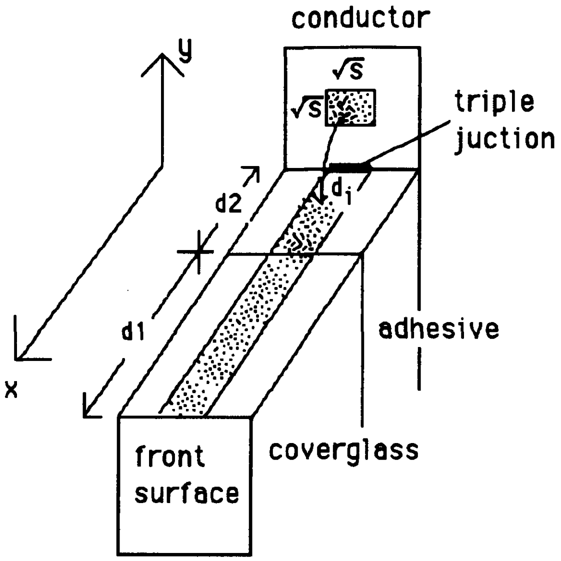

Figure 2.1: Geometry for EFEE charging

$$\frac{d\sigma(x,t)}{dt} = -\int P(x,y,t)j_{ec}(y,t)dy - \int P(x,x',t)j_{ee}(x',t)dx' + j_{ee}(x,t) \tag{2.2}$$

where $P(x,y,t)$ is the probability that an electron emitted from location y to $y+dy$ on the conductor will hit the dielectric surface in the range x to $x+dx$ and $P(x,x',t)$ is the probability that an electron emitted from location x' will hit at location x. The secondary electron current at each location x is given by

$$j_{ee}(x,t) = \int \gamma_{ee}(x,y)P(x,y,t)j_{ec}(y,t)dy + \int \gamma_{ee}(x,x')P(x,x',t)j_{ee}(x',t)dx' \tag{2.3}$$

where $\gamma_{ee}(x,y)$ is the secondary electron yield at location x due to the electrons emitted from the point y. The rate of change of the surface charge density at the first impact point, $x = d_i$, is calculated by integrating Eqn. 2.2 neglecting the contribution of secondary electrons which yields

$$\frac{d\sigma}{dt} = (\gamma_{ee} - 1)j_{ec}\frac{\sqrt{S_{real}}}{d_i} \tag{2.4}$$

where S_{real} is the area of the emission site at the dielectric vacuum interface. The electric field at the triple junction, $x = 0$, can be expressed as

$$E_{TJ} = \xi\frac{\phi_d}{d_i} = \xi\frac{\sigma}{C_{diele}d_i} \tag{2.5}$$

where ϕ_d is the potential between the first impact point and the triple junction, C_{diele} is the capacitance of the front surface and the factor ξ is introduced to account for the discontinuity of the electric field due to the difference in the dielectric constants of the adhesive and coverglass. If the first impact point of the emitted electrons on the dielectric surface is within the adhesive, $d_i < d_2$, then ξ is unity. If the impact point is within the coverglass, then ξ is given by

$$\xi = \left[\frac{d_2}{d_i} + \frac{\epsilon_{d_2}}{\epsilon_{d_1}}\frac{(d_i - d_2)}{d_i}\right]^{-1}. \tag{2.6}$$

The electric field at an emission site in the conductor, E_e, will differ from the value at the triple junction, E_{TJ}. The numerical simulations revealed that the difference was only a function of the distance from the site to the triple junction and the factor η was introduced to account for this difference. Thus, the electric field at the emission site is given by

$$E_e = \eta E_{TJ} = \eta\xi\frac{\sigma}{C_{diele}d_i} \tag{2.7}$$

Substituting Eqn. 2.7 into Eqn. 2.4 results in

$$\frac{dE_e}{dt} = \eta\xi\frac{(\gamma_{ee} - 1)\sqrt{S_{real}}}{C_{diele}d_i^2}j_{ec} \tag{2.8}$$

The current emitted from an emission site in the conductor surface is described by

$$j_{ec} = A\frac{S_{FN}}{S_{real}}\beta^2 E_e^2 \exp(-\frac{B}{\beta E_e}), \tag{2.9}$$

the Fowler-Nordheim expression for field emission due to dielectric inclusions on the conductor's surface. The factor S_{FN}/S_{real} has been introduced to account for the negative space charge effect near the emission site. S_{real} is the emission site area on the conductor surface and S_{FN} is chosen to obtain the same current observed in experiments. A and B are the Fowler-Nordheim coefficients given by Eqns. 1.6 and 1.7. The term β is the electric field enhancement factor assigned to the emission site and has been introduced to adjust for the observation of experimental emission currents at applied fields typically 100 to 1000 times smaller than those predicted by the Fowler-Nordheim expression. The field enhancement is attributed to manufacturing defects or impurities on the interconnector surface. Microprotusions on the surface can lead to an enhancement factor in the order of a hundred while a dielectric layer formed on the metal surface can yield enhancement factors in the order of a thousand. The value of β is not measured since it is a costly and difficult process. Therefore, in order to model the variation of the conductor surface, the semi-analytical code assumes a distribution of β values. The β value for an emission site is chosen randomly from a distribution of values between 1 and 2000, with an average value of 200.

The resulting rate of change of the electric field at an emission site on the conductor, E_e is given by

$$\frac{dE_e}{dt} = \eta\xi\frac{(\gamma_{ee}-1)\sqrt{S_{real}}}{C_{diele}d_i^2}A\frac{S_{FN}}{S_{real}}\beta^2E_e^2\exp\left(-\frac{B}{\beta E_e}\right). \qquad (2.10)$$

The values of η, d_i, and C_{diele} are functions only of y. The following formulas were calculated from polynomial fits of the numerical results. η is given by

$$\eta = 1 + \sum_{n=1}^{n=4} a_n((\bar{y}-1)^{2n}-1), \qquad (2.11)$$

where $\bar{y} = y/(d_{gap}/2)$, y is the distance from the emission site to the triple junction, and d_{gap} is the interconnector length. ξ_0 is the value of ξ with $d_i = d_1 + d_2$.The first impact point, d_i is given by

$$\frac{d_i}{d} = \sum_{n=1}^{n=4} b_n\left(\frac{y}{d}\right)^{\frac{1}{2n}} \qquad (2.12)$$

where $d = d_1 + d_2$. The capacitance per unit area of the dielectric side surface, $C_{diele}(d_i)$ is determined from a fifth order polynomial fit to the results of a capacitance matrix scheme [21]. In such scheme the change in the surface potential $\delta\phi_{s,j}$ due to a unit charge σ_i placed at a gridpoint on the dielectric is calculated by solving the Poisson equation, $\nabla^2\delta\phi_{s,j} = \delta_{i,j}$. Repeating this process for all the gridpoints on the dielectric, yields a matrix relating the potential at a gridpoint on the dielectric surface and the charge density at any other point on the dielectric surface. Inverting this matrix, a matrix of capacitances is obtained and the coefficients c_n result from a fifth order polynomial fit to the diagonal entries of this matrix.

$$\frac{C_{diele}(d_i)}{C_{norm}} = \frac{1}{\sum_{n=1}^{n=6} c_n\left(\frac{d_i}{d}\right)^{n-1}} \qquad (2.13)$$

where C_{norm} is the capacitance per unit area of the front surface

$$C_{norm} = \frac{1}{\frac{d_1}{\epsilon_{d_1}} + \frac{d_2}{\epsilon_{d_2}}} \qquad (2.14)$$

The value of γ_{ee}, the secondary electron yield, is also a function of y and is given by Ref. [13] as

$$\gamma_{ee} = \gamma_{max}\frac{E_i}{E_{max}}\exp\left(2 - 2\sqrt{\frac{E_i}{E_{max}}}\right)\exp[2(1-\cos\theta_i)]. \qquad (2.15)$$

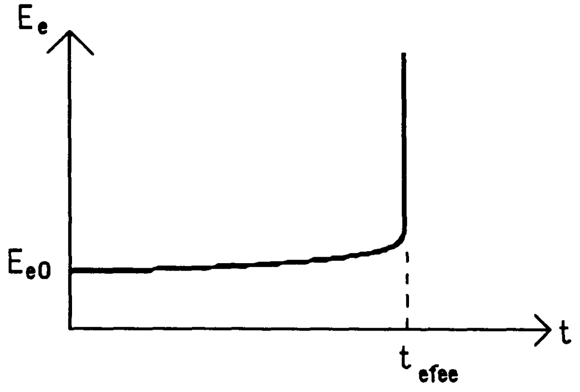

Figure 2.2: Typical Electric Field Run-Away

where γ_{max} is the maximum secondary electron yield at normal incidence and E_{max} is the electron incident energy for the maximum secondary electron yield. E_i is the incident energy of the emitted electrons impacting the dielectric surfaces and is given by

$$E_i = e\phi_d = \frac{E_{TJ} d_i}{\xi} = \frac{\xi_0}{\xi} V \frac{d_i}{d} \tag{2.16}$$

and θ_i, the incident angle of those electrons at the first impact site, is given by

$$\theta_i = \arctan\left(\frac{d_i}{y}\right). \tag{2.17}$$

If the secondary electron yield γ_{ee} is assumed to be constant, Eqn. 2.10 can be integrated, yielding an electric field $E_e(t)$ with the characteristic shape shown in Fig. 2.2 and given by

$$E_e(t) = \frac{E_{e_o}}{1 + \frac{\beta E_{e_o}}{B} ln\left(1 - \exp(-\frac{B}{\beta E_{e_o}})(\frac{B}{\beta})Ct\right)}, \tag{2.18}$$

where C is the constant given by

$$C = \eta\xi \frac{(\gamma_{ee} - 1)\sqrt{S_{real}}}{C_{diele} d_i^2} A \frac{S_{FN}}{S_{real}} \beta^2 \tag{2.19}$$

and E_{e_o} is the initial electric field at the electron emission site on the interconnector.

The theoretical run-away time for a constant secondary electron yield, $t = \tau_{efee}$, is derived by setting the denominator in Eqn. 2.18 to zero. Thus, the field emission electron charging time τ_{efee} is given by

$$\begin{aligned} \tau_{efee} &= \frac{1 - \exp(-\frac{B}{\beta E_{e_o}})}{\exp(-\frac{B}{\beta E_{e_o}})} \left(\frac{B}{\beta}\right) C && (2.20) \\ &\simeq \frac{\beta}{B} \exp\left(\frac{B}{\beta E_{e_o}}\right) \frac{1}{C} && (2.21) \end{aligned}$$

$$= \frac{C_{diele} d_i^2}{(\gamma_{ee} - 1)\sqrt{S_{real}}\eta\xi A \frac{S_{FN}}{S_{real}} B\beta} \exp\left(\frac{B}{\beta E_{e_o}}\right). \tag{2.22}$$

The initial electric field at the emission site E_{e_o} can be expressed in terms of the potential difference between the coverglass front surface and the triple junction as

$$E_{e_o} = \eta \frac{V}{d} \xi_0. \tag{2.23}$$

Thus, τ_{efee} is given by

$$\tau_{efee}(V) = \frac{C_{diele} d_i^2}{(\gamma_{ee} - 1)\sqrt{S_{real}}\eta\xi A \frac{S_{FN}}{S_{real}} B\beta} \exp\left(\frac{Bd}{\beta\eta\xi_0 V}\right). \tag{2.24}$$

The implicit assumption in this analysis is that the secondary electron yield is greater than unity. If the yield is less than unity, positive charging of the dielectric side surface will not occur and the field will not run away. Cho also showed that even when taking into to account the angle of incidence, the incident energy which gives $\gamma_{ee} = 1$ will be about twenty electron volts. Therefore, as long as the voltages considered are in the order of a hundred volts, the secondary electron yield will remain above one.

Hence, the parameters that affect the EFEE charging time are the secondary electron yield, the capacitance of the side surface, the constants associated with the Fowler-Nordheim current, the parameters of the emission site, the first impact point on the dielectric surfaces, and the bias voltage. The coefficients A and B are only determined by the surface work function, ϕ_w and as noted above d_i, η, ξ, and C_{diele} are only functions of y. For a given geometry, the independent parameters which affect the EFEE charging time are only y, S_{real}, S_{FN}, β, and V_e. In the numerical code, γ_{ee} is not assumed to be constant and therefore τ_{efee} must be calculated numerically from Eqn. 2.10. However, in the data analysis γ_{ee} is assumed to be constant and τ_{efee} is given by Eqn. 2.24.

2.1.2 Ion Charging Time

The ion charging time is the time during which the ambient ions restore the lost charge of the front surface after an arc has occurred. If an arc occurs when the potential difference between the front surface and conductor is V_a and the coverglass front surface loses charge ΔQ, then the potential difference drops to $V_a - \Delta Q / C_{front}$, where C_{front} is the capacitance of the front surface given by

$$C_{front} = \frac{1}{d_1/(A_{cell}\epsilon_{d_1}) + d_2/(A_{cell}\epsilon_{d_2})}. \tag{2.25}$$

The ambient ion charging time for the voltage to recover to the value V_e is then given by

$$\tau_{ion} = \frac{[V_e - (V_a - \frac{\Delta Q}{C_{front}})]C_{front}}{e n_e v_{ion} A_{cell}} \tag{2.26}$$

where v_{ion} is the mean speed of the ions entering the sheath and $e n_e v_{ion}$ is the ion flux to the coverglass front surface of area A_{cell}. For ground experiments v_{ion} is given by $\bar{c}/4$ where $\bar{c} = \sqrt{\frac{8T_i}{\pi m_i}}$. For flight experiments it is given by the component of the orbital velocity onto the dielectric front surface, $v_{ion} = v_{orbit} \sin\alpha$ where α is the angle of attack of the arrays to the ram direction (at angle of attack of 90^o the spacecraft velocity vector and the vector normal to the solar cell's front surface are parallel).

2.1.3 Total Charging Time

When an arc occurs, the coverglass is recharged by ions and the electric field at the triple junction increases. The EFEE process may start whenever the surface of the conductor feels a strong enough electric field. The total charging time for each emission site is determined numerically by finding the value of V_e that minimizes $\tau_{chrg} = \tau_{ion} + \tau_{efee}$. The total charging time as a function of V_e for a constant secondary electron yield is shown in Fig. 2.3 where $\tau_0(V_e)$ is the premultiplier in Eqn. 2.24. Substituting the EFEE and ion charging time equations in Eqn. 2.1 the following expression for the time between arcs is obtained

$$\tau_{chrg} = \frac{(V_e - (V_{arc} - \frac{\Delta Q}{C_{front}}))C_{front}}{e n_e v_{ion} A_{cell}} + \frac{C_{diele} d_i^2}{(\gamma_{ee} - 1)\sqrt{S_{real}}\,\eta\xi A \frac{S_{FN}}{S_{real}} B\beta} \exp\left(\frac{Bd}{\beta\eta\xi_0 V_e}\right) \tag{2.27}$$

This expression assumes that the time during which the neutrals are ionized is short and therefore it can be neglected.

2.1.4 Breakdown Condition

Once the electric field has run away, the breakdown criterion must be judged. Flashes of light observed in experiments on high voltage solar array arcing indicate that arcing is a fairly localized phenomenon, confined near the interconnector and the coverglass. Therefore the breakdown occurs in a length scale less than a millimeter. The product of the outgassed neutral density and this length scale, d, gives values which fall in the semi-vacuum region between the Townsend breakdown region, where the ionization mean free path Λ_{mfp} is smaller than the path length d, and the vacuum breakdown region where $\Lambda_{mfp} \gg d$. Cho used the hypothesis of Boyle, Kisliuk, and Germer [2] to explain the

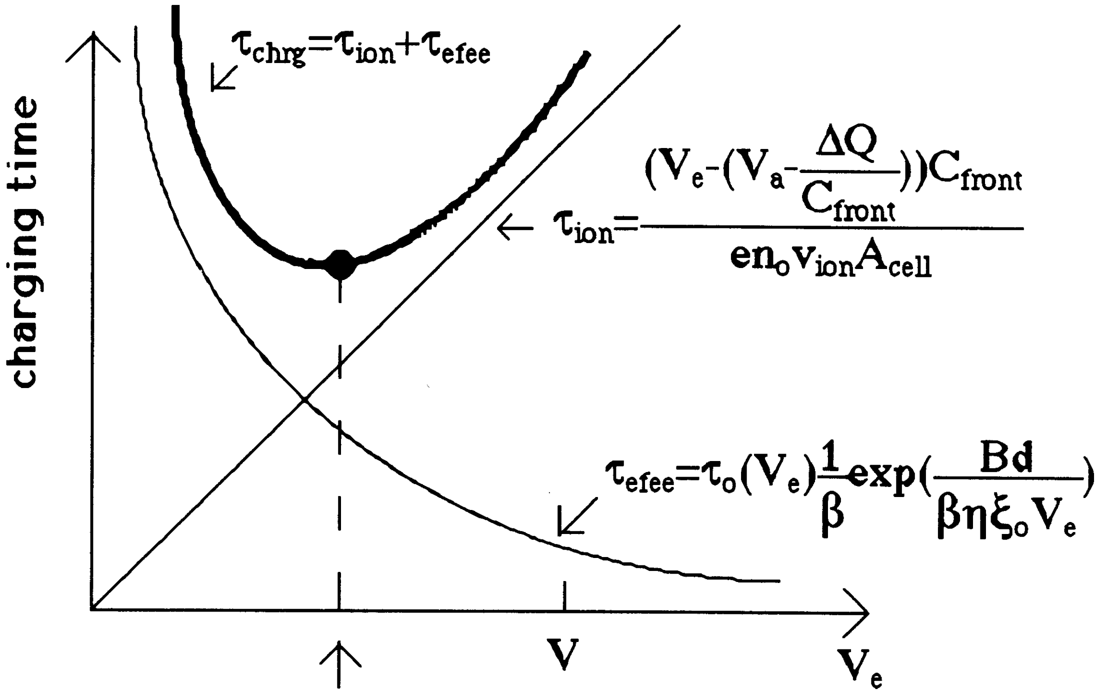

EFEE charging begins when the voltage between the triple junction and the cover-glass front surface recovers to this value.

Figure 2.3: Minimum Total Charging Time

mechanism of gas breakdown in this intermediate region. From this theory and numerical results, a critical neutral density, n_{n_c}, above which the positive ion space charge balances the increase of negative space charge, was determined to be approximately 6×10^{21} m^{-3}. Therefore breakdown occurs at a site if the desorbed neutral density n_n at the site is greater than the critical neutral density n_{n_c}. The desorbed neutral density at each emission site is given by [4] by

$$n_n = 2.08\frac{N_n Q_{ESD}}{\bar{c}}\frac{\epsilon_0}{e}\sqrt{\frac{2e}{m_e}}\frac{\sqrt{E_{se}}}{E_{se1}d^2}V_e^2 \tag{2.28}$$

where N_n is the adsorbed neutral density on the dielectric surface before the intensive outgassing due to the EFEE begins, Q_{ESD} is the electron stimulated desorption cross section, ϵ_0 is the dielectric constant of vacuum, e is the electron charge, m_e is the electron mass, E_{se} is the secondary electron energy in eV, E_{se1} is the energy for a secondary electron yield of unity, d is the dielectric thickness, $d = d_1 + d_2$, and $\bar{c}$ is the average speed of the desorbed neutrals. These neutrals are assumed to be at the temperature of the dielectric surface T_s, so that

$$\bar{c} = \sqrt{\frac{8\kappa T_s}{\pi m_n}} \tag{2.29}$$

where m_n is the mass of the neutrals (assumed to be water). The rate of change in the adsorbed neutral density N_n is calculated by the difference between the thermal stimulated desorption of neutrals and the flux of ambient neutrals onto the dielectric surface. N_n can be calculated by solving the following equation

$$\frac{dN_n}{dt} = \left(\Gamma_n + n_{na}\frac{\bar{c}}{4}\right)\left(1 - \frac{N_n}{N_{n0}}\right) - k_1^0 N_n \exp\left(-\frac{E_D}{\kappa T_s}\right), \tag{2.30}$$

where k_1^0 is the neutral thermal desorption coefficient, E_D is the adsorption energy, n_{na} is the ambient neutral density, and N_{n0} is the neutral surface density for monolayer coverage of the surface. The term $1 - N_n/N_{n0}$ is an approximation for the probability that a neutral striking the surface will stick and Γ_n is the component of the neutral flux to the side surface due to the orbital velocity given by

$$\Gamma_n = n_{na}v_{orbit}\cos\alpha, \tag{2.31}$$

with v_{orbit} being the orbital velocity and α the angle of attack of the arrays to the ram. The surface neutral density, as a function of time, is therefore given by

$$N_n(t) = \frac{C_1}{C_2}\left(1 - e^{-C_2 t}\right) \tag{2.32}$$

where C_1 and C_2 are given by

$$C_1 = \Gamma_n + n_{na}\frac{\bar{c}}{4} \tag{2.33}$$

$$C_2 = \frac{C_1}{N_{n0}} + k_1^0 \exp\left(-\frac{E_D}{\kappa T_s}\right). \tag{2.34}$$

Substituting Eqn. 2.32 in Eqn. 2.28 the steady state critical ambient neutral density, n_{na_c}, required for arcing onset can be derived and is given by

$$n_{na_c} = \frac{k_1^0 \exp(\frac{E_D}{\kappa T_s})}{(2.08\frac{Q_{ESD}}{n_{n_c}\bar{c}}\frac{\epsilon_0}{e}\sqrt{\frac{2e}{m_e}}\frac{\sqrt{E_{se}}}{E_{se1}d^2}{V_e}^2 - \frac{1}{N_{n0}})(\bar{c}/4 + V_{orbit}\cos\alpha)} \tag{2.35}$$

This density is a function of the cell temperature, voltage, electron stimulated desorbtion cross section Q_{ESD}, angle of attack, dielectric thickness and the secondary emission properties of the dielectric. Thus, for a given cell, voltage and value of Q_{ESD} and orientation, the critical ambient density required for breakdown can be determined for various cell temperatures. For example, the maximum steady state critical ambient neutral density needed for breakdown at typical bias voltages used in the SAMPIE experiment for silicon cells in the ram orientation is shown Fig. 2.4. The value of Q_{ESD} chosen for the curves, 10^{-19} m^2, was chosen to agree with the value of ESD yield, $N_n Q_{ESD}$, recorded in numerous measurements [6]. As seen in Fig. 2.4, the ambient neutral density needed to allow breakdown is a strong function of the cell temperature. The curves indicate that for a given cell temperature there is a critical ambient neutral density above which breakdown will occur. Similarly, for a given ambient neutral density, there exists a cell temperature above which no arcing will occur.

Using the semi-analytical model, the arcing rates may be calculated for conventional geometry cells. To calculate arc rates, the solar array area is divided into a finite number of correlated areas. For each emission site in the conductor, parameters are chosen randomly from distribution functions. The enhancement factor β is chosen assuming a distribution function $f(\beta) = f_o\exp(-\beta/\beta_o)$, where f_o is determined from the normalization condition $\int f(\beta)d\beta = 1$ and β_o is a constant which determines the shape of the distribution. The values of S_{real} and S_{FN} are chosen so that $\log_{10}S_{real}$ and $\log_{10}S_{FN}$ are uniformly distributed and encompass the range of experimentally measured values. In each correlated area, the arc size and time at which an arc occurs is recorded. The site with a big arc with the minimum charging time will be the one that arcs. The number of small arcs that took place before this time are counted, since these do not reset the charging process. The process is then repeated until the time exceeds the experiment time. The number of arcs whose current exceeds the

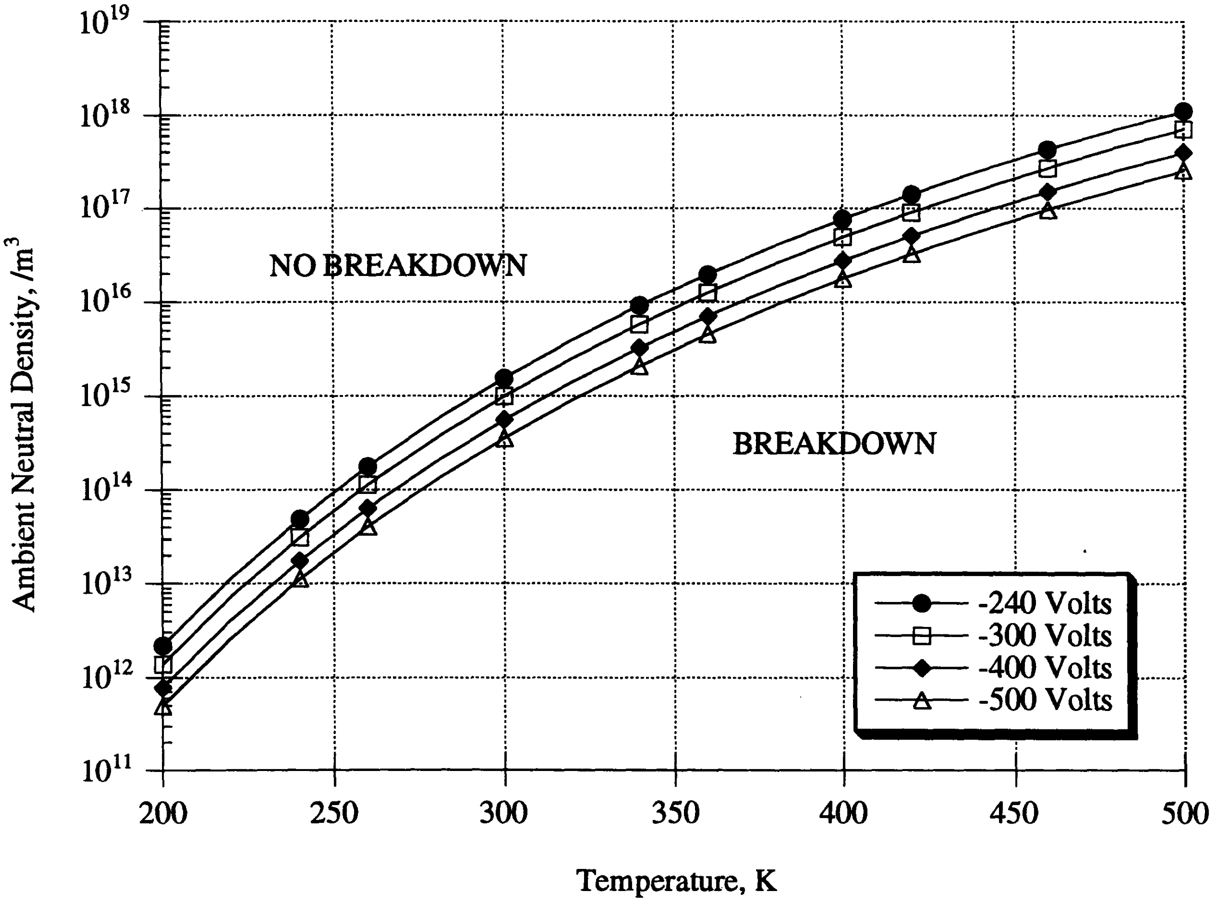

Figure 2.4: Critical Ambient Neutral Density Variation with Temperature

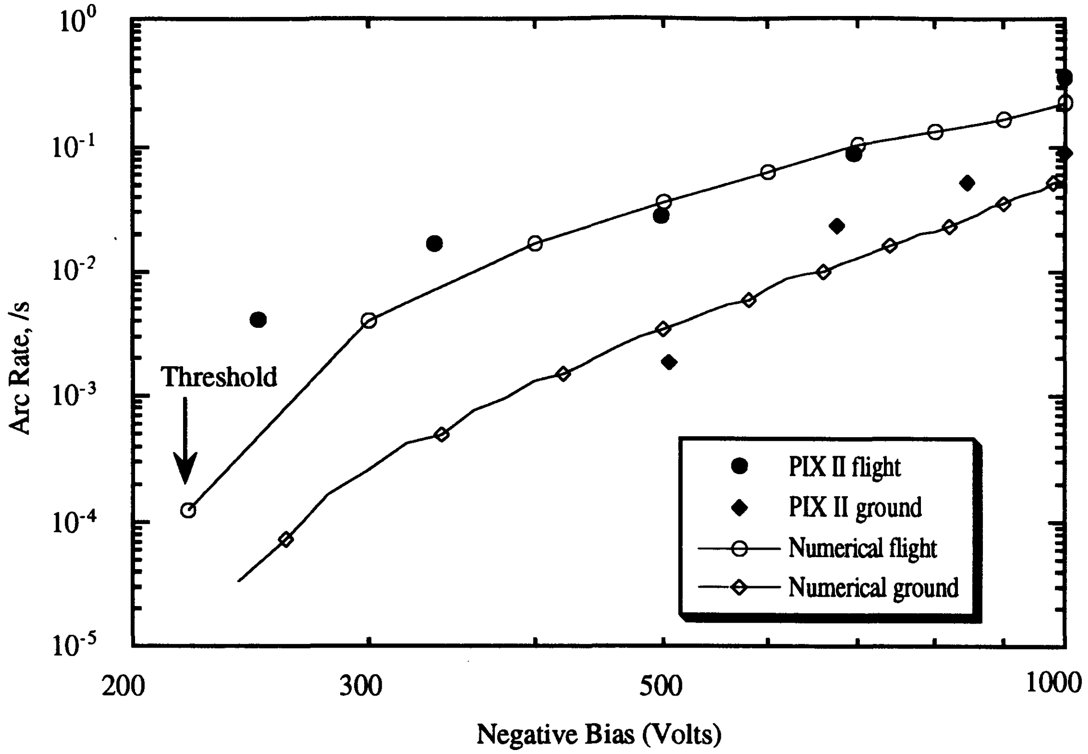

Figure 2.5: PIX II Experimental Data and Numerical Results

experiment current threshold is then divided by the experiment time to yield the arc rate. Because of the random selection of the parameters from the distribution functions, different arc rates are obtained each time the experiment is simulated. Simulating the experiment one hundred times gives the maximum, minimum, and average expected arc rates for the experiment. Cho and Hastings used this procedure to calculate the arc rate numerically for the PIX II ground and flight experiments. The results showed excellent agreement with the experimental data, as shown in Fig. 2.5.

2.2 Proposed Arcing Mechanism for WTC Cells

As discussed in the introduction, the new WTC cells differ from the conventional geometry cells in that their interconnectors are not exposed to the ambient plasma but are imbedded underneath the substrate. The purpose of this new geometry is to eliminate the current emitted from the conductor, thus hindering the arcing process. However, these cells have been observed to arc during ground experiments [33]. In this design, a semiconductor (the solar cell) is exposed to the ambient plasma along the edge of the cell, as seen in Fig. 1.2, and may aid to the arcing process. A mechanism through which WTC cells arc has been proposed by Font [10]. This arcing mechanism is illustrated in Fig. 2.6 and can be summarized as follows:

(1) The ambient ions charge the front of the coverglass and the substrate between the cells. The region of the substrate immediately adjacent to the cell is charged to a significant positive potential by the ions, creating a large electric field near the junction of the cell and the substrate.

(2) The electric field becomes significantly large to induce the enhanced field electron emission (EEFE) from the solar cell. Due to the potential structure in the gap, the emitted electrons will strike the substrate causing the release of secondary electrons and the electron stimulated desorption of neutrals adsorbed on the substrate's surface.

(3) The secondary electrons will be unable to climb the potential well and will remain in the vicinity of the substrate. When the neutral density is sufficiently large, ionization and arcing will take place if the electrons do not become space charge limited and halt the EFEE emission.

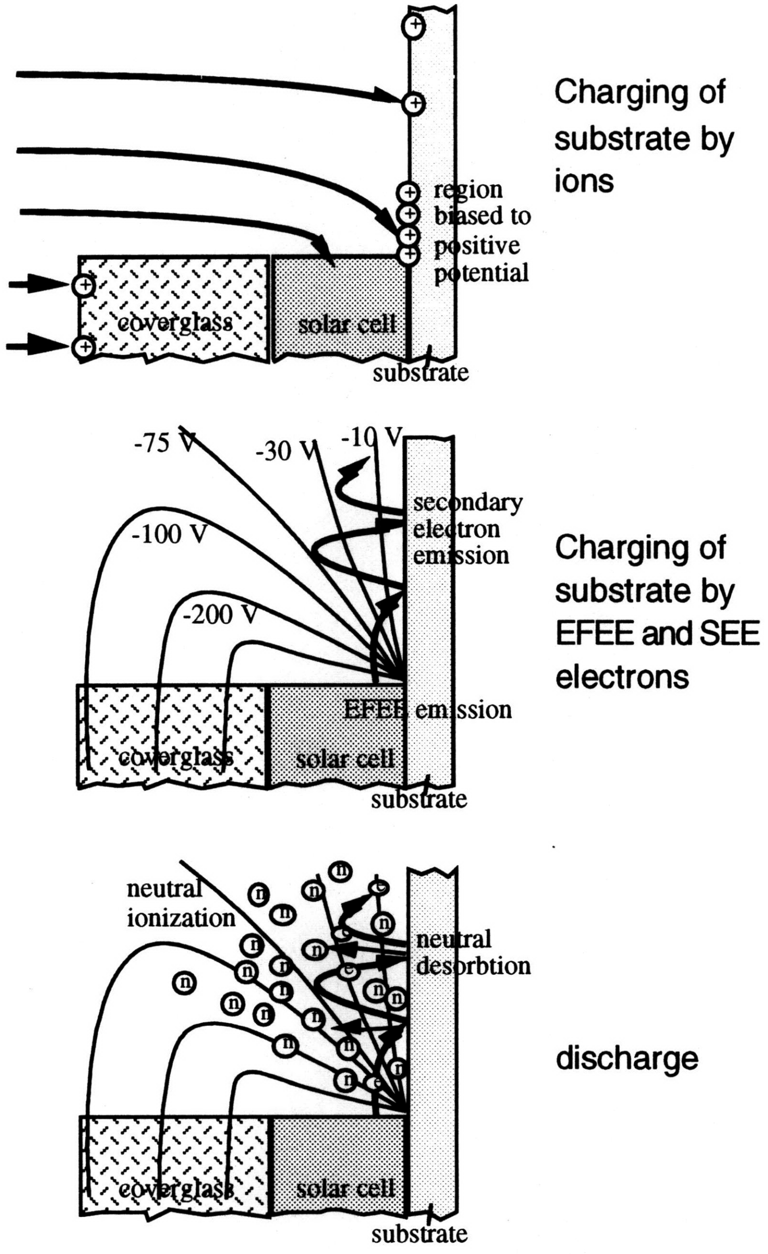

Figure 2.6: Proposed Arcing Sequence of a Wrap-Through-Contact Cell

Chapter 3

Experiment Descriptions

The SAMPIE and HVSA experiments have been designed to study the interaction between high voltage solar cells and the ionospheric plasma environment. The objectives and operations of each experiment will be described in this chapter.

3.1 SAMPIE Description

SAMPIE, the Solar Array Module Plasma Interactions Experiment, was designed to study the arcing behavior and current collection characteristics of different solar cells and materials likely to be exposed to the LEO environment in future missions. SAMPIE was developed at the National Aeronautics and Space Administration (NASA) Lewis Research Center and sponsored by the NASA Office of Aeronautics and Space Technology (OAST). The flight experiment was flown on board the Space Shuttle Columbia in the STS-62 mission launched on March 4, 1994. The Orbiter was placed in a nearly circular orbit with the following orbital parameters:

GMT : 1994+70+04:07:59
Apogee altitude: 307.75 km
Perigee altitude: 299.14 km
Inclination: 38.92^o
M: 352.64^o
Right. Ascension: 204.67^o
Argument of perigee: 47.37^o

The seven main objectives of the SAMPIE experiment were the following [19]

(1) Measure arc rates and strengths for selected solar cell technologies and determine the arcing threshold

(2) Measure the plasma current collection characteristics for the selected solar cell technologies.

(3) Verify different arcing mitigation techniques previously demonstrated in ground tests.

(4) Study the effect of exposed area on current collection through the design of simple metal/insulator geometries.

(5) Study the dependence of arcing threshold, arc rates, and arc strengths on the properties of the metal interconnector.

(6) If time permits, study basic phenomena related to arcing through experiments on materials such as anodized aluminum and Z-93 thermal control paint; these materials will be used in the Space Station.

(7) Obtain the plasma and environmental parameters necessary for data reduction and analysis.

3.1.1 Diagnostic Instruments Description

The Hitchhiker-M carrier configured for the OAST-2 mission, with the SAMPIE package on one of the four top mounting positions, is shown Fig. 3.1. As shown in Fig. 3.2, the plate containing the cells to be biased was mounted on top of the metal box, while most of the instruments and electrical subsystems were placed inside the box. A pressure gauge was also included to measure the background pressure. The gauge could measure ambient pressures from 10^{-7} Torr to 10^{-3} Torr. Two high voltage power supplies (HVPS-1 and HVPS-2) in the electronics box biased the specified cells to predetermined dc voltages, ranging from +300 V to -600 V, above that of the Orbiter. In addition, an electrometer in the HVPS-1 circuit measured the currents collected and a sun sensor located on the experiment plate confirmed the attitude of the Orbiter. Two additional electrical probes were also part of the package: a Langmuir probe to monitor the plasma density and temperature, and a V-body probe to monitor the shuttle's potential with respect to the plasma. It was estimated that SAMPIE would disturb the ionosphere within an area of one meter in all directions [19], and consequently these probes were positioned about five feet away from the box, shown in Fig. 3.1.

3.1.2 Individual Experiments Description

A layout of the experiment plate is shown in Fig. 3.3. In addition to the individual experiments, a sun sensor was used to confirm the Orbiter's orientation.

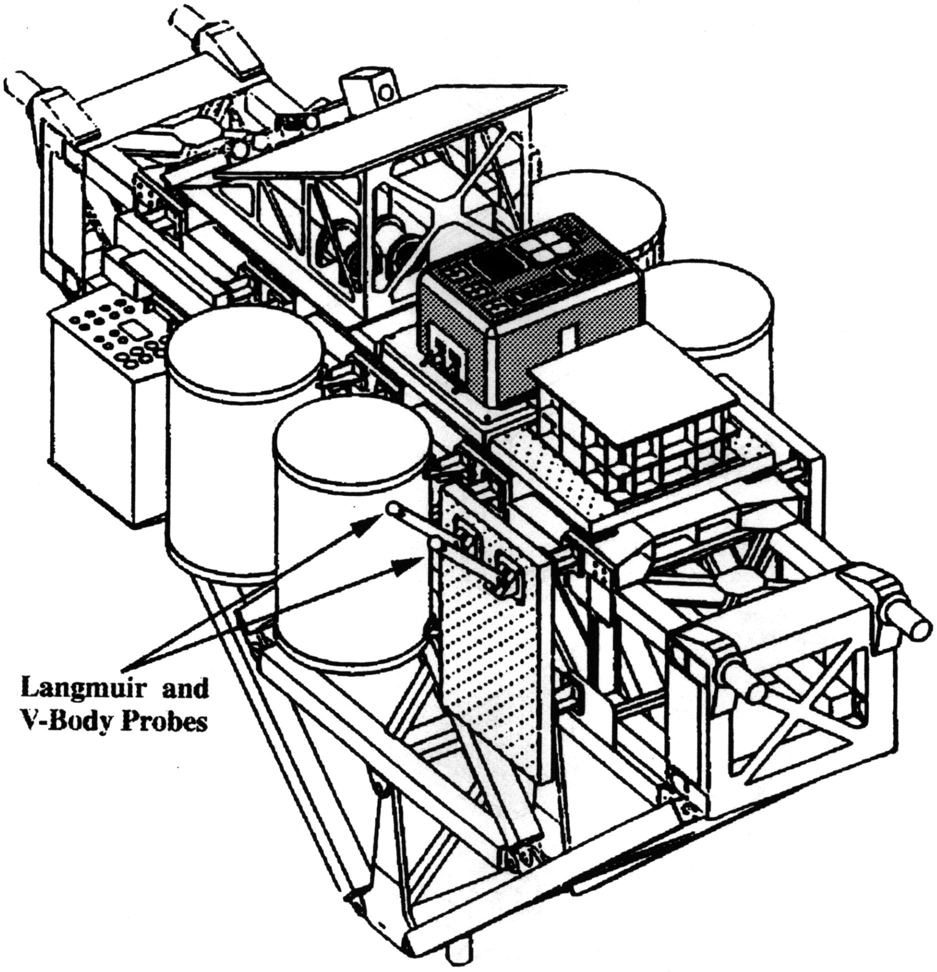

Figure 3.1: Hitchhiker-M bridge configured for OAST-2 mission

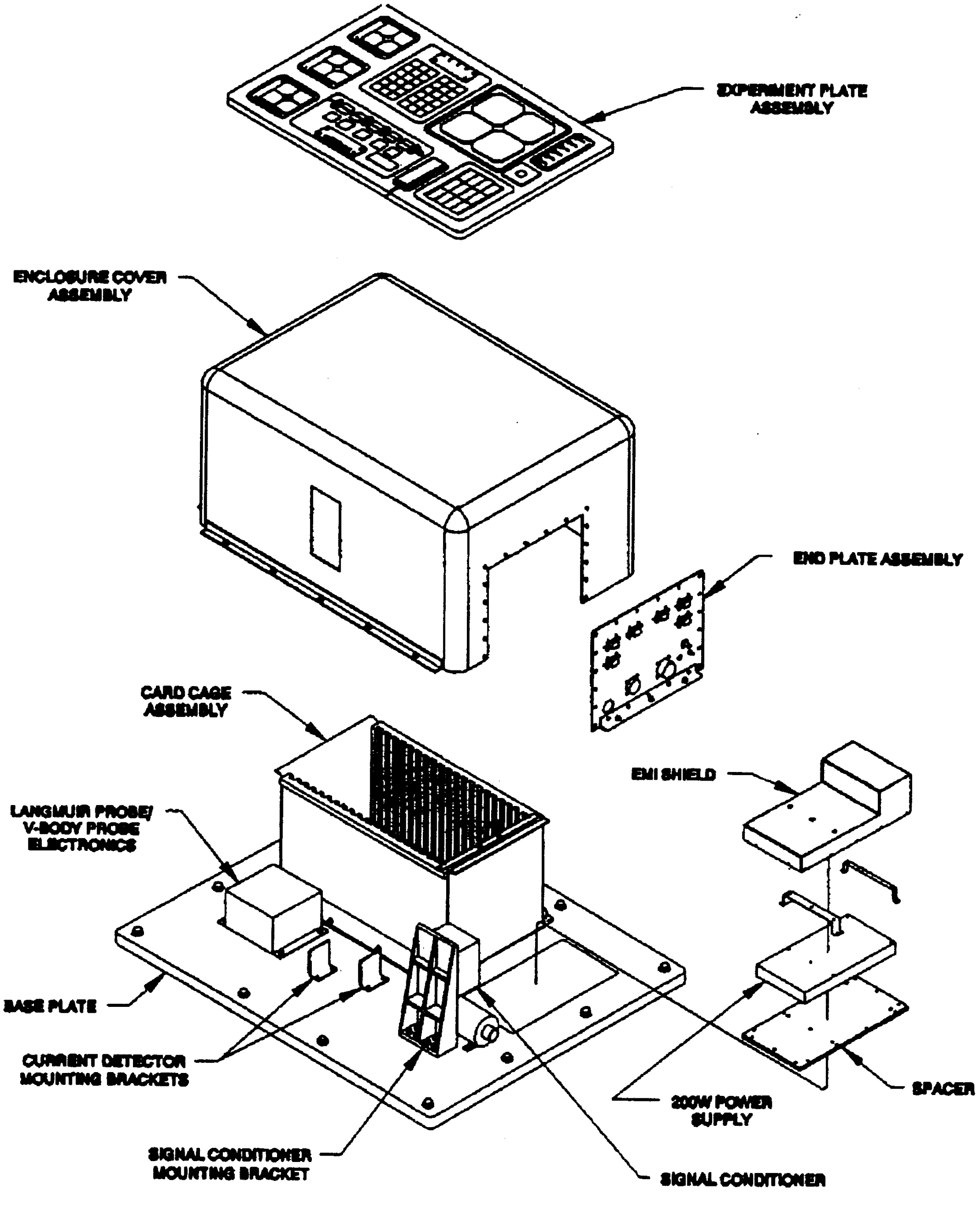

Figure 3.2: The SAMPIE Electronics Box and Sample Tray

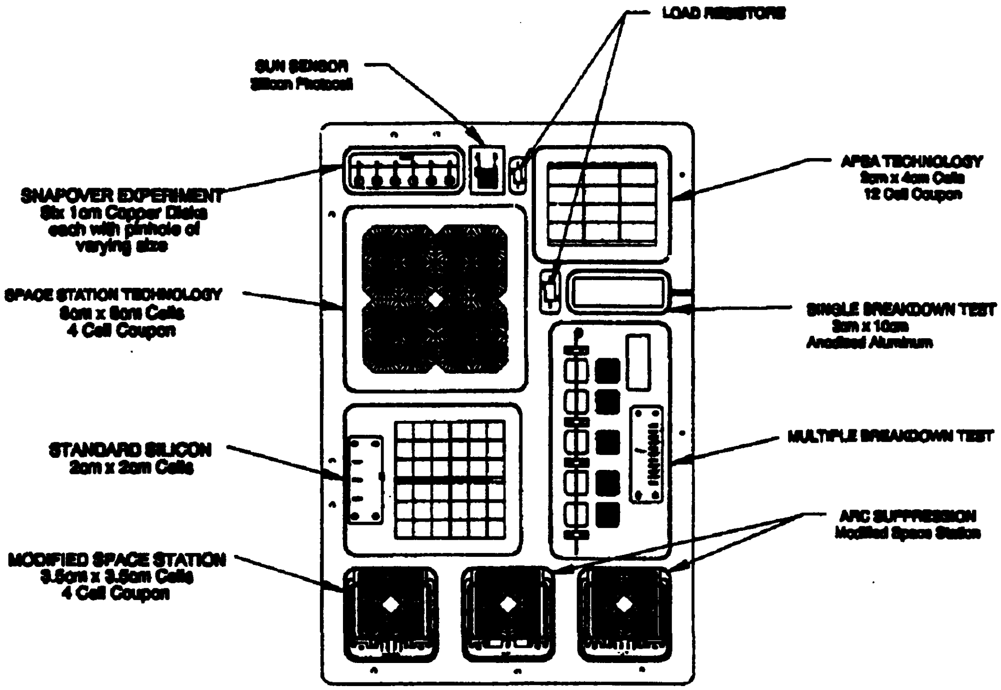

Figure 3.3: The SAMPIE Experiment Plate

In the experiments, different technologies and arcing mitigation strategies were tested. A detailed description of all the experiments is given in Ref. [20]. Among the cells tested was a four cell coupon of 8 cm by 8 cm wrap-through-contact cells to be used on the International Space Station Alpha, a coupon of twelve 2 cm by 4 cm thin Advanced Photovoltaic Solar Array (APSA) cells, and a coupon of four traditional 2 cm by 2 cm silicon solar cells used to provide a baseline for comparison.

The Space Station (SS) cells were designed to operate in LEO at a nominal voltage of -160 V. The cells are mounted on a flexible substrate, and the inter-cell connections are made through copper traces imbedded in the substrate and welded to the back of the solar cells. The coverglass, semiconductor and substrate of these cells were each 203 μm (8 mil) thick, and there was only about a 0.81 mm separation between adjacent cells. The semiconductor is silicon, the substrate is Kapton, and the coverglass is ceria-doped microsheet (CMX).

The APSA cells, built by TRW, presented a thinner silicon cell design. Their reduced thickness, 63.5 μm (2.5 mil), is expected to yield mass savings in future space applications. The thicknesses of the CMX coverglass and the Dow Corning adhesive DC-93500 are 51 μm (2 mil) and 76 μm (3 mil) respectively. The interconnector between these cells is silver plated invar.

Lastly, the conventional silicon cell, representative of the cell technology presently used

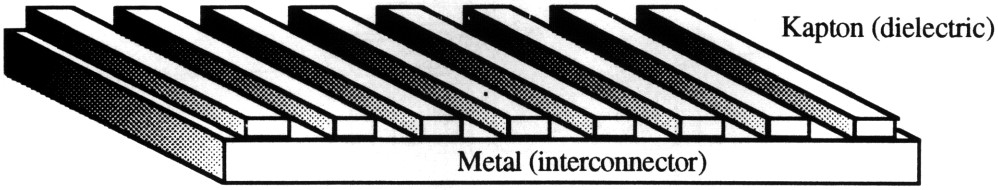

Figure 3.4: Metal Coupon Geometry

in many DOD, NASA, and commercial spacecraft, was also tested. These cells were manufactured by Spectrolab Inc. and incorporated into an array by RCA in 1984. The thickness of the fused silica coverglass and the DC-93500 adhesive are 153 μm and 37 μm respectively. The interconnector between these cells is assumed to be Kovar.

To test different arcing mitigation strategies, three coupons of modified Space Station cells were tested. The size of these cells was reduced from the standard 8 cm by 8 cm to 3.5 cm by 3.5 cm in order to increase the number of experiments that could be conducted. In each of the coupons, a different arc mitigation strategy was tested. In the first set (SSMIN-3), the side of the coverglass overhangs the cell by 0, 101.6, 177.8, and 279.4 μm (0, 4, 7, and 11 mils). In the second set (SSMIN-2), all four cells were shorted together. The excess adhesive has been removed from the edges of the cells using a proprietary process developed by Physical Sciences Incorporated (PSI). In the third coupon (SSMIN-1), the cells had their edges completely covered with the coverglass adhesive except for specified lengths, 0, 203.2, 406.4, and 812.8 μm (0, 8, 16, and 32 mils), which were exposed to the plasma.

On the right side of the experiment plate, there are five metal samples each made of a different pure metal: Gold, Silver, Copper, Aluminum, and Tungsten. On top of these 1 inch square samples are eight Kapton strips placed 0.0625 inch apart. A schematic of a metal coupon in shown in Fig. 3.4. When a discharge occurs, the reaction of the adhesive used to bond the Kapton may be difficult to predict. In order to eliminate this complication, a second set of metal samples with a 1 mm diameter rod suspended 1 mm above the metal's surface was also tested. The distance above the metal was chosen to obtain an electric potential close to the samples of the first set, thus eliminating the dielectrics from the process. While the second set of tests isolate the metal's effect on the arcing process, the geometry of the first set resembles the geometries found in solar cells. This metal/insulator geometry can be found in the triple junction of the conventional cells. The geometry of the Hastings and Cho arcing model closely resembles that of these samples (see Fig. 1.3). A final double sized coupon made of aluminum coated with Z93 is also included with the above sets, but was not tested for arcing. This coupon has been observed to collect electrons under certain conditions, and therefore was positively biased in the experiment.

A piece of anodized aluminum whose composition and anodization process is identical to that of the Space Station main structure was also tested to check whether this material undergoes dielectric breakdown at high voltages. Lastly, an experiment was conducted to study current collection and snapover. The experiment consisted of six 1cm diameter copper disks covered with Kapton each with a different size of pinhole in its center.

3.1.3 SAMPIE Operations

Large scale ground tests of the WTC cells yielded a relationship between bias voltage, plasma density, and plasma temperature [19]. Using this relationship, it was estimated that a dwell time of 20 minutes would be necessary to observe an arc at -120 V. A dwell time of 30 minutes was chosen at -120 V and correspondingly shorter dwell times were chosen for the higher voltages. At higher voltages, the dwell time was determined by the 1 minute minimum required to ensure good measurements of the ion and electron currents. Table 3.1 shows the low voltage biasing sequence and corresponding dwell times at each voltage used in the arcing experiments. Two different high voltage biasing sequences, shown in Table 3.2, were used. Sequence 1S is identical to sequence 1H, used by HVPS-1, but accommodates for the limited voltage range on HVPS-2. Therefore, the cells assigned to the HVPS-1 were biased to a maximum voltage of -600 V while those in the HVPS-2 to -500 V. The metal samples, the anodized aluminum sample, and the modified Space Station cells treated by PSI were assigned to HVPS-2, while the rest of the cells in the arcing experiments were assigned HVPS-1. Arcs were detected by counting the number of spikes in the current flowing through the solar array circuit above a threshold value. The threshold currents were set to 100 mA and 20 mA for the HVPS-1 and HVPS-2 respectively.

In a simplified description of the operation of the SAMPIE experiment, each power supply biased a sample to a bias voltage given by the biasing sequence chosen. When the high voltage sequences were executed, only one cell was biased at a time. The remaining samples were held at the ground potential. Extracts of the planned timeline followed during the experiment is shown in Table 3.3.

Table 3.1: SAMPIE Low Voltage Biasing Sequence

Bias Voltage (V)	Dwell Time (min)
0	1
-30	1
-60	1
-90	1
-120	30
-150	20
-180	5
-210	2
-240	1
-270	1
-300	1

Table 3.2: SAMPIE High Voltage Biasing Dwell Times

Sequence	-400V	-500V	-600V
1H	1	1	1
1S	1	1	-

Table 3.3: Extracts from the Timeline of the SAMPIE Experiment

Run Number	Orbiter Orientation	HVPS-1	Bias Seq.	HVPS-2	Bias Seq.	Duration (min)	Mission Time	
							Hours	Min
31	Ram	APSA	1	Anodized Al	1	63	11	4
32	Ram	SS	1	Copper Kapton	1	63	12	7
33	Ram	Silicon	1	Copper Rod	1	63	13	10
34	Ram	APSA	1	Silver Kapton	1	63	14	13
35	Ram	SS	1	Silver Rod	1	63	15	16
46	Ram	SS	1H	idle	-	3	23	52
47	Ram	idle	-	Copper Kapton	1H	2	23	56

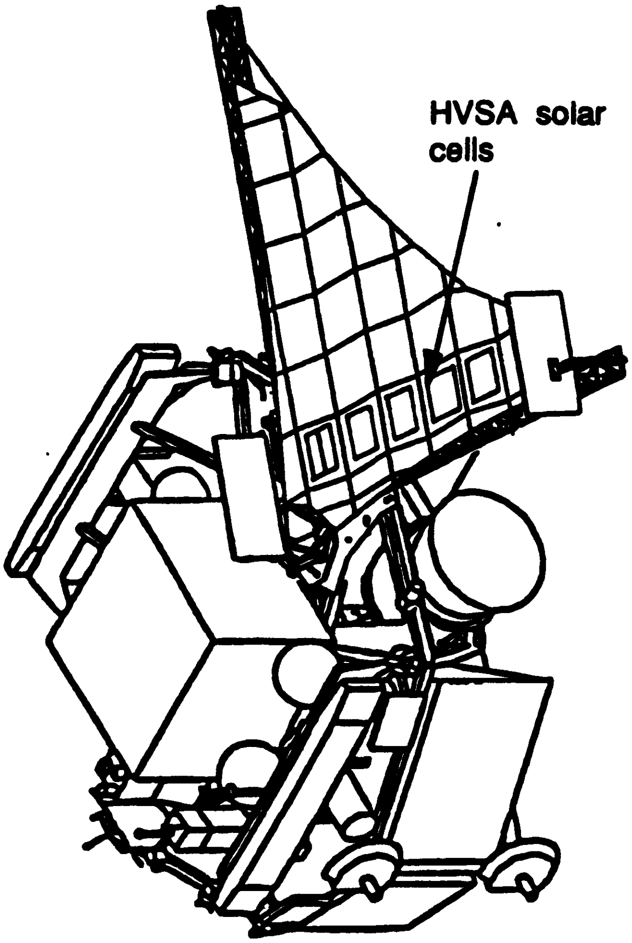

Figure 3.5: Deployment Configuration of the 2D array in the SFU

3.2 HVSA Description

The High Voltage Solar Array (HVSA) experiment was designed to advance the use of photovoltaic power generation at higher bus voltages in space. The experiment, developed by the Institute of Space and Astronautical Science (ISAS), was integrated as one of the eleven experiments conducted on the first flight of the Space Flyer Unit (SFU). The SFU, developed by Japan, is a reusable free-flying space platform with eight integrated standardized Payload Unit Boxes. It was launched by a Japanese H-II rocket on March 20, 1995, injected into a 486 km altitude and 28.5^o inclination circular orbit, and retrieved by the Space Shuttle after six months of operation. The configuration of the SFU, with its triangular retractable array deployed, is shown in Fig. 3.5. The objectives of the HVSA experiment were the following [26]

(1) Demonstrate high voltage photovoltaic power generation in the LEO environment
(2) Verify the function of the series-parallel connecting circuit for the high voltage solar array
(3) Measure the ionospheric plasma interactions of the high voltage solar array

The HVSA experiment was the first to use its own array voltage instead of using an independent power supply. It consisted of the Versatile Power Control Unit (VPCU), the Solar Cell Modules (SCM) and the Electron Collector (EC). The SCMs and EC were mounted in the deployable solar array along the main extensible mast. There were four SCMs, each containing 135 conventional 2 cm by 4 cm silicon cells connected in series. Under nominal conditions, a single SCM could output 60 V at open voltage and 0.3 A of short circuit current. The VPCU changed the electrical connections between the four SCMs, using five Series Relay (SR) switches, to generate open voltages of 60 V, 120 V, 180 V or 240 V, and a maximum power of 80W. Three of these configurations and their corresponding voltage-current curves are shown in Fig. 3.6. The silicon cells in SCMs 1 and 3 were covered with the conventional magnesium fluoride anti-reflection coating while those in SCMs 2 and 4 were covered with a conductive coating. A schematic of this type of cell is shown in Fig. 3.7. The conductive coating was indium tin oxide and was also used to cover the side of the coverglass and adhesive to electrically connect the coating on top of the coverglass to the interconnector. Both types of cells were 100 μm thick. The coverglass is a borosilicate glass manufactured by Nippon Electric Glass and has a thickness of 150 μm. It is assumed to have secondary electron properties similar to those of Pyrex glass. The adhesive, manufactured by Dow Corning, is Sylgard 184 and has a thickness of 40 μm. The interconnector is silver plated invar. The experiment examined these conductive cells by using the relay switches to select which type of cells will be biased to the largest negative voltages.

The array was operated at the open voltage, but once an arc occurred the array was shorted and the voltage was set to zero for the remaining time at that voltage. This mode of operation constrained the number of arcs to a maximum of one arc per biasing time. Arcs were detected by measuring the current flowing through an electron collector. If the current exceeded the threshold value of 0.3 A, the circuit was automatically shorted.

The experiments were conducted twice. The time periods during which the experiment was deployed, executed, and retracted are shown is Table 3.4. During each period, three different dwell times of 1, 5, and 50 minutes were used.

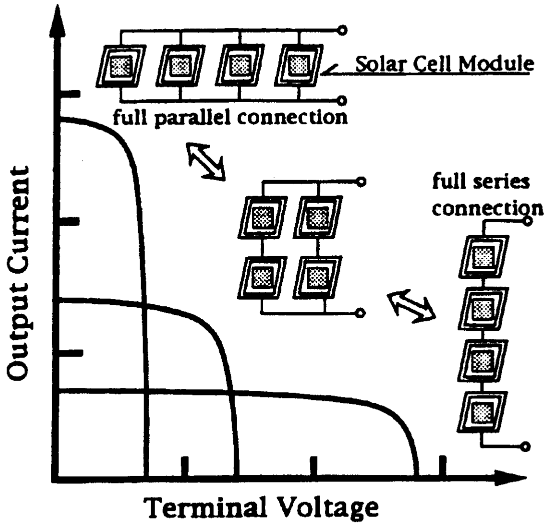

Figure 3.6: Characteristic Voltage-Current Curves

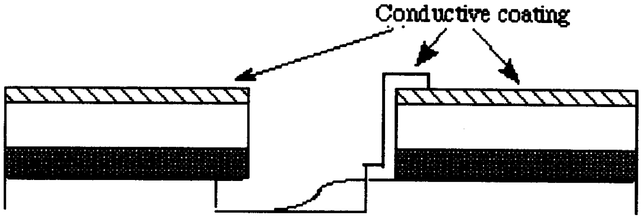

Figure 3.7: Schematic of the Silicon Solar Cell with the Conductive Coating

Table 3.4: Timeline for HVSA Experiment

Experiment Date	Bias Voltage
5/29/95 0:00-09:00	60V
5/30/95 23:00-08:00	120V
5/31/95 22:00-08:00	180V
6/1/95 3:00-12:00	240V

Chapter 4

SAMPIE and HVSA Simulations

Using the semi-analytical code described in Chapter 2, the maximum and minimum arcing activity of the SAMPIE cells was simulated using the experimental data. Similarly the arcing activity expected during the HVSA experiment was predicted.

4.1 SAMPIE Simulations

4.1.1 SAMPIE Data Acquisition

During the experiment, preliminary data was received by the OAST-2 payload control center at the Goddard Space Flight Center. After 37 hours of scheduled data taking, an anomaly with the HVPS-1 circuit necessitated reconsideration of the experiment timeline, and new instructions were transmitted to SAMPIE on orbit. A total of 62 hours of current collection and arcing data were obtained, stored on board, and recovered after Columbia returned to Earth. A total of 18 hours and 46 minutes of arcing data were obtained in the bay-to-ram orientation and 24 hours of data were obtained in the bay-to-deep-space orientation. These orientations are shown in Fig. 4.1.

During the experiment, the neutral pressure and orbital potential were continuously monitored. The V-body probe showed that the potential of the Shuttle never differed from the ambient plasma potential by more than ±3 Volts during the arcing experiments. Therefore, the potentials of the cells with respect to the plasma environment are accurately represented by the applied bias voltages.

Approximately every three minutes, the Langmuir probe performed a plasma density/temperature sweep. Standard probe theory was used to obtain these parameters from the raw sweeps. However, these standard techniques did not yield the correct plasma parameters expected from a moderate sized probe in a flowing plasma facing the ram direction. Both the plasma densities and temperatures were uniformly higher than expected.

A comparison between ionosonde data during times and locations coincident with the

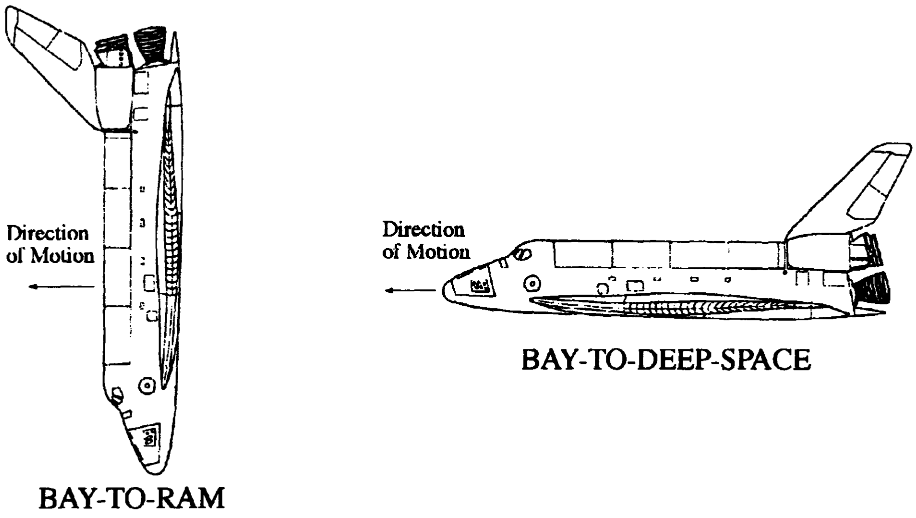

Figure 4.1: Bay-to-Ram and Bay-to-Deep-Space Orientations

Shuttle orbit during the bay-to-ram data taking period and the IRI-86 model showed that the IRI model predictions are extremely good, especially in the daytime [32]. Based on the IRI model, simple correction factors could be applied to the standard probe theory results to yield accurate densities and temperatures. The corrections were the following [8]: divide the experimental plasma densities by a factor of 3.6 and apply a linear correction to the electron temperatures (1.74T-0.31). The simulations and data analysis of the arcing rate in the SAMPIE experiments used the ambient plasma conditions obtained using these corrections. It is believed that the plasma densities are correct to within about 10% and the electron temperatures to within 0.03 eV.

Compilations of the data obtained from the arcing experiments for the conventional cells, WTC cells, and the metal coupons at the times when the plasma diagnostics were recorded are shown in Appendix A. The environmental data includes the corrected plasma densities and plasma temperatures for the ram data, sun sensor readings, and neutral pressures. The corrected plasma densities and temperatures during a portion of the flight in the bay-to-ram orientation are shown in Fig. 4.2 and Fig. 4.3 respectively. The plasma density and electron temperatures show peaks and valleys about every 90 minutes, the period of the orbit. The peaks correspond to when the shuttle receives sunlight and therefore measures the daytime plasma environments, and the valleys correspond to when the shuttle is in eclipse and the

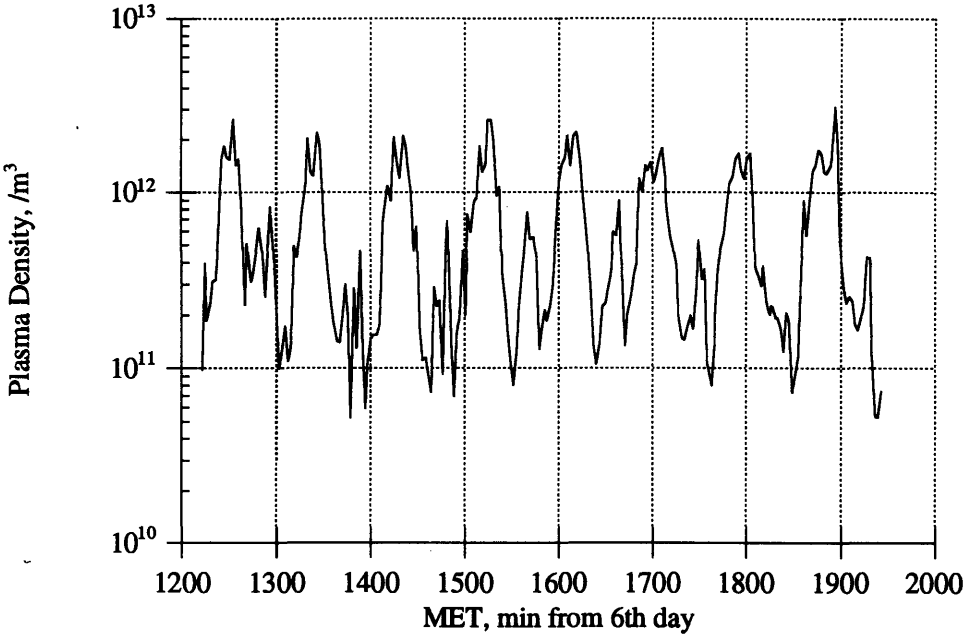

Figure 4.2: Plasma Density measured by SAMPIE (corrected) in ram

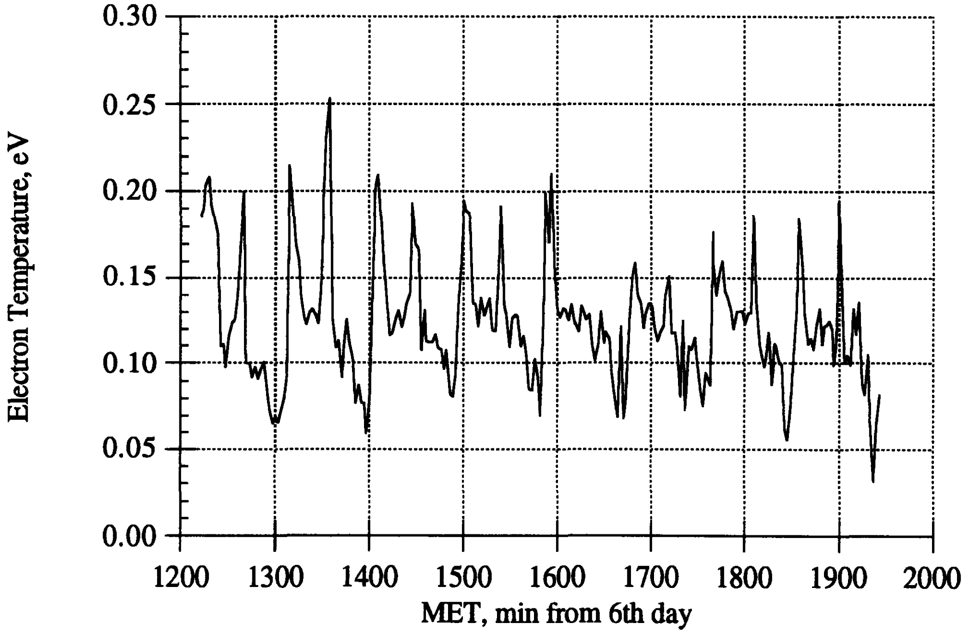

Figure 4.3: Electron Temperature measured by SAMPIE (corrected) in ram

night time plasma parameters are measured. No corrected values of the Langmuir probe data were available for the bay-to-deep-space orientation period. The plasma density and electron temperature in the bay-to-deep-space used for the simulations were inferred from the IRI-86 model. The Environmental Work Bench (EWB) software package developed by S-Cubed, with accurate solar activity parameters, was used to infer these quantities.

In addition, the cell temperatures annotated during the preliminary telemetering to the payload control center are also included. The last column identifies those data points considered to be outliers and consequently not used in the data analysis or simulations. These points were labeled as B (bad) for several reasons, such as anomalously high arc counts or the concurrent operation of other experiments in the shuttle bay. In the bay-to-space data, an increase in arc rate and neutral pressure was observed when gas was released during the Experimental Investigation of Shuttle Glow (EISG) experiment. Arc counts above 1000 counts were considered anomalous high. When the anomaly in the HVPS-1 circuit occurred, the number of arcs detected increased from tens of arcs to counts ranging from 1000 to 3000. Therefore, arc counts above 1000 counts were discarded. Due to the anomaly in the HVPS-1, the arcing data obtained from the silicon, APSA, and WTC cells is limited to a few experiments in the bay-to-ram orientation. The metal coupons, however, were additionally biased in the bay-to-deep-space orientation, providing valuable data.

4.1.2 SAMPIE Simulations

The predictive capability of the modified semi-analytical code described in Chapter 2 was verified by generating arcing rates for the conventional cells and metal samples biased during the flight experiment. These arcing rates used the experimental data obtained from the flight experiment and were then compared to the experimental arcing rates. The given and assumed properties for the conventional, wrap-through-contact and a selected metal coupon are summarized in Table 4.1. The geometry of the five metal coupons with the Kapton strips closely resembles that of the proposed model. The only property differing between the metal samples is the work function of the conductor. The work function ϕ_w is a measure of the ease with which electrons are released from the surface. The given and assumed work functions for the metals and their oxides are shown in Table 4.2 [9, 28].

Whenever possible, the environmental data measured by SAMPIE was used in the simulations. Since the cell temperature was not annotated for all the experiments, the range used was that observed during the bay-to-ram portion of the experiment, -5°C to 15°C. These temperatures provided a maximum and minimum arc rate value for each run. Values for those environmental variables not recorded during the flight experiment, such as ambient

Table 4.1: SAMPIE Cell Data

Cell Type	Si	Si WTC	APSA	Gold Sample
Manufacturer	RCA	NASA	TRW	-
Cell Size (cm^2)	2x4	8x8	2.6x5.1	0.158x2.54
No. of Cells	4	4	12	8
Cell Gap (μm)	500	1000	635	1588
d_{cell} (μm)	203	203	56	-
d_1 (μm)	153	203	51	25
d_2 (μm)	37	N/A	76	20
ϵ_{d_1}	3.5	4	4	3
ϵ_{d_2}	2.7	3	2.7	3.8
γ_{max_1}	3.46	4	4	2.1
γ_{max_2}	3	2	3	-
E_{max_1} (eV)	330	400	400	150
E_{max_2} (eV)	300	200	300	-
ϕ_w (eV)	4.76	4.85	4.26	5.1

Table 4.2: Work Functions of the Metal Samples and Oxides

Metal Sample	Pure Metal ϕ_w (eV)	Oxide ϕ_w (eV)
Gold	5.1	-
Copper	4.65	5.02
Tungsten	4.55	4.95
Aluminum	4.28	4 7
Silver	4.26	4.68

Table 4.3: Environmental Parameters for Minimum/Maximum Arcing

Condition	Plasma Density	Electron Temperature	Ion Velocity	Neutral Density	Cell Temperature
Min. (Si/APSA)	$5.3 \times 10^{10}\,m^{-3}$	0.0818 eV	7728 m/s	$1.53 \times 10^{16} m^{-3}$	288.1 K
Max. (Si/APSA)	$1.7 \times 10^{12}\,m^{-3}$	0.1946 eV	7728 m/s	$2.36 \times 10^{16}\,m^{-3}$	268.1 K
Min. (Metals)	$7.3 \times 10^{10}\,m^{-3}$	0.0752 eV	360 m/s	$4.56 \times 10^{14}\,m^{-3}$	288.1 K
Max. (Metals)	$3.1 \times 10^{12}\,m^{-3}$	0.2036 eV	7728 m/s	$1.21 \times 10^{15}\,m^{-3}$	268.1 K

neutral temperature, ion mass, and ion velocity in the ram orientation, were generated using the EWB package. The variation of these parameters during an orbit was small and therefore average values for these variables were used. The experimental and assumed environmental parameters conducive to maximum and minimum arcing activity used in the simulations are listed in Table 4.3. The simulations also included the experimental current threshold, 100 mA for the silicon and APSA cells and 20 mA for the metal coupons. As explained in Chapter 2, with these thresholds only the occurrence of "big arcs" will be detected.

The dynamic range in plasma density, and neutral density for the cells and the metal coupons is very small. However, the range in the ion velocity is large for the metal coupons. This is due to the fact that when the coupons were biased in the bay-to-deep-space orientation where the ions will no longer arrive at the front surface with orbital velocity, but with the thermal velocity. A comparison between the arc rates obtained by the simulations and the experimental values for the silicon and APSA cells is shown in Fig. 4.4. In general, the experimental values fall within the maximum and minimum simulated arc rates. For the silicon cell at -600 V, the semi-analytical code underpredicts the arcing rates, but the simulated values are of the same order of magnitude as the experimental values. A trend is seen in both the experimental and simulated data: the arcing activity greatly decreases when the Shuttle is in the bay-to-deep-space orientation.

Similar comparisons were generated for each of the metal samples and are shown in Figs. 4.5 to 4.9. The model accurately simulated the arcing activity of the copper coupon (Fig. 4.6) and tungsten coupon (Fig. 4.7), while underpredicted that for the gold sample (Fig. 4.5) at the high voltages. The low predicted values may be due to the fact that the measured plasma density, or neutral density may be imprecise. It is interesting to note how the maximum predicted arc rates show the same trends seen in the actual data. A good example of this agreement is seen in the copper sample simulations in Fig. 4.6. In Chapter 5, the arc rate dependency on various parameters such as the work function will be examined

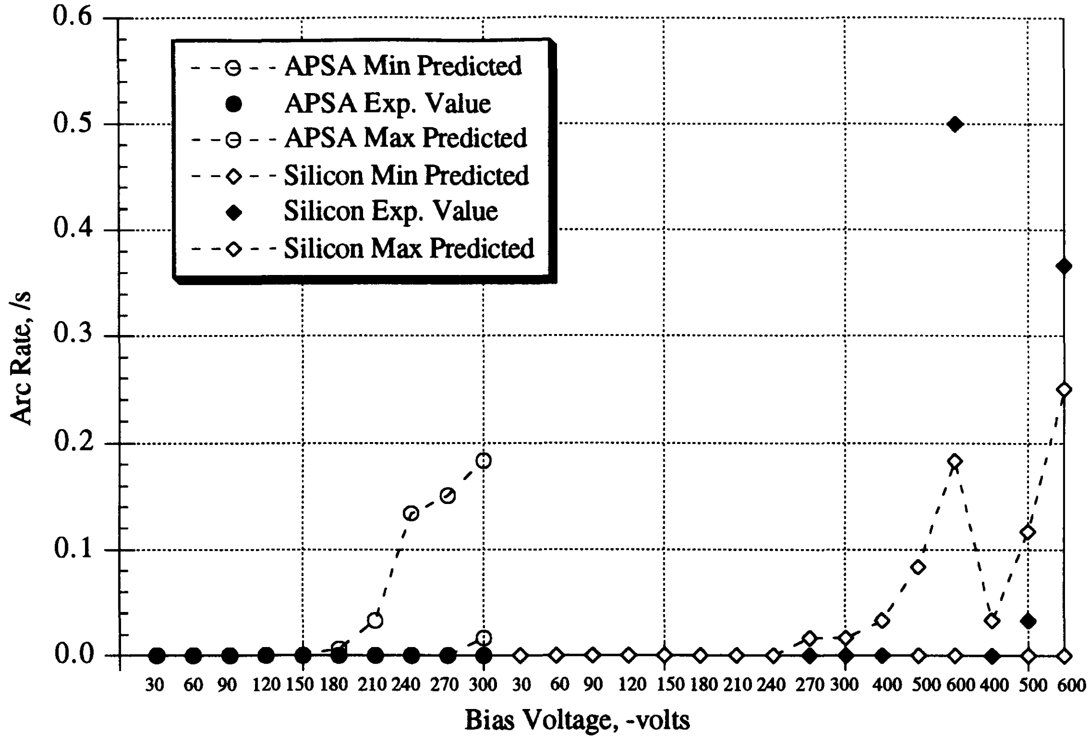

Figure 4.4: Experimental and Simulated Arc Rates for the Silicon and APSA cells

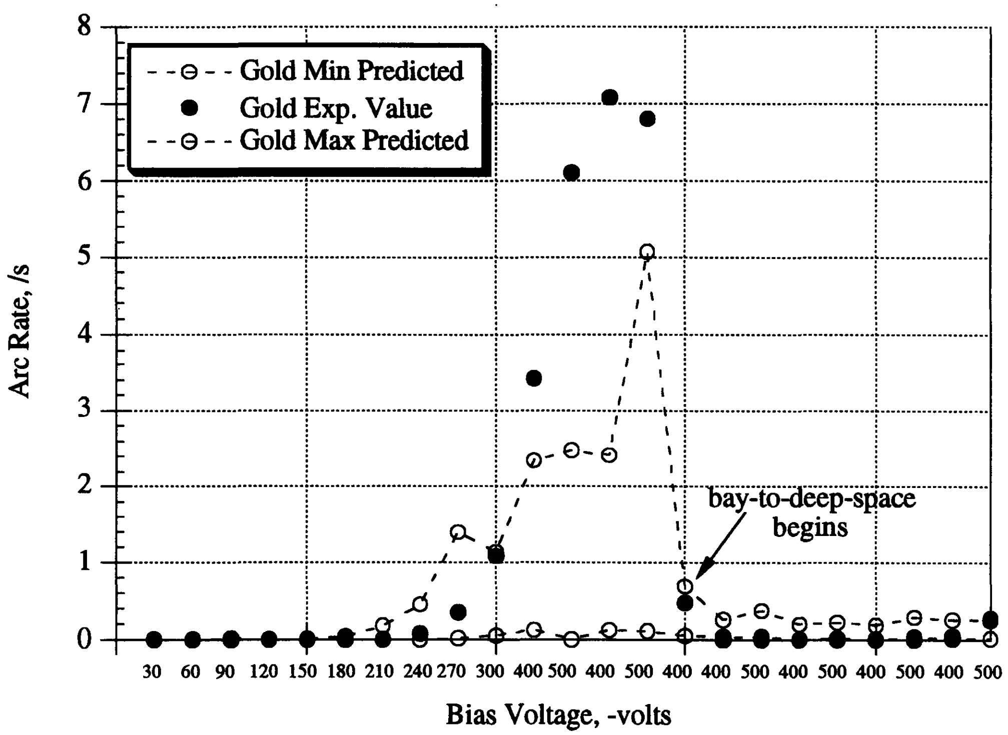

Figure 4.5: Experimental and Simulated Arc Rates for the Gold Coupon

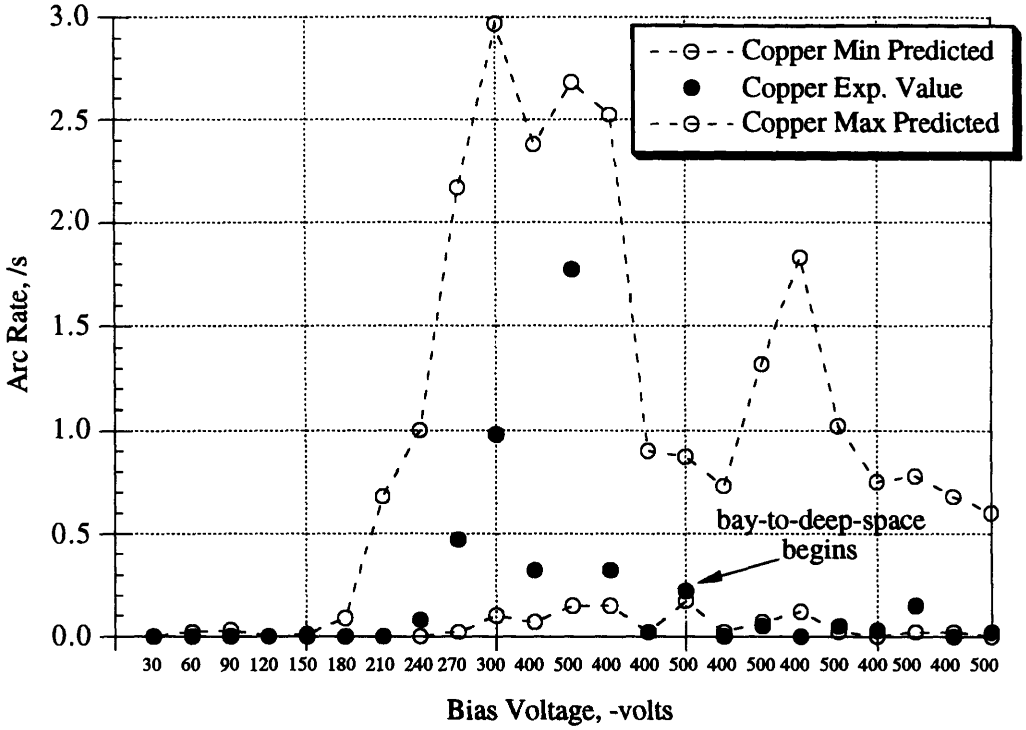

Figure 4.6: Experimental and Simulated Arc Rates for the Copper Coupon

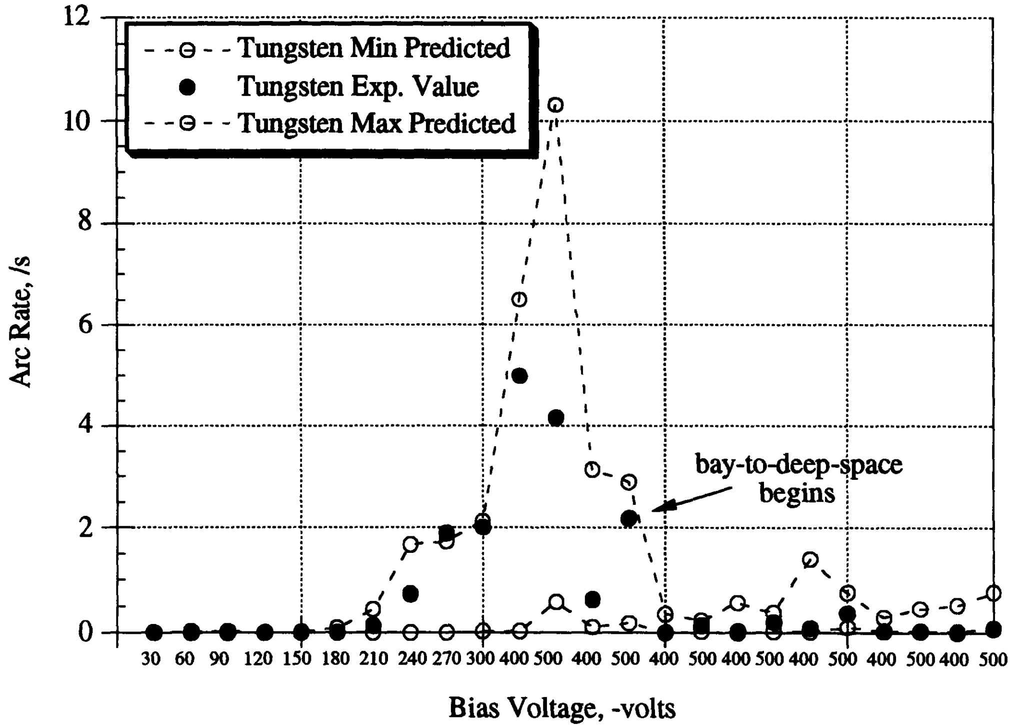

Figure 4.7: Experimental and Simulated Arc Rates for the Tungsten Coupon

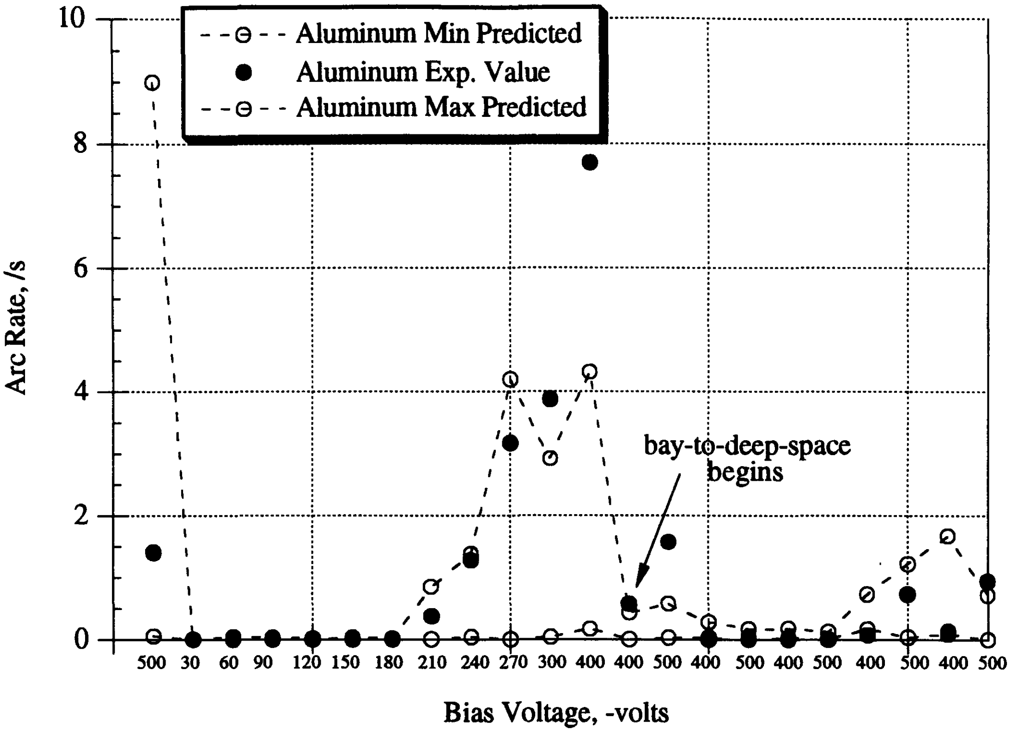

Figure 4.8: Experimental and Simulated Arc Rates for the Aluminum Coupon

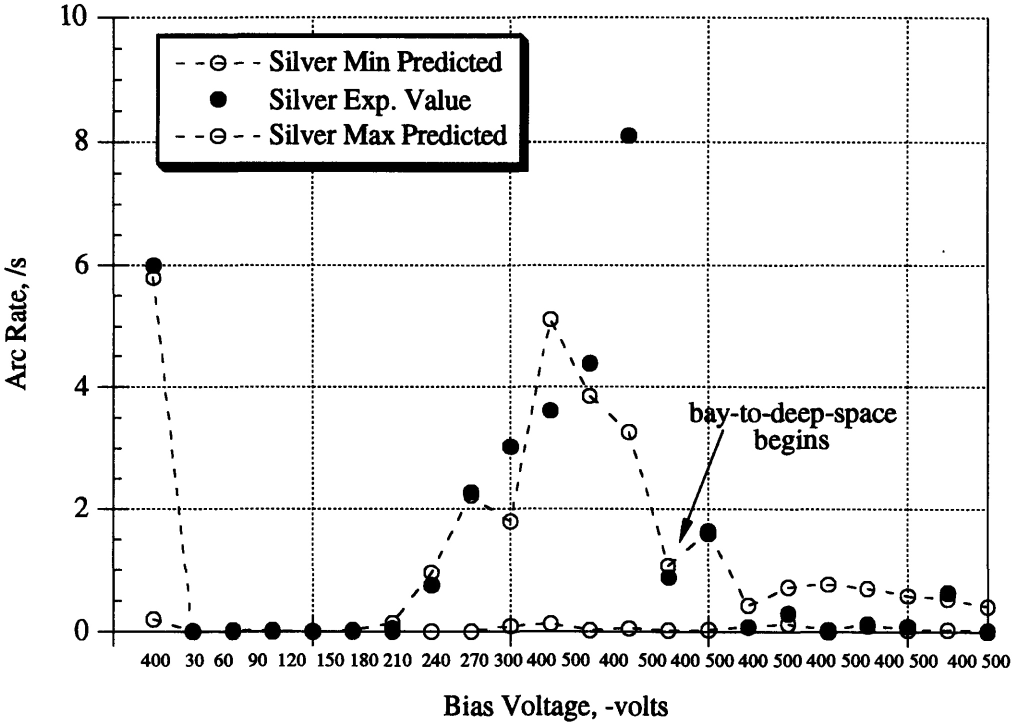

Figure 4.9: Experimental and Simulated Arc Rates for the Silver Coupon

Table 4.4: Environmental Parameters for Minimum/Maximum Arcing for SFU orbit

Condition	Plasma Density	Electron Temperature	Ion Mass	Ion Velocity	Neutral Density	Cell Temp.
Minimum	$4.2 \times 10^{10}\ \mathrm{m}^{-3}$	0.057 eV	$1.99 \times 10^{-26}\mathrm{kg}$	1130 m/s	$2.5 \times 10^{12}\ \mathrm{m}^{-3}$	320 K
Maximum	$4.2 \times 10^{11}\ \mathrm{m}^{-3}$	0.075 eV	$7.47 \times 10^{-27}\mathrm{kg}$	7620 m/s	$1.1 \times 10^{13}\ \mathrm{m}^{-3}$	250 K

using the flight data from these metal samples.

4.2 SFU Predictions

The semi-analytical code was also used to predict the arcing activity of the HVSA solar cells. The comparison of these predictions with the actual data will serve to validate the model. As seen in Fig. 3.7, the conductive coating in the second type of cells will cover the triple junction. This geometry will eliminate any potential difference between the triple junction and the coverglass' front surface, thus eliminating the enhanced field electron emission from the conductor's surface. Therefore, no arcing is expected for these cells.

The semi-analytical code was used to predict the arcing activity of the silicon cells covered with the conventional anti-reflection coating. To provide arc rate predictions for these cells, the SFU orbit was recreated using the EWB software package with the flight orbital parameters. The SFU is in a 486 km circular orbit at an inclination of 28.456°. The environmental variables conducive to maximum and minimum arcing rates for this orbit are listed in Table 4.4. The value for the maximum electron temperature is rather low. This discrepancy, however, will not affect the arcing rate since it is included in the maximum ion flux expression which is dominated by the orbital velocity. The cell temperature range was chosen to be the same as that seen in the silicon cells in the PASP experiment [40], which is also a small free-flying spacecraft in LEO.

The given and assumed properties for the simulated silicon cells are shown in Table 4.5. The semi-analytical code was used to provide maximum and minimum arc rate predictions. The minimum predictions show no arcing. This is because, unlike SAMPIE, the HVSA cells will always be pointing at the sun, resulting in operation at various angles of attack in both ram and wake orientations. Thus, the low ion flux in the wake orientation will not be large enough to induce arcing. Since the circuit will be shorted when an arc occurs, predictions will be presented as the probability that an arc will occur within a given time, rather that as a rate. Using the parameters conducive to maximum arcing and cell temperatures ranging

Table 4.5: Silicon Cell Data

Cell Type	Si
Manufacturer	-
Cell Size (cm^2)	2x4
No. of Cells	135
Cell Gap (μm)	630
d_{cell} (μm)	100
d_1 (μm)	153
d_2 (μm)	37
ϵ_{d_1}	7.3
ϵ_{d_2}	2.7
γ_{max_1}	2.4
γ_{max_2}	-
E_{max_1} (eV)	400
E_{max_2} (eV)	-
ϕ_w (eV)	4.26

from 240 K to 320 K, arcing probabilities were generated for the different bias voltages. No arcing was seen at 60 V and 120 V. When biased at 240 V, the code always predicted arcs within the first second. The generated probabilities for 180 V at different cell temperatures are shown in Fig. 4.10. The plasma density in this graph varies from the maximum plasma density by two orders of magnitude. This density was chosen to account for the increased neutral density on the dielectric surface due to electron stimulated desorption.

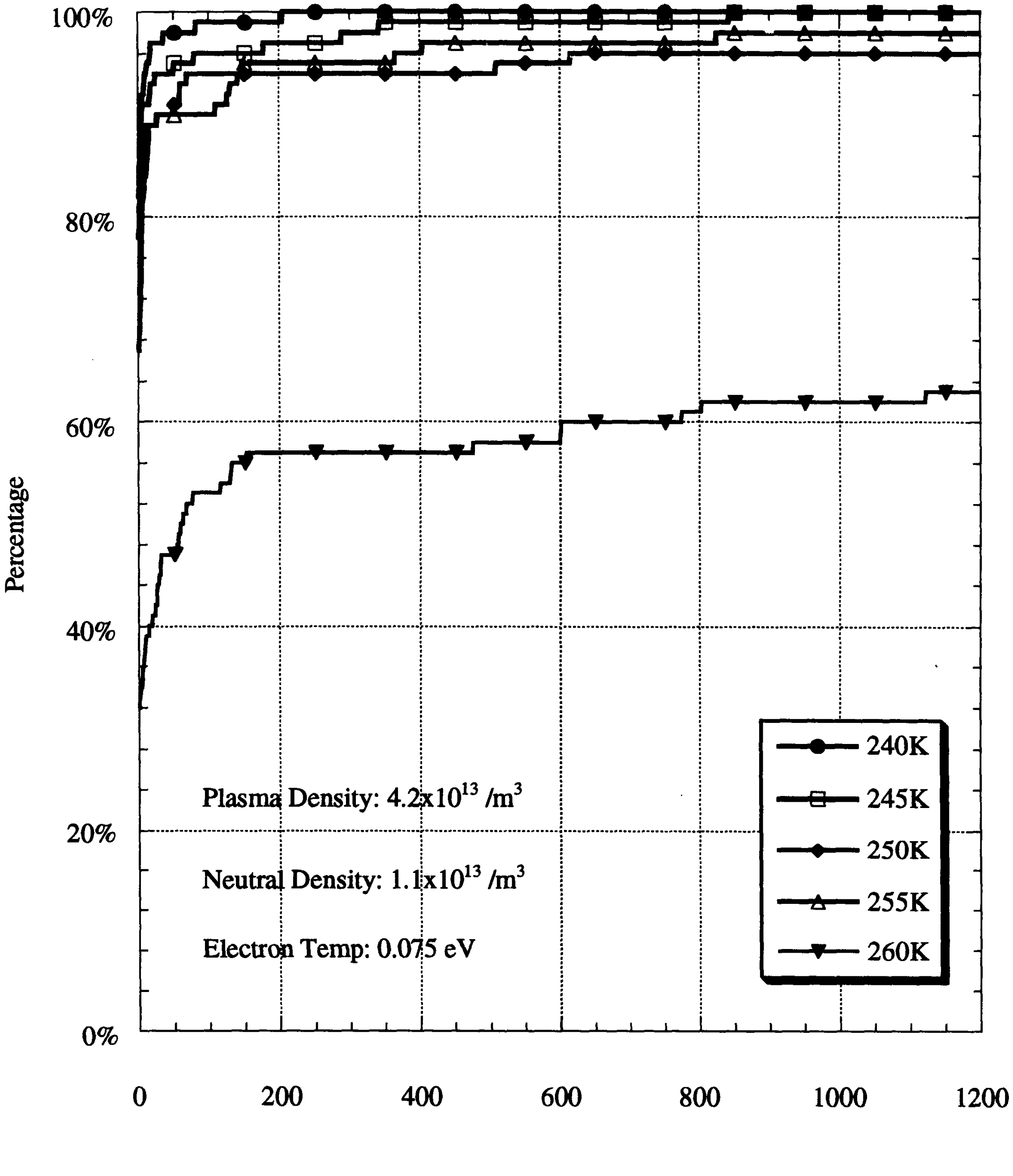

Figure 4.10: Probability of an Arc Occurrence within a given Time

Chapter 5

SAMPIE Data Analysis

In this chapter, the dependency of the arc rate on several variables suggested by the semi-analytical model will be discussed. These dependencies will be then examined in the arcing data obtained from the SAMPIE experiment. These dependencies were not examined in the HVSA arcing data since this data was not available at the time of the writing of this thesis.

5.1 Arc Dependency on Various Parameters

From the model proposed by Cho and Hastings, it is possible to identify operational parameters, environmental variables, and material and geometric properties which will affect the arcing rate. The dependency of the arc rate on the bias voltage V_b, electron work function of the interconnector material ϕ_w, dielectric thickness d, front surface area A_{cell}, overhang of the coverglass d_o, ion flux Γ_i, neutral flux Γ_n, and cell temperature T_s will be examined. In general, the arc rate can be expressed as $\dot{R} = \dot{R}(V_b, \phi_w, d, A_{cell}, d_o, \Gamma_i, \Gamma_n, T_s)$

5.1.1 Bias Voltage

The dependency of the arc rate on the bias voltage is obtained by setting the remaining parameters to constants. Eqn. 2.27 suggests the following functional form :

$$\dot{R} = \frac{1}{c_0 \exp(\frac{c_1}{V_b}) + c_2 V_b} \tag{5.1}$$

At low voltages, the electric field at the triple junction will be small and the charging time will be dominated by the EFEE term. Thus, the ion charging time may be neglected. Since the EFEE charging time decreases exponentially with V_b, the arc rate will increase exponentially with V_b. This exponential dependency gives an effective threshold voltage: the voltage at which the EFEE charging time is on the order of the experiment time. No arcs have been observed above -96V, the operational voltage used in European spacecraft [17];

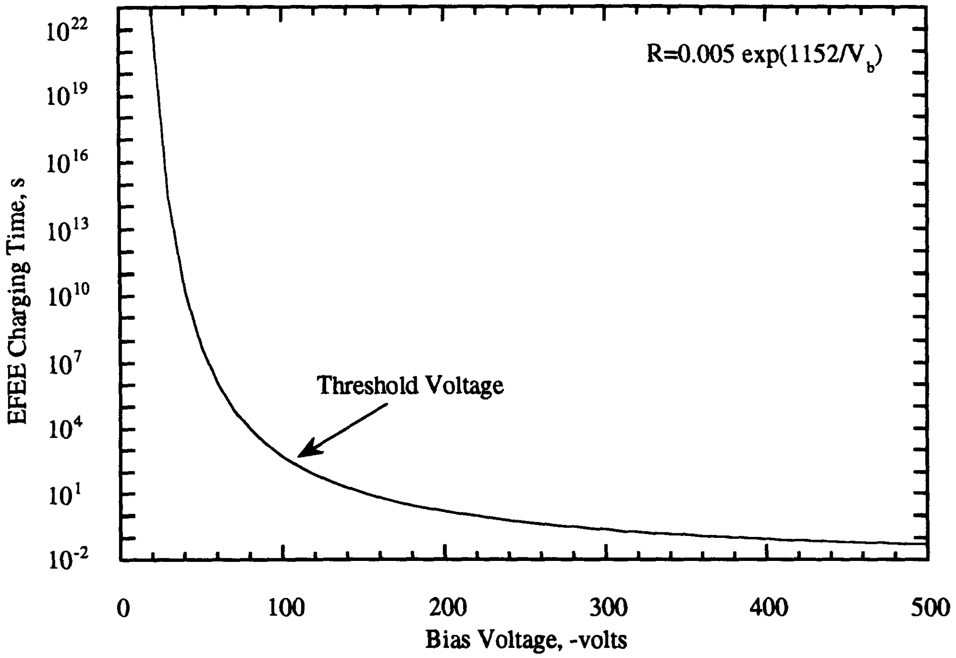

Figure 5.1: Typical Ion Charging Time Curve and Voltage Threshold

therefore, the threshold voltage is above this value. Fig. 5.1 shows this threshold voltage for a typical EFEE charging time curve. The threshold voltage is close to -100 V when the experiment time is on the order of 100 seconds.

5.1.2 Material Properties

Under normal conditions, electrons are prevented from leaving a metal by a potential step at the interface. The height of this step is the work function, ϕ_w. If given sufficient energy, the electrons will escape. Metals with higher work functions will exhibit a lower electron emission from the conductor's surface. Thus, the time needed for the electric field to run away will be increased with increasing work function. The work function is included in the Fowler-Nordheim coefficients in the τ_{efee} equation. If the arcing rate is defined as $1/\tau_{chrg}$, and setting the other parameters to constants, the dependency of the arc rate $\dot{R}$ on the work function ϕ_w is given by

$$\dot{R} = \frac{1}{c_0\sqrt{\phi_w}10^{4.52/\phi_w}\exp({\phi_w}^{1.5}) + c_1} \tag{5.2}$$

The dependency on the work function is more pronounced for low bias voltages, where the τ_{ion} term, c_1, may be neglected. The presence of the work function term in the exponential term ensures that the arcing activity will be greater for interconnectors with lower work functions.

5.1.3 Cell Geometry

The geometry of the cell plays an important role in the arcing mechanism. The thickness of the dielectric d determines the magnitude of the electric field at the triple junction, given by $E_{TJ} = \phi_d/d$, where ϕ_d is the potential difference between the triple junction and the front surface of the dielectric. A thicker dielectric will lower the electric field and consequently increase the time for the electric field to build up, decreasing the arc rate. Similar to the work function, the effect of the dielectric thickness is more prominent at low voltages where τ_{efee} dominates the arcing process. The dielectric thickness enters the τ_{efee} term in its exponential factor. Thus, eliminating the other variables, the arcing rate at low voltages can be written as a function of d as $\dot{R} = c_0 \exp(-c_1 d)$ where c_0 and c_1 are positive constants.

The area of the front surface of the cell A_{cell} will also affect the arcing rate. The model suggests that the arc rate will vary linearly with the number of correlated areas encompassed by the cell. Therefore, the arc rate will be affected by an increase or decrease by a finite number of correlated areas. Although the cell area is present in the τ_{ion} expression, its effect is canceled by the cell area term present in the capacitance of the dielectric front surface, given by Eqn. 2.25.

Lastly, the arc rate will also be affected by the overhang of the coverglass over the adhesive and solar cell. Numerical simulations conducted by Cho [4] and Mong [31] showed that the EFEE charging time increased dramatically with the addition of an overhang, resulting in a decrease in the arcing rate. Mong [31] derived an expression for the critical overhang distance, such that overhangs greater than this length will decrease the arcing activity dramatically. Using this expression, for example, the critical overhang distance is 67 μm for a conventional silicon cell biased at -400 V. Therefore it is expected that the arcing rate should decrease dramatically for solar cells with an overhang distance above the critical overhang distance.

5.1.4 Environmental Variables

The semi-analytical model predicts that there is a critical ambient ion flux. If the ion flux is below this value, the electric field created by the ions deposited on the front surface will not be sufficient to start the enhanced field electron emission from the conductor surface. In this case, the ion charging time τ_{ion} will be greater than the experiment time τ_{exp}. Thus, no arcs will occur during the experiment. The critical ion flux, $\Gamma_{i_{crit}}$, calculated by setting Eqn. 2.26 to τ_{exp}, is given by

$$\Gamma_{i_{crit}} = \frac{\Delta V_{drop} C_{front}}{e A_{cell}} \tag{5.3}$$

where ΔV_{drop} is the voltage drop during an arc. For given dielectric constants, the critical ion flux will vary linearly with this drop. If this voltage drop varies with the bias voltage, than the critical ion flux will also be a function of the bias voltage. If τ_{ion} is less than τ_{exp}, a further dependency can be derived from Eqn. 2.27. Setting the remaining parameters to be constants, the arc rate $\dot{R}$ is given by $\dot{R} = \frac{1}{c_0/\Gamma_i + c_1}$. At very large voltages, where the EFEE term can be neglected, the expression suggests that the arc rate varies linearly with ion flux.

The cell temperature and neutral flux onto the side surface determine whether the desorbed neutral density is sufficient to allow breakdown to occur. As described in Chapter 2, for a given cell temperature, there is a critical neutral flux below which breakdown will not occur. If the ambient neutral flux is below this value, the surface cannot be recharged during the experiment time. Lower cell temperatures result in a higher number of neutrals on the surface available and consequently a lower ambient neutral flux is needed for breakdown to occur. Similarly, for a given neutral flux and experiment time, there is a cell temperature above which not enough neutrals will reside on the surface to allow breakdown. If the arc rates are measured while the cells are always at the same angle of attack, the neutral flux will vary with neutral density and with the temperature of the neutrals. The cells in the SAMPIE experiment were oriented in the ram and in the bay-to-deep-space orientations. In the ram orientation the flux to the side surface of the solar cell is only due to neutrals moving with thermal velocities. Since the experiment was placed in the shuttle bay, it will be assumed that the side surface of the cells while in the latter orientation was also charged only by the thermal flux. Therefore, these orientations become indistinguishable with respect to the neutral flux. If the temperature of the neutrals is assumed to be constant, the neutral density and flux become interchangeable parameters in the data analysis

5.2 Statistical Significance Discussion

During the SAMPIE experiment, each power supply biased a sample to a given voltage while the others were grounded. The arc counts were detected by counting the number of times the current in the circuit exceeded a specified threshold, 100 mA for the solar cells and 20 mA for the metal samples. The arc rates were then calculated by dividing the number of arcs by the corresponding dwell time at each voltage. In this type of experiment, two types of uncertainties must be addressed. Instrumental uncertainties arise from a lack of perfect precision in the measuring instruments and are often independent of the actual value of the quantity being measured. If the occurrence of arcs is assumed to be a random process, uncertainties also arise from statistical fluctuations in the collection of finite numbers of counts over finite periods of time. In the case of the SAMPIE experiment, it will be assumed that the statistical uncertainties are dominant in the arc count measurements. It will be assumed that the dwell time at each voltage is sufficiently large such that the determination of the time intervals with only finite precision will induce only a small relative uncertainty in the calculated arc rates. Instrumental uncertainties were assigned to the plasma diagnostic variables: 15% for the plasma densities and 25% for the electron temperatures.

Assuming that the occurrence of arcs is random, when the value of the arc counts is low, repeated measurements will distribute themselves about their mean in a Poisson distribution. In the Poisson distribution, the standard deviation is defined as $\sigma = \sqrt{\mu}$ where μ is the mean of the parent population from which each arc count is sampled. If the number of measurements were infinite, the mean would closely approximate that of the parent distribution. However, if only one arc count measurement x is available, $\sqrt{x}$ must be used as an estimate for the standard deviation. Using this distribution, error bars may be placed at one standard deviation from the mean value, providing a 68% confidence level. Similar to the PIX II data analysis [7], the error bars for very low arc counts were calculated using Poisson statistics for small numbers. The minimum and maximum values bounding the mean value with a 68% confidence level for values of the mean below 10 are shown in Fig. 5.2. It should be noted that for a Poisson distribution as the mean increases, the relative error, $\sigma/\mu = 1\sqrt{\mu}$, decreases.

As the mean of the arc counts increases, the symmetry of the Poisson distribution increases and it becomes indistinguishable from a Gaussian distribution. This occurs for values of the mean greater than about 10 [1]. For these values the relative error calculated using the Poisson distribution is very small and does not represent the expected uncertainty in the arc rate measurements. Therefore, for values of the mean greater than 10, the standard deviation σ was calculated from the data assuming a Gaussian distribution. It is given by

$$\sigma = \sqrt{\frac{1}{N-1}\sum(x_i - \bar{x})^2} \tag{5.4}$$

where $\bar{x}$ is the average of the measured arc rates and N is the total number of measurements. Also, for a Gaussian distribution, it is possible to define the standard error σ_μ, or uncertainty of the mean, which is defined by

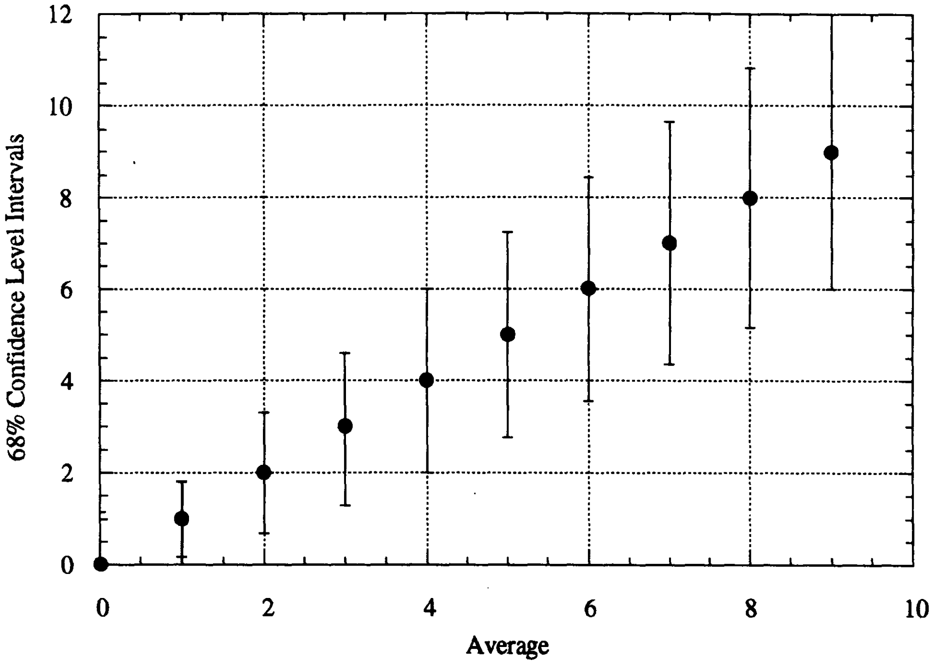

Figure 5.2: Intervals Yielding a 68% Confidence Level

$$\sigma_\mu^2 = \sum \left[\sigma_i^2 \left(\frac{1}{N}\right)^2\right] = \frac{\sigma^2}{N} \tag{5.5}$$

where σ_i is the standard deviation in each measured data point . The estimate of the mean value will improve as the square root of the number of measurements. The SAMPIE data set was limited; there were at most two data points for a given bias voltage. At the voltages above -300 V, where the arc counts exceeded 10 and the standard error could be calculated using Eqn. 5.5, the low number of measurements shows that the estimate of the mean is not precise.

In the following sections, the relationships between the arc rates and the different environmental variables and operational parameters will be examined. If the number of data points was not sufficient to obtain these relationships, a qualitative analysis was performed. The values of the arc rates and parameters used in the data analysis are included in Appendix A. The values of the plasma density and temperature in the ram orientation were corrected using the correction factors described in Chapter 4. The values for these parameters in the bay-to-deep-space orientation were calculated using the IRI-86 model in the EWB software. The rest of the parameters used in the data analysis were those recorded during the experiment.

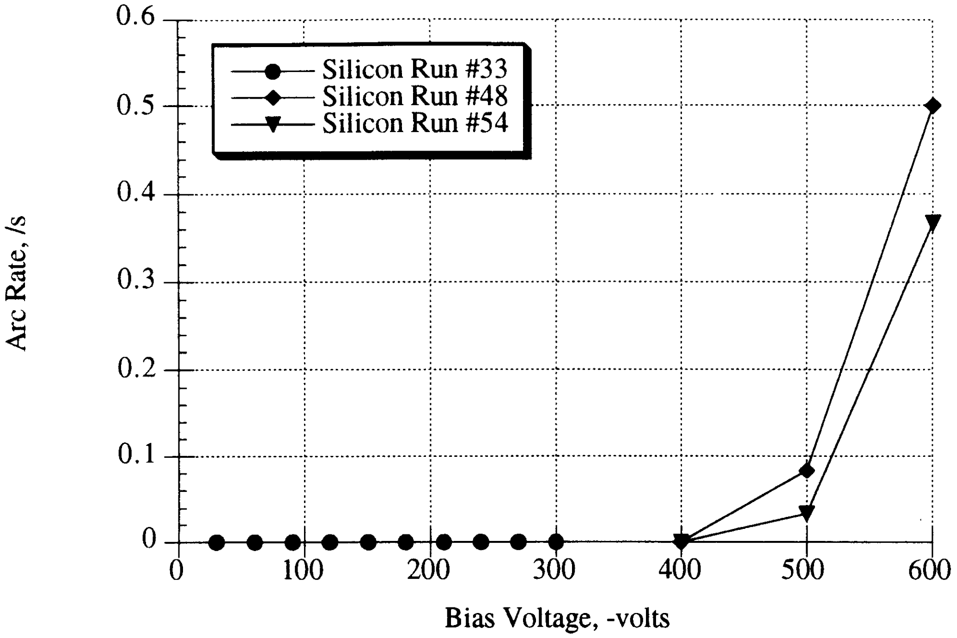

Figure 5.3: SAMPIE Arcing Data for the Silicon Cells

5.3 Data Analysis of Conventional Silicon Cells

The data available from the four-cell coupon of standard silicon cells is shown in Fig. 5.3. The run number is a reference to the particular time during the experiment when a biasing sequence was executed. Due to the anomaly in the HVPS-1 circuit, only one low voltage bias sequence and two high voltage biasing sequences were executed. The behavior of the arc rate with respect to bias voltage is shown in Fig. 5.3. The arcing rates are zero at bias voltages below and including -400 V and they show a sharp increase at the high voltages. The limited data precludes a determination of the threshold voltage, but it supports the conclusion that for bias voltages above -400 V, the silicon cells will arc. Due to the limited number of data points, no correlations were found between the arc rate and the other parameters. Consequently, the arcing data from these cells was used to make qualitative comparisons with other cells.

5.4 Data Analysis of APSA Cells

The data available from the APSA cells is shown in Fig. 5.4. Only one set of measurements exists at each bias voltage. The arc rate recorded at -400 V corresponds to an arc count of one. It is during this run that the anomaly in the circuit occurred and therefore, the number

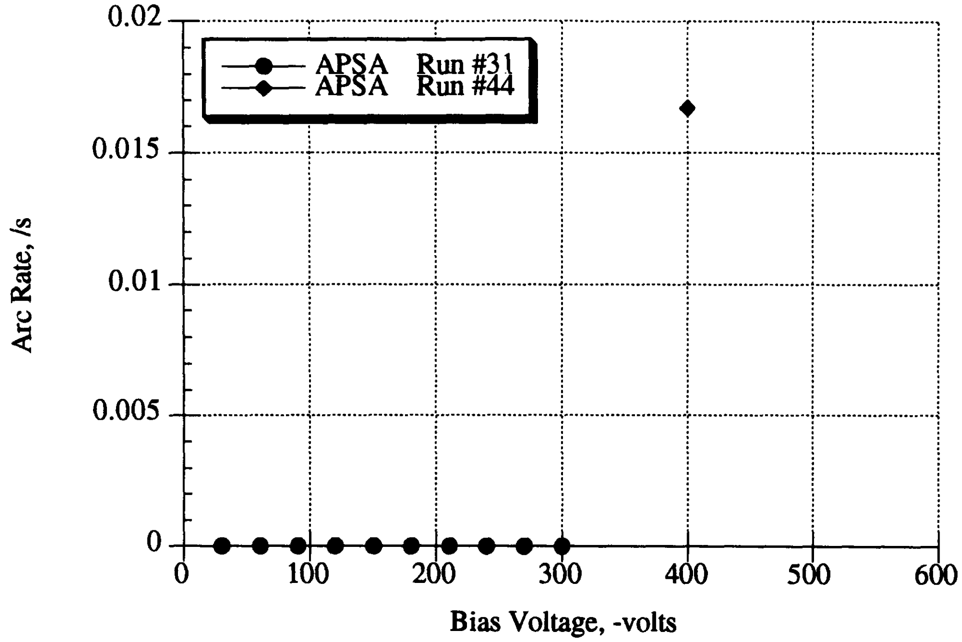

Figure 5.4: SAMPIE Arcing Data for the APSA Cells

of arc counts at this voltage may have been higher. From the model, it is expected that this thinner silicon cell design will exhibit a higher arcing activity than the conventional silicon cells. This behavior can be observed at -400V, where one arc was detected in the APSA cells and no arcing was observed in the standard silicon cells.

5.5 Data Analysis of Metal Coupons

The number of data points for the metal coupons was relatively large compared to that for the other cells. One arcing measurement is available at each voltage of the low voltage bias sequence described in Chapter 3. For each of the metal samples biased at high voltages (-400 V and -500 V), two data points were obtained when the cells were oriented in the ram direction and five data points were obtained in the bay-to-deep-space orientation. Thus, the relatively large number of data points allowed relationships between the arc rates and the different environmental variables and operational parameters to be examined. It is expected that the data from these coupons will agree very well with the model predictions because of the close resemblance of the geometry of the coupons to the geometry assumed by the model. The only difference between the different coupons is the work function of the metal, which represents the interconnector in the model. As suggested by the model, the dependencies of the arc rate on the following experimental parameters were examined:

	Minimum	Maximum
Bias voltage (V)	-30 V	-500 V
Work Function (ϕ_w)	4.26 eV	5.1 eV
Ion Flux (Γ_i)	1.6×10^{14} $m^{-2}s^{-1}$	2.6×10^{16} $m^{-2}s^{-1}$
Neutral density (n_n)	3.7×10^{15} m^{-3}	2.4×10^{16} m^{-3}
Cell temperature (T_s)	268.1 K	288.1 K

A computer program was developed using the Interactive Data Language from Research Systems, Inc. to find the different correlations. To examine the correlation between arc rate and a given parameter, points along the orbit were found where the remaining parameters were constant (using 5% tolerance for the voltages and 15% for the others). A plot of arc rate versus the parameter was then generated. The data points showing anomalous high arc rates, caused by the failure in the HVPS-1 circuit or the concurrent operation of other experiments in the shuttle bay, were ignored.

5.5.1 Dependency of Arc Rate in Cell Temperature

The dependency of the arc rate on the cell temperature could not be determined due to the low number of data points, as well as the limited dynamic range of this parameter, 268 K to 288 K. Fig. 5.5 shows a representative result when the neutral density and ion flux were held constant. A dependency of the arc rate with cell temperature has been observed in the cells biased in the PASP Plus experiment [40]. However, the range of temperatures experienced by the PASP cells was higher than that seen by the SAMPIE cells. For example, the cell temperature of the APSA cells in the PASP Plus experiment varied from 215 K to 330 K.

5.5.2 Dependency of Arc Rate on Neutral Density and Ion Flux

When the effect of the ion flux or the neutral density was studied, the other environmental parameters were not held constant because the data showed two distinct populations, high values of ion flux and neutral density when in ram, and low values when in the bay-to-deep-space orientation. These distinct populations are shown in Fig. 5.6. If one of these two parameters was held constant to study the other, only one of these populations would show and no correlations could be determined.

The neutral flux cannot be quantified from the experimental data, but the neutral density may be calculated from the neutral pressure if a neutral temperature is assumed. Using the EWB software, the average ambient neutral particle density and neutral mass density

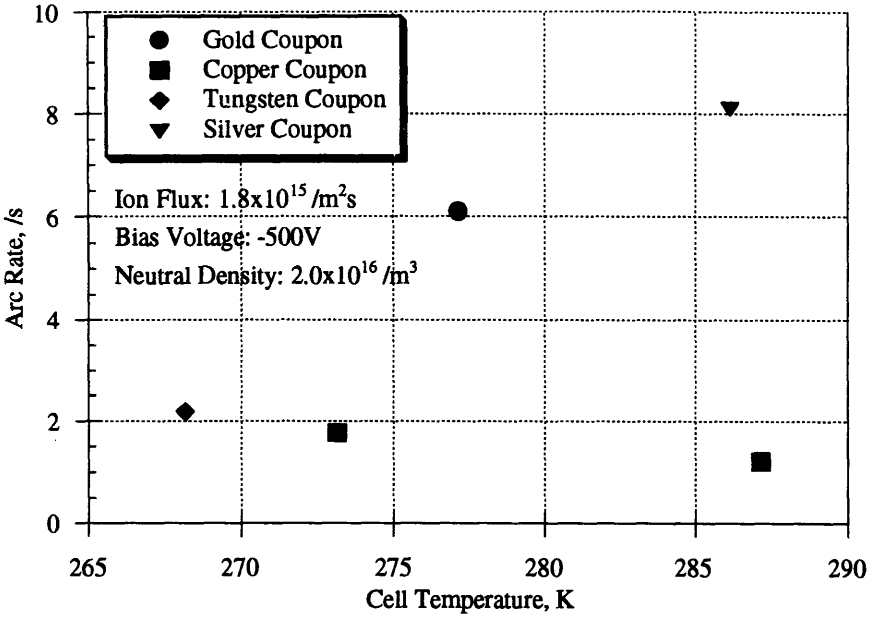

Figure 5.5: Arc rate Dependence on Cell Temperature

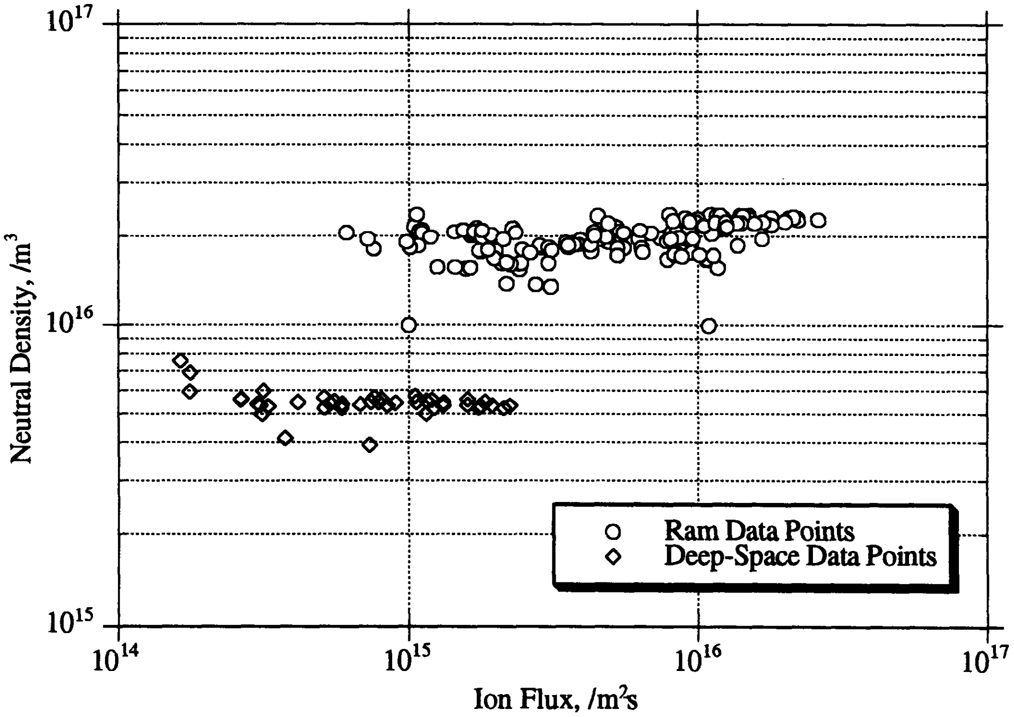

Figure 5.6: Neutral Density and Ion Flux for SAMPIE Arcing Data

during the SAMPIE orbit were 6×10^{14} m^{-3} and 2×10^{-11} kgm^{-3} respectively. Assuming a neutral temperature of 1100 K, the neutral densities calculated from the experimental neutral pressure measurements yielded values about two order of magnitudes larger than ambient density given by the EWB software. This increase in the density surrounding the shuttle has been observed during many shuttle experiments and is attributed to nearby thruster firings.

The behavior of the arc rate with respect to neutral density is shown in Fig. 5.7. The data suggests that there seems to be a neutral density above which the arcing activity increases dramatically, about 5×10^{15} m^{-3}. It is expected that for a given cell temperature and voltage, there will be a critical ambient neutral density above which arcing will always occur once the EFEE emission has started. The critical ambient densities curves for different voltages and the available experimental data in the ram orientation are shown in Fig. 5.8. Cell temperatures were not available for the bay-to-deep-space orientation. The experimental ram data falls in the breakdown region, therefore no dramatic change in the arcing activity at this orientation is expected. The ram experimental data supports this hypotheses. The existence of a threshold neutral density in the experimental data suggests that the bay-to-deep space data points would lay in the curve or in the "no breakdown" region. Since no cell temperatures were obtained in the bay-to-deep-space orientation, the corresponding data points were not plotted, and the predictive capability of the breakdown criterion cannot be validated.

The dependence of the arc rate on the ion flux for all the metal coupons at -400 V and -500 V operation is shown in Fig. 5.9 and Fig. 5.10 respectively. As expected from the model both plots seem to show a critical ion flux above which arcing always occurs. Both plots show a critical ion flux of about 5×10^{14} m^{-2}s^{-1}. The critical flux calculated using Eqn. 5.3 assuming a ΔV_{drop} of 300V, was about 2×10^{13} m^{-2}s^{-1}. To obtain the critical ion flux shown in the data, the average voltage drop would be 1500 V, which is impossible. The range in the bias voltage was not large enough to test the linear dependency of the critical flux with bias voltage, as hypothesized by the model. If the neutral flux and cell temperature were in the breakdown region, the identical critical ion flux at -400 V and -500 V substituted in Eqn. 5.3 suggests the voltage drop is constant for these bias voltages. The statistical fluctuation in the data cannot support the dependency of the critical ion flux on the work function of the interconnector.

In summary, the experimental data supports the existence of a critical neutral density and ion flux. The two distinctive populations shown in Fig. 5.6 preclude the study of the arc rate behavior with respect to only one of these parameters. Therefore, the dependency of the critical ion flux with bias voltage or the agreement of the data with the breakdown

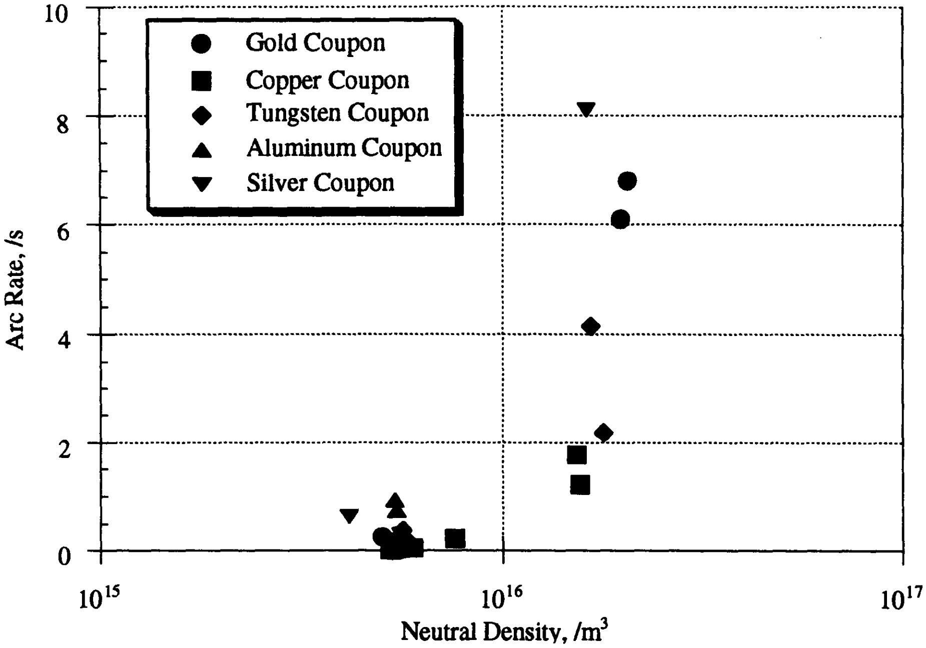

Figure 5.7: Arc rate Dependence on Neutral Density at -500 V

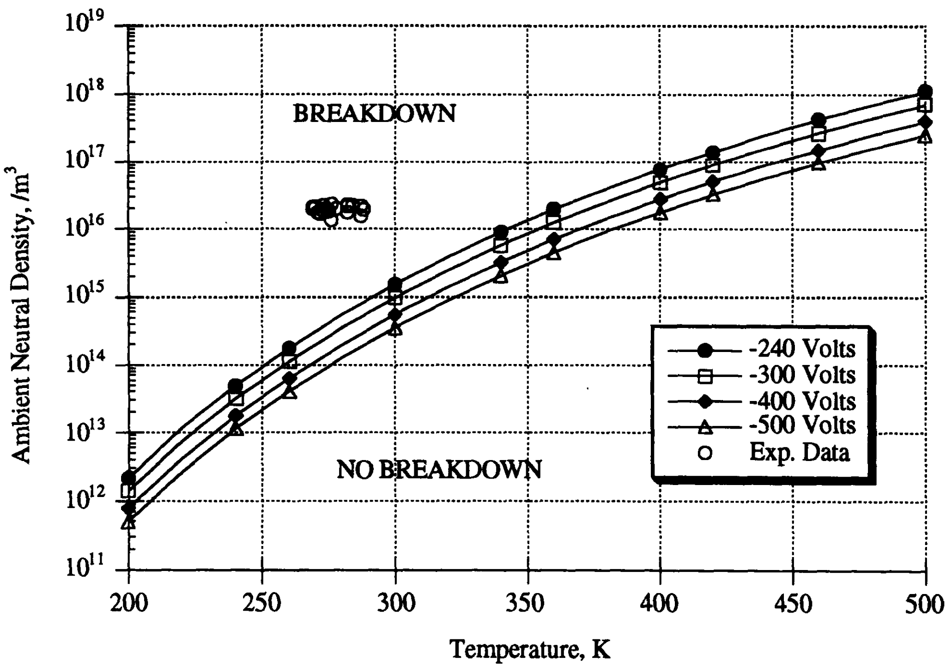

Figure 5.8: Critical Ambient Neutral Density for Metal Coupons and Experimental Data

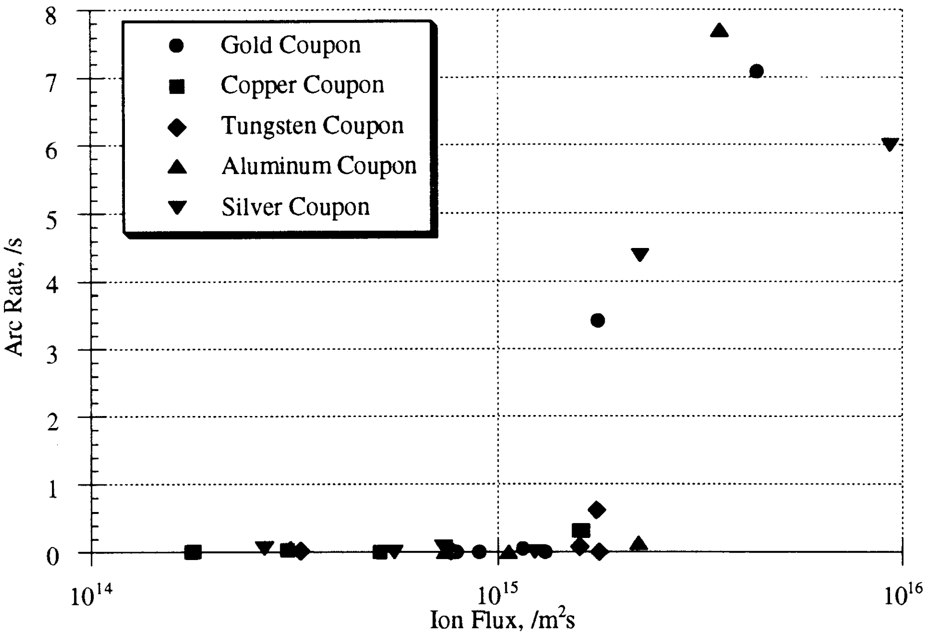

Figure 5.9: Arc rate Dependence on Ion Flux at -400V

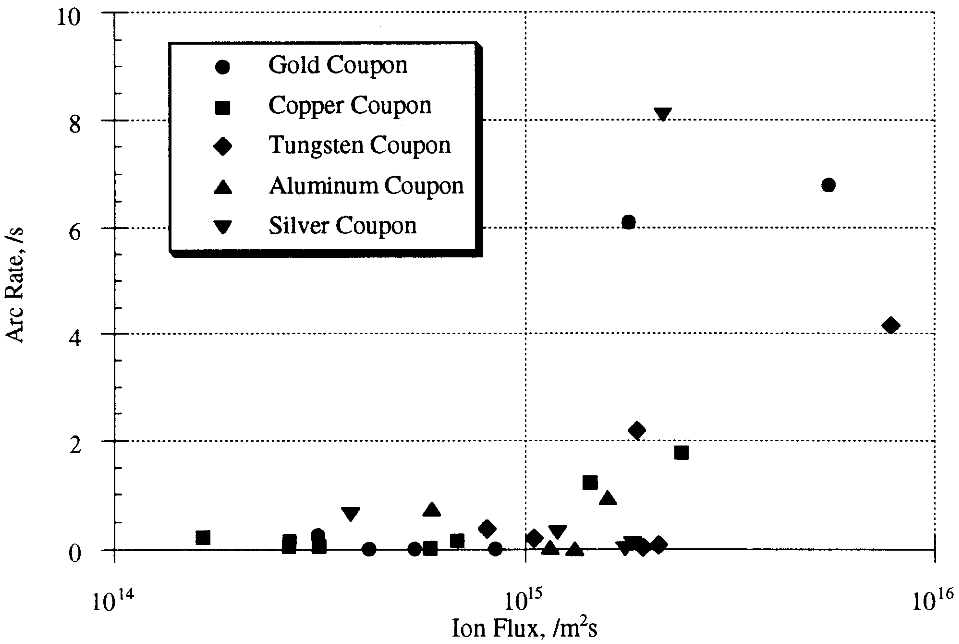

Figure 5.10: Arc rate Dependence on Ion Flux at -500V

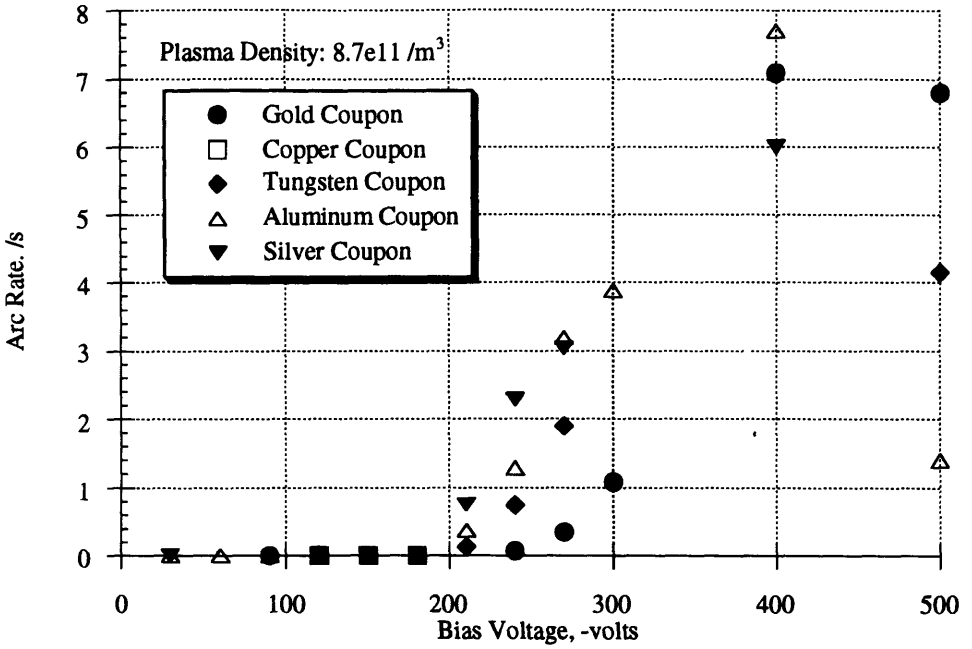

Figure 5.11: Arc rate at points of Constant Plasma Density

criterion predicted by the model could not be determined. Yet, the experimental data does show that as both the ion flux and the neutral density increase, the arc rate increases.

5.5.3 Dependency of Arc Rate on Bias Voltage

The dependency on the bias voltage while keeping plasma density constant was examined in the ram data where the bias voltage ranged from -30 V to -500 V. There is a clear correlation between arc rate and bias voltage, shown in Fig. 5.11. At the low voltages no arcing occurs and beyond the threshold voltage, between -180 V and -210 V, the arcing rate increases dramatically.

The data analysis focused on the determination of the dependency of the arc rate on this parameter. Because the work functions of pure silver and aluminum differ by only 0.02 eV, the data for these coupons was combined to increase the number of data points and, consequently, the statistical significance.

The data was fit using a power law, an exponential form, and the Cho/Hastings model form as given by Eqn. 5.1. The fits were done using a least squares fit to a non-linear equation using the gradient expansion method. The iterations were repeated until χ^2, the goodness-of-fit parameter, changed only by 0.1% or the number of iterations reached 20. Data points indicating anomalous arc counts above 1000 were not included in the data

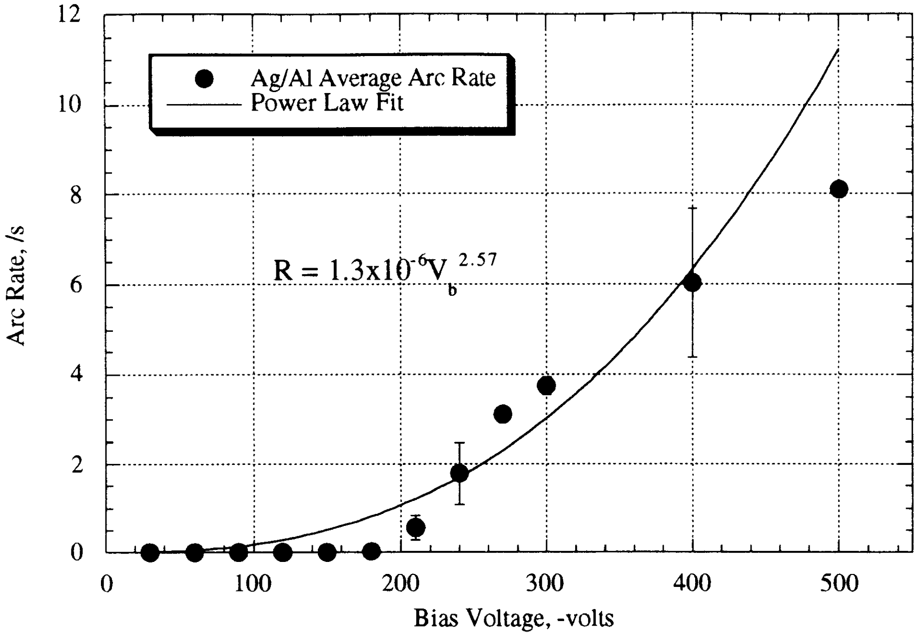

Figure 5.12: Power fit to silver/aluminum data points at constant Plasma Density

fitting. In addition, a very low arc count of 84 for the aluminum sample at -500 V was also discarded. When this data point was included, the power law fits and Cho/Hastings model fits did not converge.

The power law was previously used by Ferguson to fit data for silicon cells in the PIX II experiment [7]. The relationship obtained, given in Eqn. 1.2, showed a dependence of the arc rate on the voltage to the 3.093 power and linear dependency on plasma density. The power law fit for the silver/aluminum coupons and the gold coupon, shown in Figs. 5.12 and 5.13 respectively, yielded the following equations:

$$\dot{R} = 1.3 \times 10^{-6} V_b^{2.57} \quad \text{(silver/aluminum)} \tag{5.6}$$

$$\dot{R} = 5.7 \times 10^{-7} V_b^{2.6} \quad \text{(gold)} \tag{5.7}$$

The exponential fit is derived from the simple form of the Cho/Hastings model as given by Eqn. 5.1. When the bias voltage is low, the exponential term will dominate and the equation can then be rewritten as

$$\dot{R} = \frac{1}{c_0 \exp(\frac{c_1}{V_b})} \tag{5.8}$$

For the metal coupons, coefficients c_0 and c_1 vary only with the work function since they

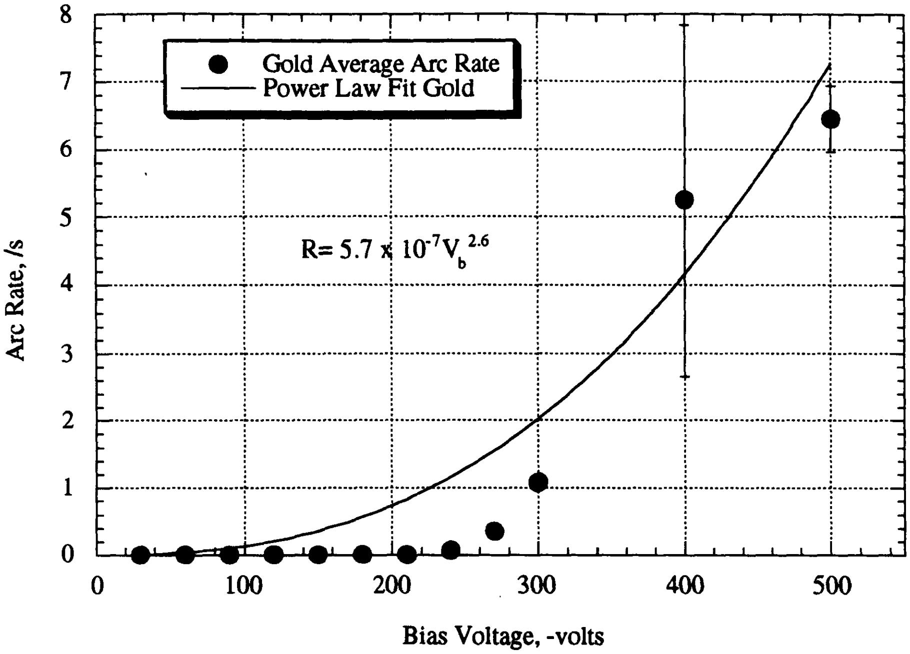

Figure 5.13: Power fit to gold data points at constant Plasma Density

include the Fowler-Nordheim coefficients. A preliminary study, shown in Fig. 5.14, shows the arcing activity of the metals at different environmental conditions at low voltages, below -300 V. At -300 V the slope of arc rate curve starts to decrease and no longer exhibits the predicted exponential behavior. The exponential dependency of the arc rate on the work function is expected to be more prominent at the lower voltages. As expected from the model, the metals with higher work functions arced less than those with lower work functions. This behavior, as expected from the model, is prominent at voltages below -270V. Above -270V, the aluminum coupon exhibits a higher arcing rate than the silver coupon with has a lower work function. It is interesting to note that the arc rates of the copper sample and the gold sample were nearly identical, yet their work functions differ by 0.35 eV.

The exponential fit to the silver/aluminum coupon data at lower voltages, shown in Fig. 5.15, yielded the following equation

$$\dot{R} = \frac{1}{0.005\exp(\frac{1152}{V_b})} \quad \text{(silver/aluminum)} \tag{5.9}$$

This exponential form provides a good fit, but if the average values of parameters such as β and S_{FN} are substituted in the τ_{efee} expression, the coefficients c_0 and c_1 are not physically significant. The coefficients, c_0 and c_1, from the exponential fit for a given work function, ϕ_w, scaled for a different work function, ϕ_{w_2}, yield the new coefficients, c_{0_2} and c_{1_2}, given

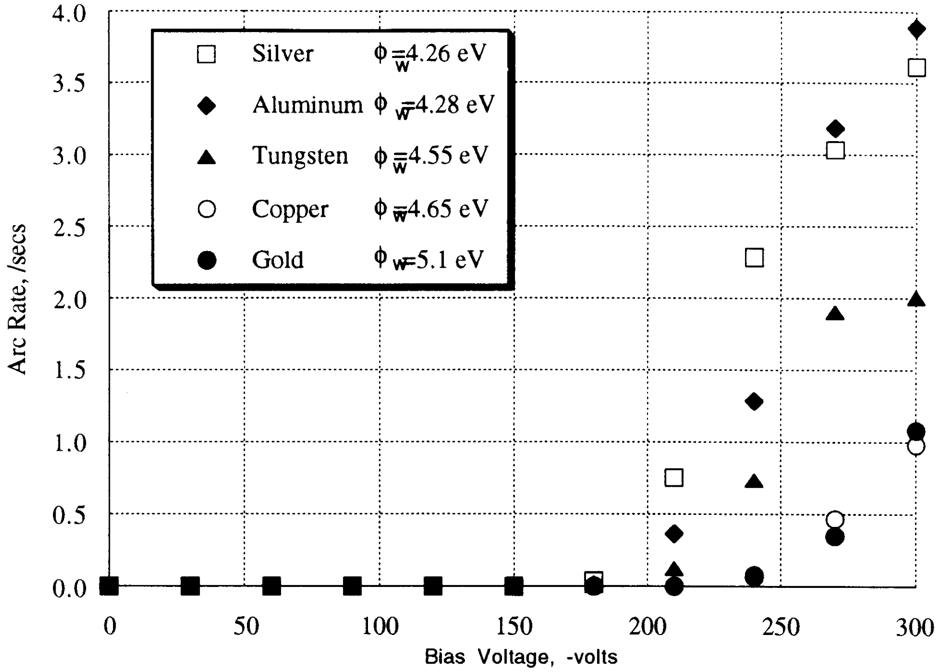

Figure 5.14: Arc rate experimental values for the different metal coupons

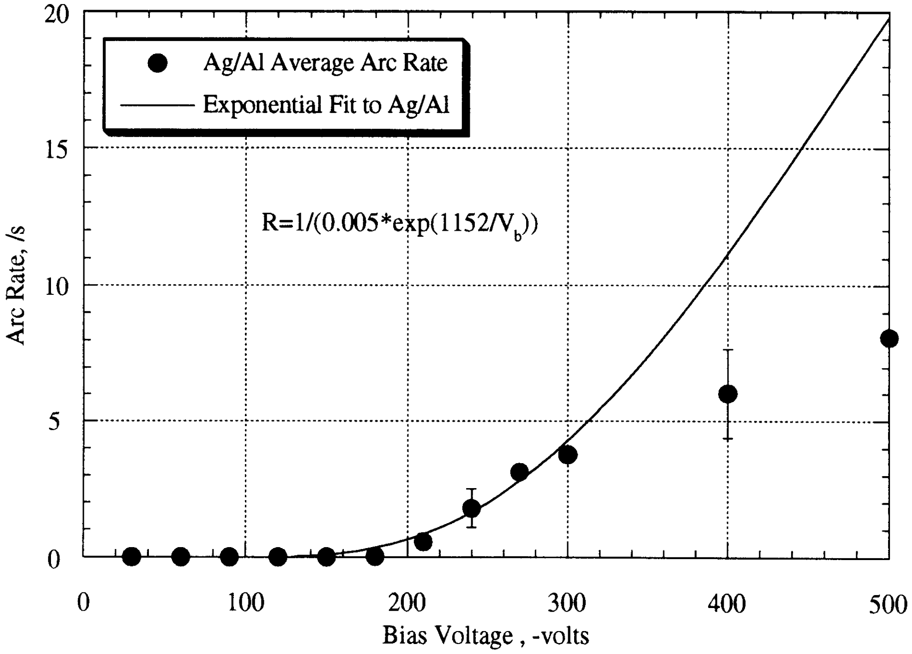

Figure 5.15: Exponential fit to Ag/Al combination

by

$$c_{1_2} = \left(\frac{\phi_{w_2}}{\phi_w}\right)^{1.5} c_1 \tag{5.10}$$

$$c_{0_2} = 10^{-4.52(\frac{1}{\sqrt{\phi_w}} - \frac{1}{\sqrt{\phi_{w_2}}})} (\frac{\phi_{w_2}}{\phi_w})^{1/2} c_0 \tag{5.11}$$

If the coefficients from the exponential fit to the silver/aluminum combination are accordingly scaled for the work function of gold, ϕ_w=5.1 eV, and the work function of tungsten, ϕ_w=4.55 eV, the lower curves of Fig. 5.16 are obtained. Both curves seem to fit the data well. Unfortunately, a photograph of the samples taken after the flight revealed that the some of the samples may have oxidized. The placement of the samples is shown in Fig. 5.17 and the photograph is shown in Fig. 5.18. The photograph suggests that the silver sample and the copper sample were oxidized. The work functions of the oxides are shown in Table 4.2. It should be noted that the work function of copper oxide is very close to that of gold, which may explain the nearly identical arc rates observed for these coupons. Since the arc rates of the silver and aluminum were very close, the work function of the aluminum sample was set to that of the silver oxide. Using the new work functions for the oxides, the scaled curves from the aluminum/silver exponential fit to the other samples no longer seems to fit the data well. The scaling of the exponential fit to the gold data points assuming the silver/aluminum combination was oxidized is shown in Fig. 5.19. If, on the other hand, the work function of the pure aluminum/silver is scaled with respect to that of the oxidized copper sample, the scaled curve shown in Fig. 5.20 fits the copper data well, indicating that copper oxidized. The scalings suggest that the silver and aluminum samples may not have oxidized completely. Another explanation maybe that the work function of the metal has changes due to adsorption of gas on the surface [35]. The effect of the adsorbed gas was not included in the semi-analytical model. The change in ϕ_w depends strongly on the binding state, and for the same combination of gas and solid, one adsorbing state gives an increase of ϕ_w, while others give a decrease. Therefore, it is possible that the aluminum sample did oxidize, but the adsorbed gas on its surface reduced its work function to a value close to that of pure aluminum.

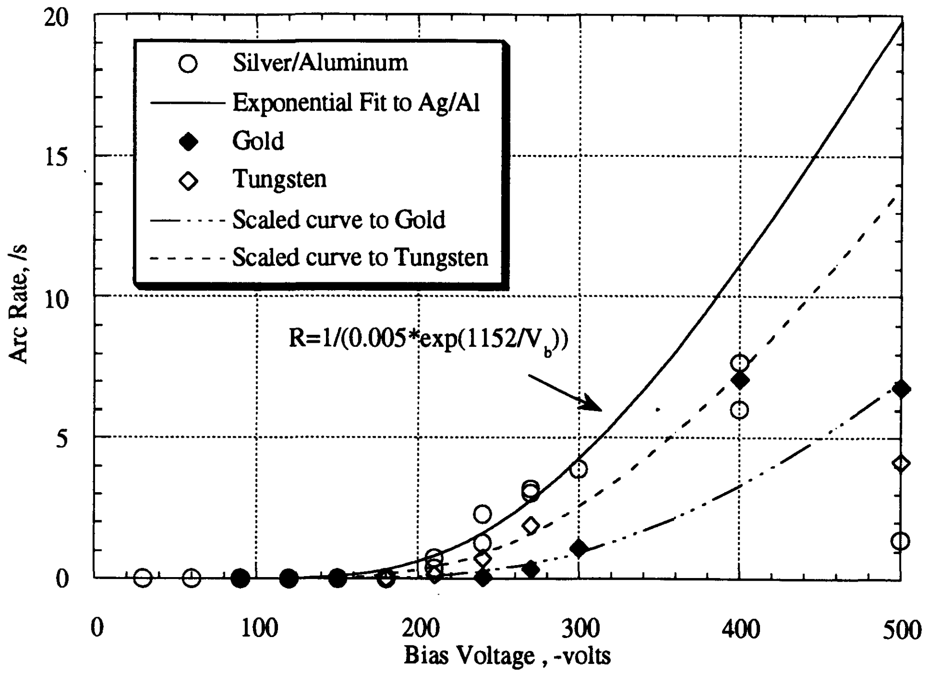

Figure 5.16: Exponential fit to Ag/Al combination and scaled curves for gold and tungsten

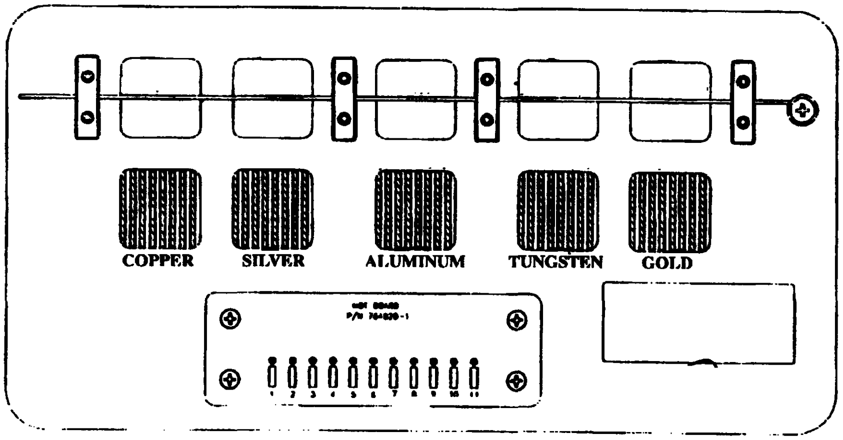

Figure 5.17: Metal Coupons

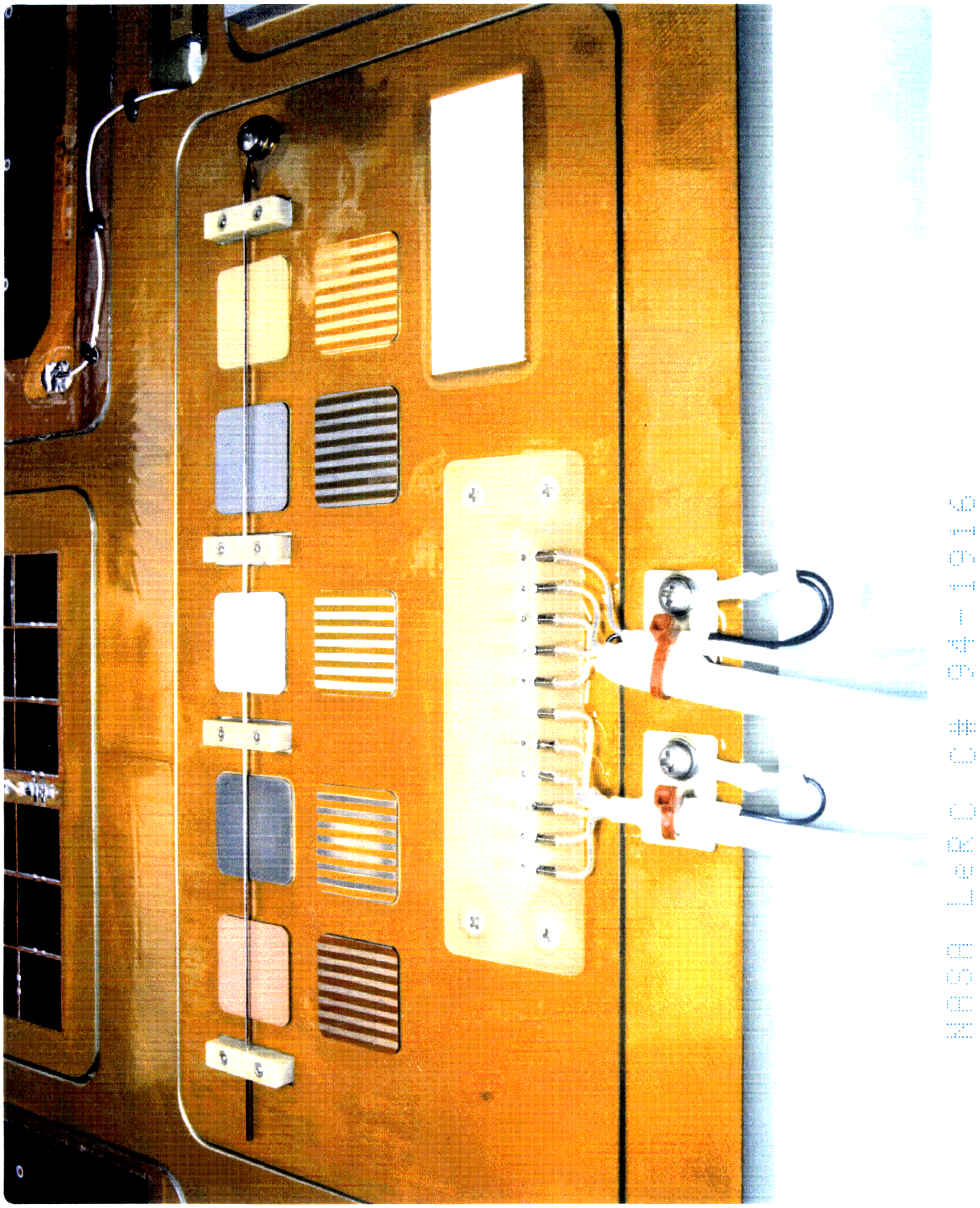

Figure 5.18: Photograph of the Metal Samples after the Flight Experiment

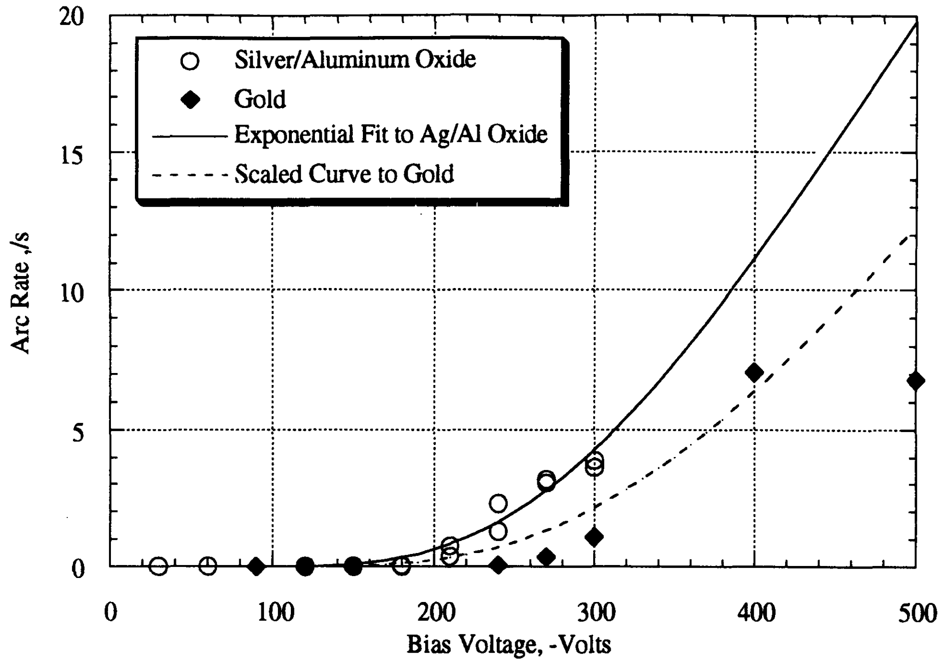

Figure 5.19: Exponential fit to Ag/Al oxide combination and scaled curves for gold

The exponential form overpredicts the experimental values at the high voltages. Therefore, an additional term is needed in the denominator of Eqn. 5.8 to lower the arc rate values at the high voltages. The functional form suggested by Eqn. 5.1 contains this additional term and was also used to fit the data. Using the values of the coefficients obtained in the exponential fit, a value for the coefficient of the τ_{ion} term was found. The resulting fit yielded the following equation and is shown in Fig. 5.21.

$$\dot{R} = \frac{1}{0.005\exp(\frac{1152}{V}) + 0.00014V_b} \text{ (silver/aluminum)} \qquad (5.12)$$

This functional form also provides a good fit to the data. Again, the τ_{ion} coefficient found cannot be supported physically. The fit and the curve obtained when the fit is scaled for the gold's work function are shown in Fig. 5.21. As shown above, if the oxide work functions are used, the quality of the fits decreases. This fit differs from the other fits in that it shows a decrease in slope at the higher voltages, which can be supported physically but cannot be guaranteed by the data.

Although the coefficients are not physically supported, a further scaling with ion flux was made using this functional form. All the data points in the bay-to-deep-space orientation were biased at -400 V or -500 V. Thus, a fit of the form suggested by Eqn. 5.1 using only these data points was not possible. On the other hand, Eqn. 5.12 may be scaled to account

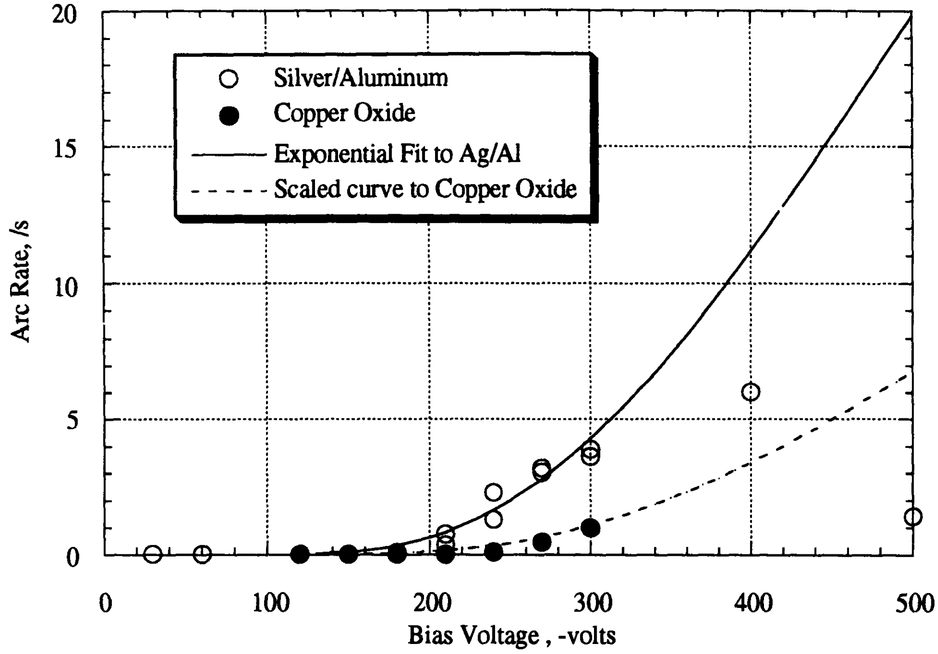

Figure 5.20: Exponential fit to Ag/Al combination and scaled curves for oxidized copper

for the lower ion flux in the bay-to-deep-space orientation. The only term affected by the ion flux is τ_{ion}, which is inversely proportional to it. From the SAMPIE diagnostic data, the ion flux decreased by about two orders of magnitude. Eqn. 5.12 scaled to the maximum and minimum ion fluxes encountered in the bay-to-deep-space orientation is compared to the experimental data in Fig. 5.22. The scaled curves predict the arcing activity at lower ion fluxes very well.

Three different functional forms were used to fit the arcing data from the metal samples. The limited number of data points obtained at each voltage was not sufficient to determine the equation describing the relationship between arc rate and bias voltage. The functional forms provided equally good fits. It is important to note that both the exponential and the Cho/Hastings model fit show an onset voltage at approximately -180 V, which seems to be supported by the data. The coefficients from these fits cannot be interpreted physically. Yet as expected from the model, these coefficients scale with the work function at the lower voltages and with ion flux at the higher voltages. Since the coefficients cannot be supported physically, these coefficients cannot be used to predict the arcing activity of other cells. Yet, when the semi-analytical code is used and parameters such as β and S_{FN} are chosen randomly from a distribution, the predicted maximum and minimum arc rate predictions bound the data very well. The arcing code was used to predict the arcing activity of the

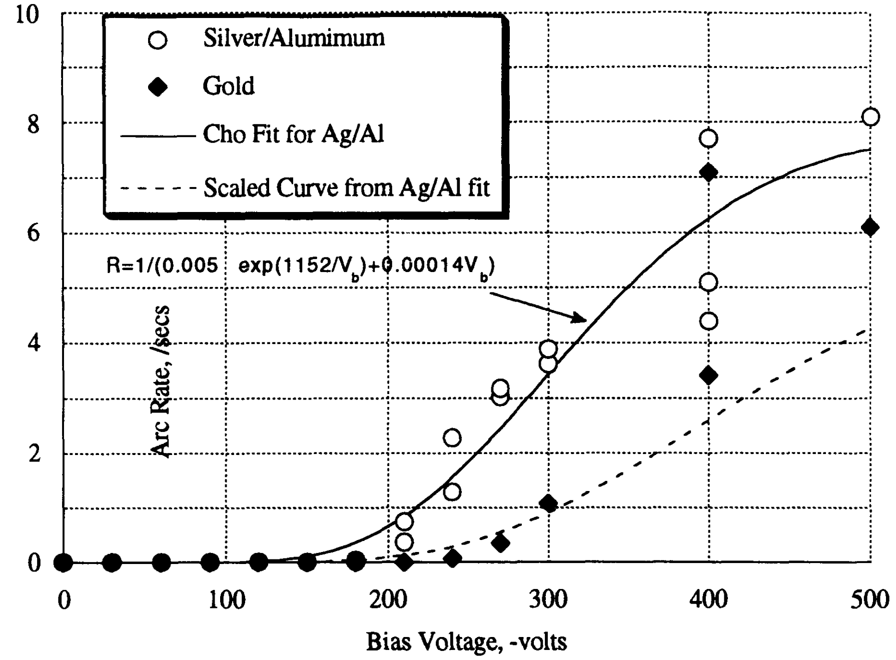

Figure 5.21: Cho/Hastings simple fit to Ag/Al combination and scaled curve for gold

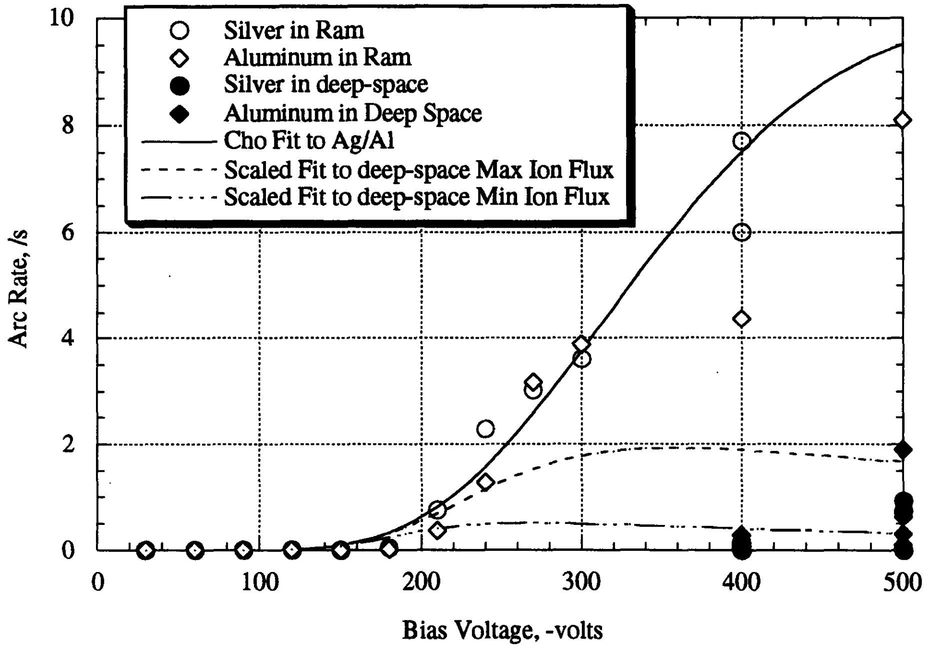

Figure 5.22: Cho/Hastings simple fit to Ag/Al combination and scaled curve for ion fluxes

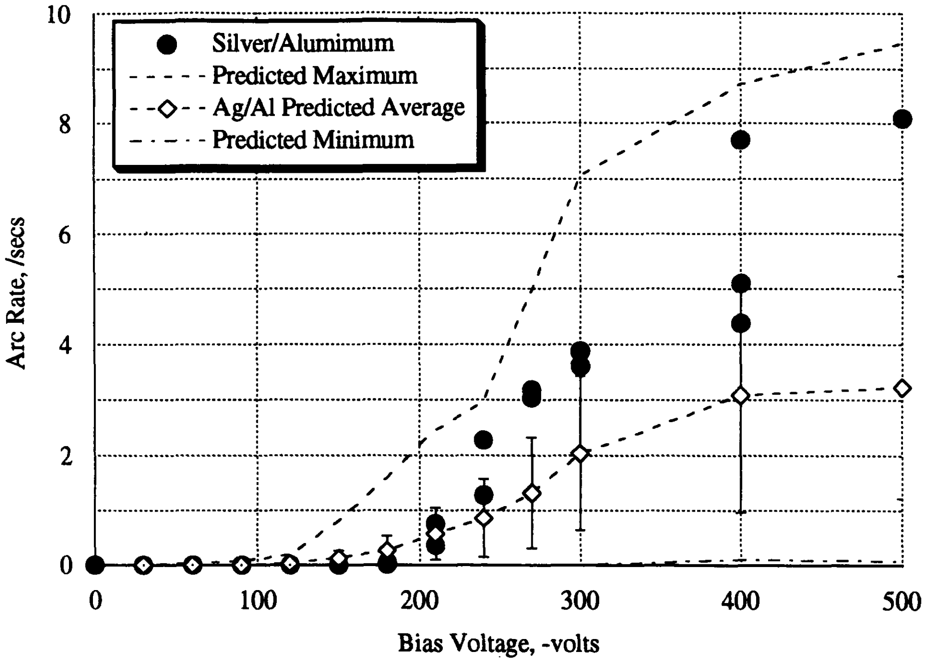

Figure 5.23: Comparison of Ag/Al Experimental Data and Numerical Arc Rates β=200

silver/aluminum combination and the gold cells from Fig. 5.21. The code was run 100 times with an average β value of 200, and from these runs, the maximum, minimum, average and standard deviations of the predicted arc rates were calculated. The results are shown in Figs. 5.23 and 5.24 respectively. At the higher voltages, the experimental data falls outside of the one standard deviation error bars. At the lower voltages, below -240 V, the code predicts the arcing activity very accurately. The maximum and minimum expected arc rates bound all the experimental data except one data point at -400 V for the gold sample. The low predicted average values indicate that the values for the number of emission sites or the average field enhancement were larger than those assumed in the code. If the field enhancement factor is increased to 300, the predicted arcing rates increase and most of the data points fall within the one standard deviation error bars, shown in Fig. 5.25.

Therefore, there are two possible ways to predict the arcing rates for a given cell: to scale the coefficients from fits to this cell under a different ion flux or with a different interconnector material, or to use the semi-analytical code. The former way is limited since only data tabulated from flight experiments could be used, but in a given flight experiment data would need to be recorded only at a particular ion flux and the arcing activity at the other fluxes could be calculated from the observed behavior. The maximum and minimum predictions from the semi-analytical code can predict the arcing activity of most cells under different environmental conditions.

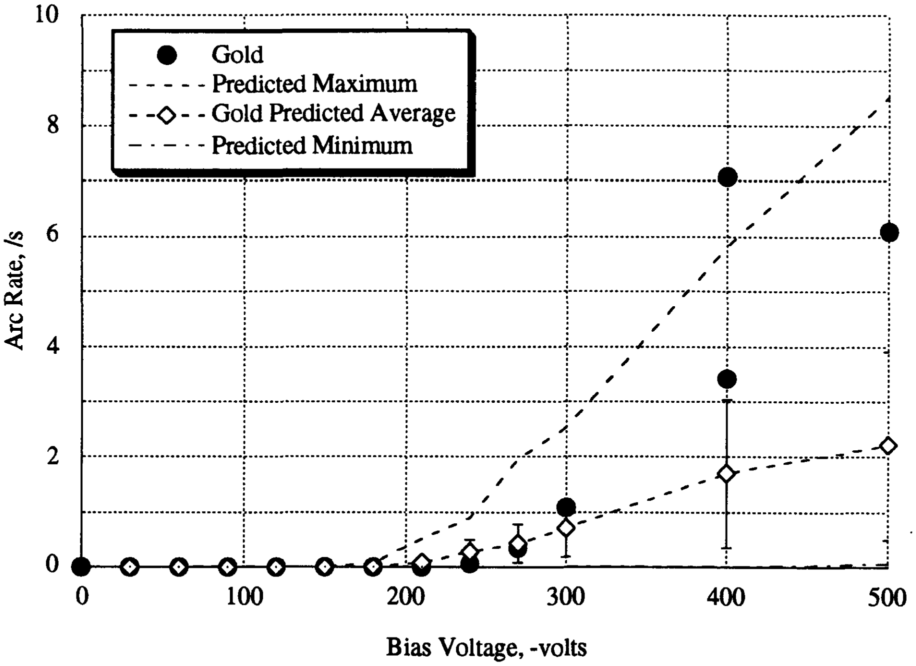

Figure 5.24: Comparison of Gold Experimental Data and Numerical Arc Rates

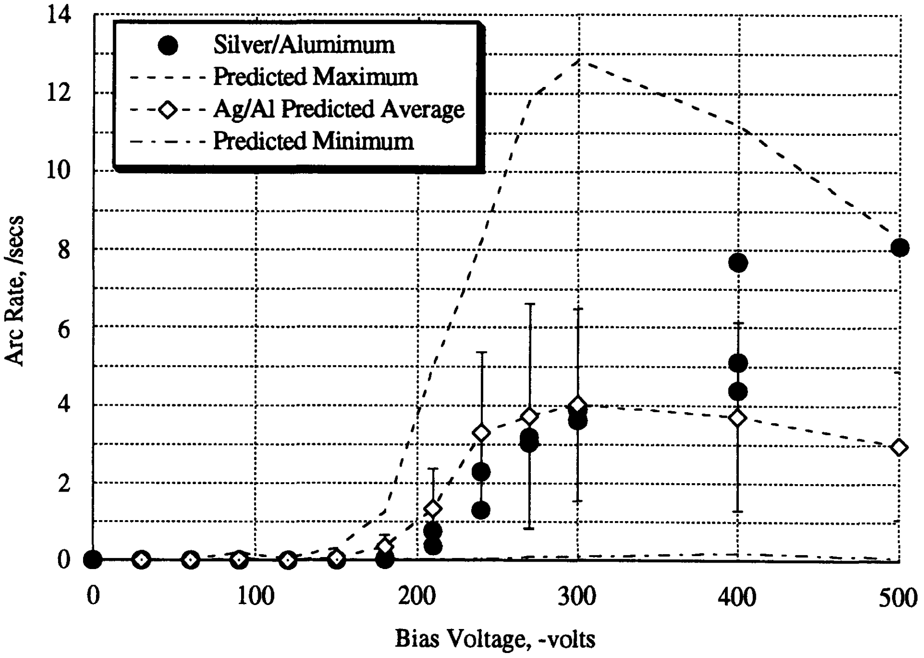

Figure 5.25: Comparison of Ag/Al Experimental Data and Numerical Arc Rates β=300

5.6 Data Analysis of Wrap-Through-Contact Cells

The data available from the WTC cells is shown in Fig. 5.26. As described in Chapter 3, SAMPIE biased four different sets of WTC contact cells. The large Space Station cells are designated as SS. The set of modified cells completely sealed with adhesive expect for specified lengths is designated by SSMIN1. SSMIN1,1 refers to the cell with no adhesive removed and SSMIN1,4 refers to the cell with 32 mils removed. SSMIN3 refers to the set of modified cells in which the overhang length of the coverglass was varied. The cell with no overhang, used as a control, is designated by SSMIN3,1, while the SSMIN3,4 refers to the cell with the maximum overhang, 279.4 μm, 11 mils. Lastly, the four modified Space Station cells that were shorted together are referred to as SSMIN2. The run number indicates the particular time during the experiment when a biasing sequence was executed and the second number indicates the number of times the run was executed. In some cases the runs using the same sequence for the same cell were denoted by the same symbol. Furthermore, low voltage runs with zero arc rates at each bias voltage were shown with an open circle and the high voltage runs by an open square. Almost all of the cells showed no arcing at voltages lower than -300V bias.

The flight data obtained for the WTC cells was also limited and therefore only qualitative comparisons could be made. Due to the limited data, all the data was examined as if it were under similar environmental conditions. This assumption may induce some errors in the analysis. A comparison of the arcing activity of the silicon cells and the WTC cells is shown in Fig. 5.27. The WTC cells used as a control in the overhang study, SSMIN3,1 experiment arced at a surprisingly low voltage of -240 V. At the larger bias voltages, the experimental scatter is very wide. In one run (#46), the SS cells arced very little at -600 V, while on another run (#52), the arc count was as large as the conventional cells (runs #48, #54). This suggests that the arcing problem has not been eliminated by shielding the interconnectors from the ambient plasma.

If the arc rates for each cell of Fig. 5.27 are normalized by the area, as suggested by the conventional geometry model, the arcing activity of the SS cells and silicon cells can be compared. Normalizing by the area of the silicon cells, Fig. 5.28 is obtained. The arcing activity exhibited by the SS cells is now much lower than that of the silicon cells, indicating that these cells may indeed have reduced arcing rates.

The dependency of cell area can be examined between the SS cells and the modified SS cells used as controls in the arcing mitigation experiments. The model predicts that the arc rate will scale linearly with the area. The comparison is shown in Fig. 5.29. It is interesting

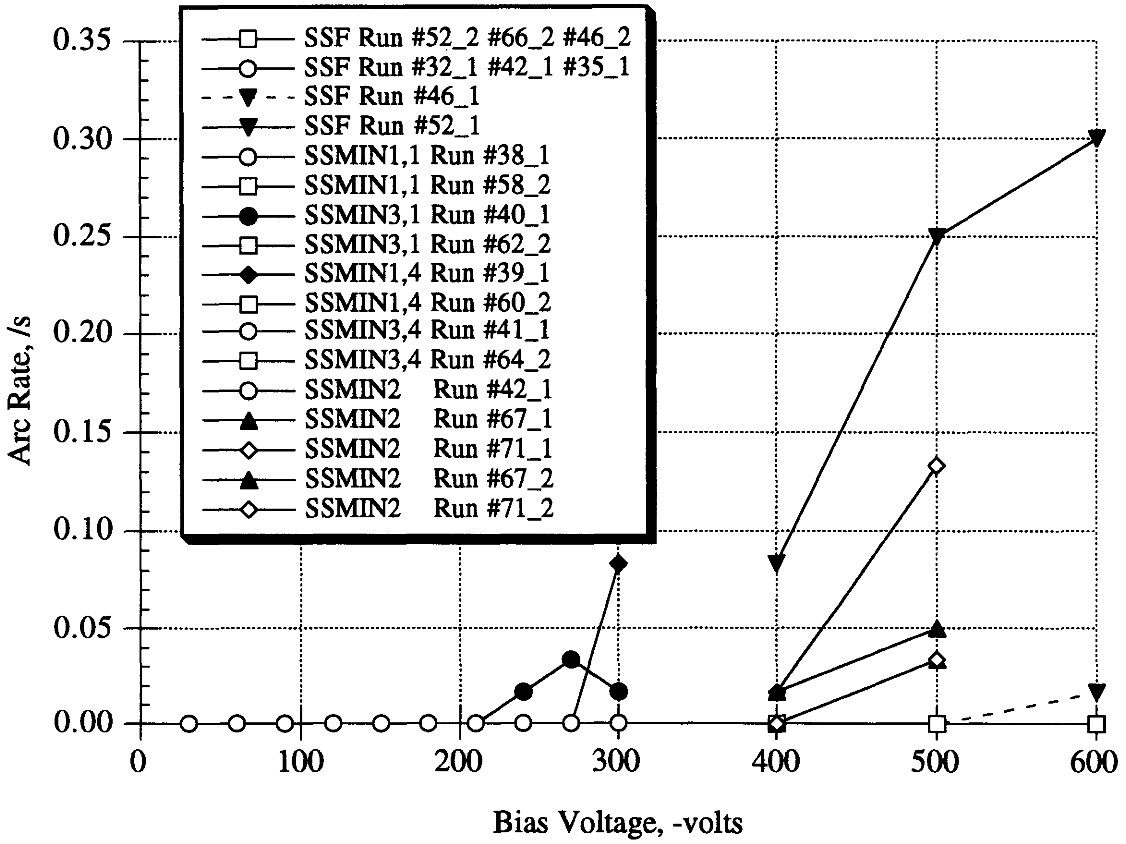

Figure 5.26: SAMPIE Arcing Data for the WTC Cells

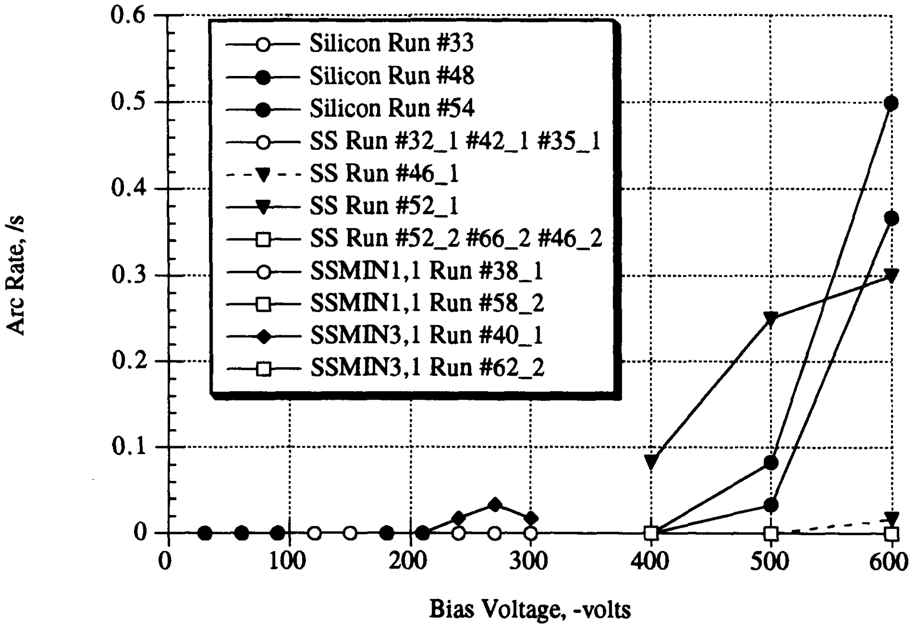

Figure 5.27: Arcing Activity of Silicon and Space Station Cells

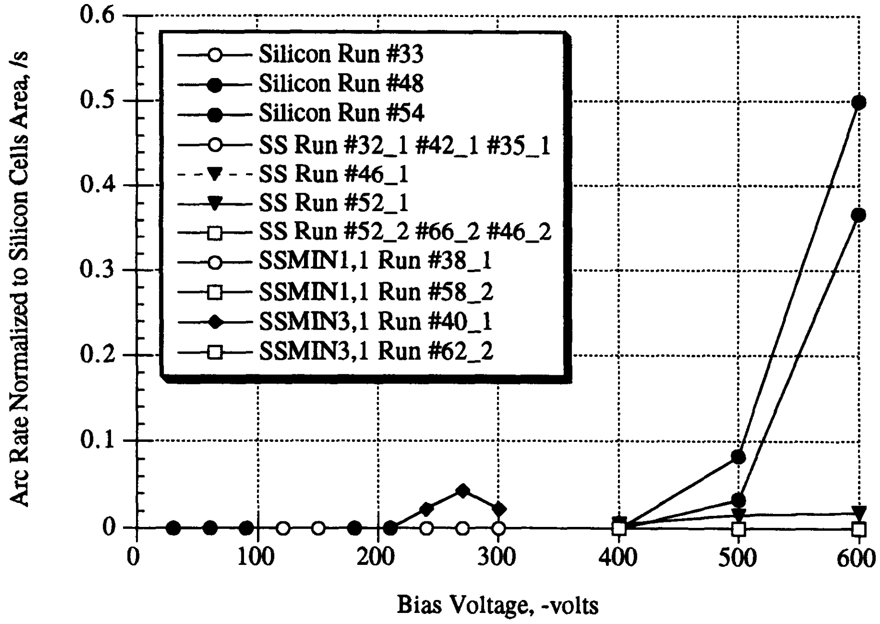

Figure 5.28: Normalized Arcing Activity of Silicon and Space Station Cells

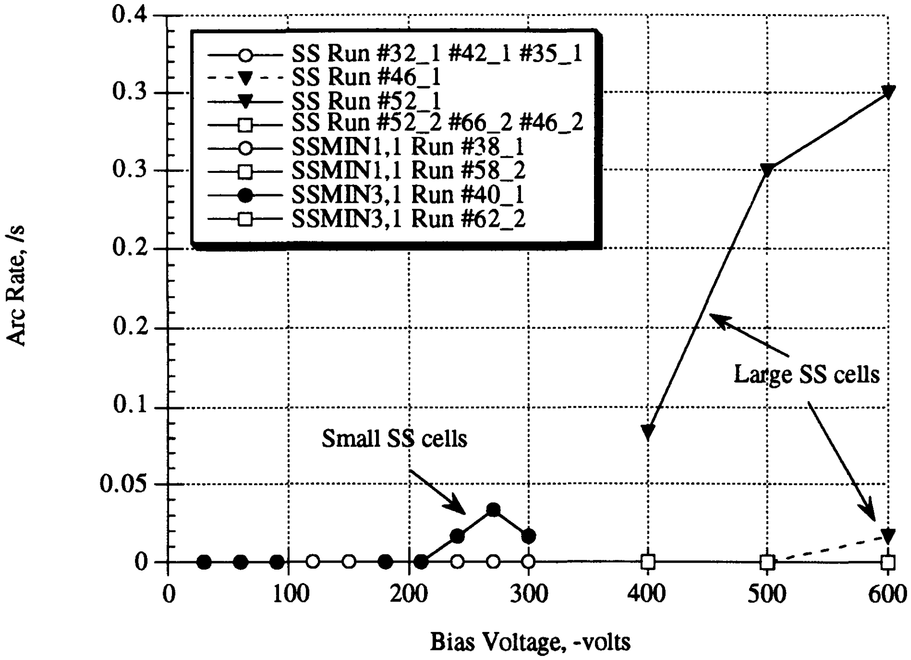

Figure 5.29: Dependency of Arc Rate on Cell Area for WTC cells

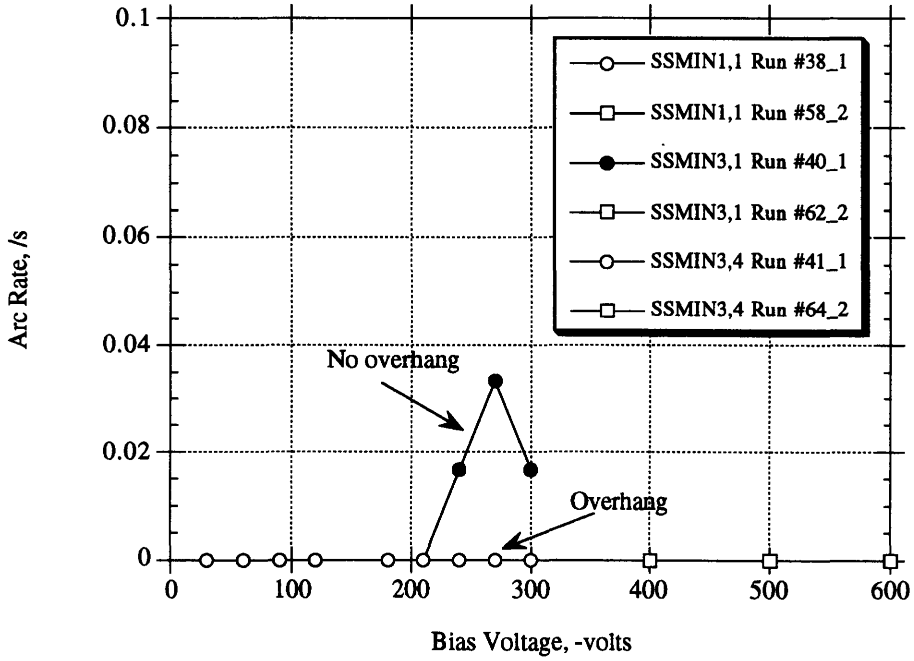

Figure 5.30: Effect of Overhang in the Arcing Activity of WTC Cells

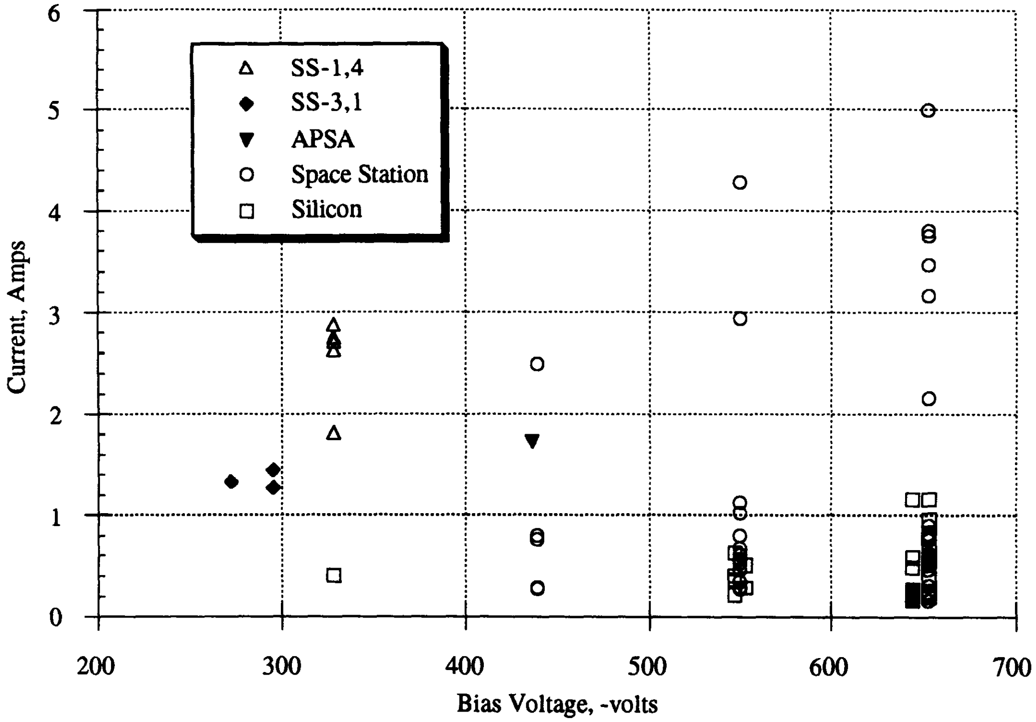

Figure 5.31: Peak Current in the Arcs Recorded by HVPS-1

to note that the SSMIN3,1 cells (#40_1) arc at the low voltages while the SS cells, with an area 20 times greater, show no arcing. At the high voltages the modified cells show no arcing and therefore no scaling can be observed.

Lastly, the effect of creating an overhang will be examined as a method of arcing mitigation. The model predicts substantially reduced arcing activity for a conventional cell if the coverglass extends by a length greater than a critical length. It is expected that the overhang will have the same effect in WTC cells. The data used to examine this effect is shown in Fig. 5.30. At low voltages the cells with no overhang showed arcing while those with the 11mils overhang showed no arcing, suggesting that the overhang may have an effect. At the high voltages, all the cells showed no arcing; thus no comparisons could be made.

5.6.1 Arc Strengths

The strength of an arc is measured by the current it draws from the electrical circuit. Multiplying this current by the voltage drop incurred during the arc gives an estimate of the power loss. The peak current and the half-width of the current profiles were recorded for those cells biased by the HVPS-1. The peak currents are presented in Fig. 5.31. The large number of data points of the silicon and WTC cells allowed comparisons between these cells to be made. The arc strengths were compared by the power per unit area, a measure of the damage to the cell. In the calculation of the power per unit area, the arcs were assumed to be

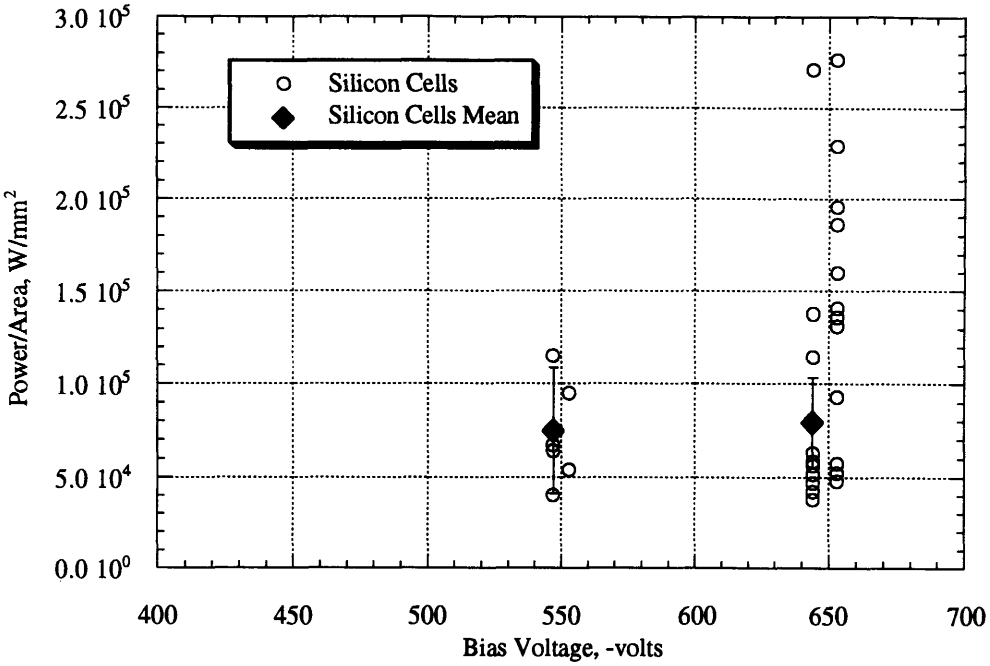

Figure 5.32: Power per unit area in Arcs in the Silicon Cells

a column of charge with a diameter of 0.1 microns and a height equal to the total thickness of the dielectrics. It was also assumed that during an arc the voltage would drop from the bias voltage to a steady value of -200 V. The power per unit area as a function of voltage for the silicon and WTC cells is shown in Fig. 5.32 and Fig. 5.33 respectively. The average power per area in arcs occurring in SS cells is larger than in the silicon cells. The error bars in each plot are three standard errors away from the mean. In both plots, some arcs fall outside of the error bars, indicating that there is a second population of arcs. The two arc populations at -650 V for the silicon and SS cells are shown in Figs. 5.34 and 5.35 respectively. Assuming an average arc duration of 1μs and that the dielectric is silicon dioxide, an estimate for the depth of the dielectric vaporized by the arcs can be calculated for the range of power per area obtained. As shown in Fig. 5.36, the arcs in the upper distribution of the silicon cell data can vaporize 0.08 mm while those in the lower distribution can only vaporize 0.02 mm. The low and high power arcs in the APSA cells will vaporize dielectric thickness of 0.04 mm and 0.31mm respectively. The damage caused by the arcs can be detected with the human eye. A study of the surface of these cells would determine the strength of the arcs.

The limited flight data obtained for the WTC cells allowed only qualitative comparisons to be made. The SS cells show a reduced arcing activity when compared to the conventional silicon cells if the arcing rate is assumed to vary linearly with cell area. Yet, the arcing activity is not completely suppressed with this new type of cell. The effect of cell area could

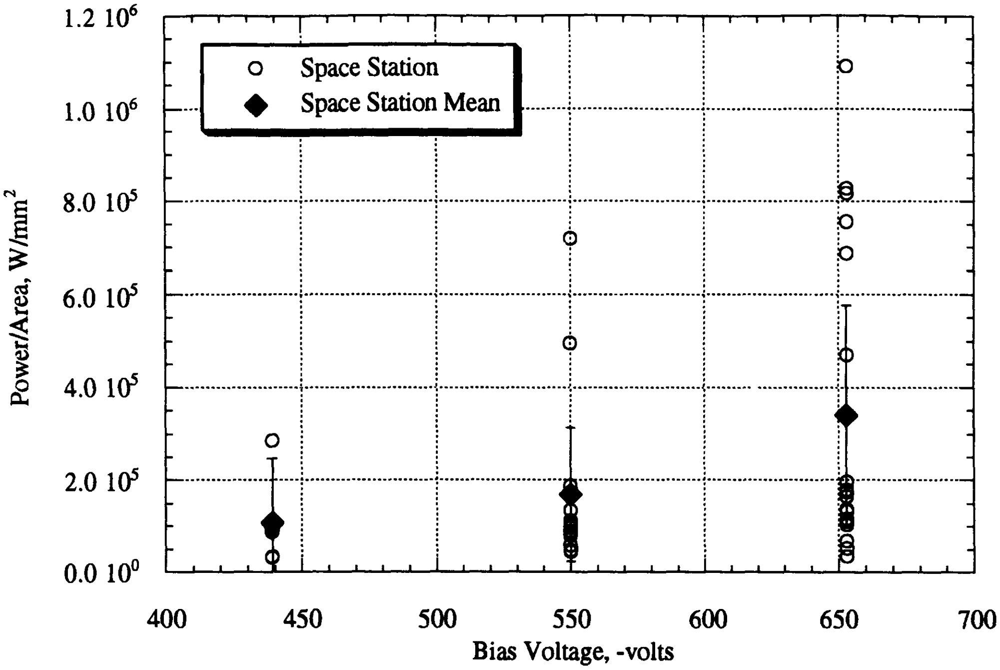

Figure 5.33: Power per unit are in Arcs in Space Station Cells

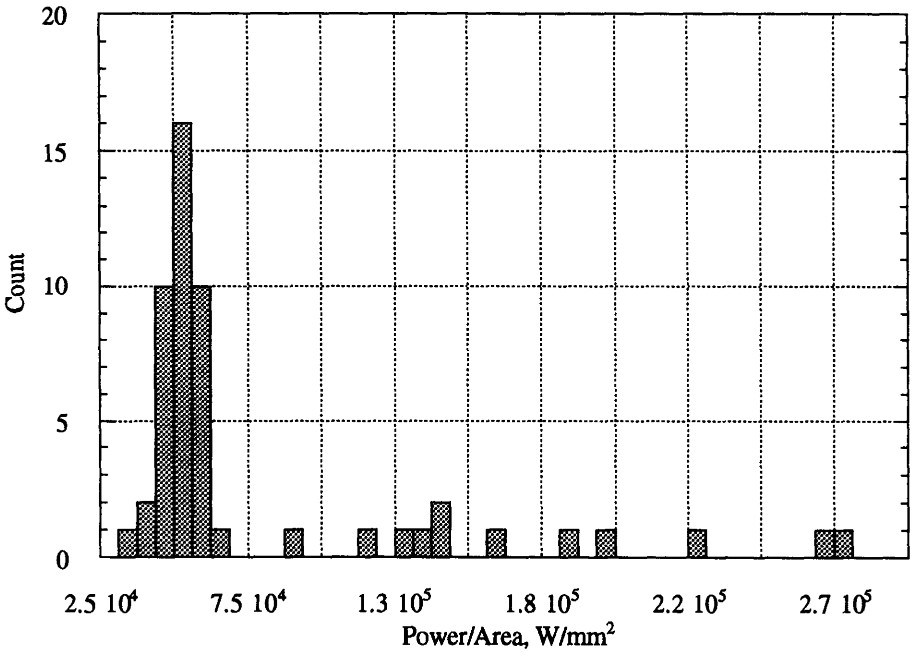

Figure 5.34: Arc Populations in the Silicon Cells at -650V

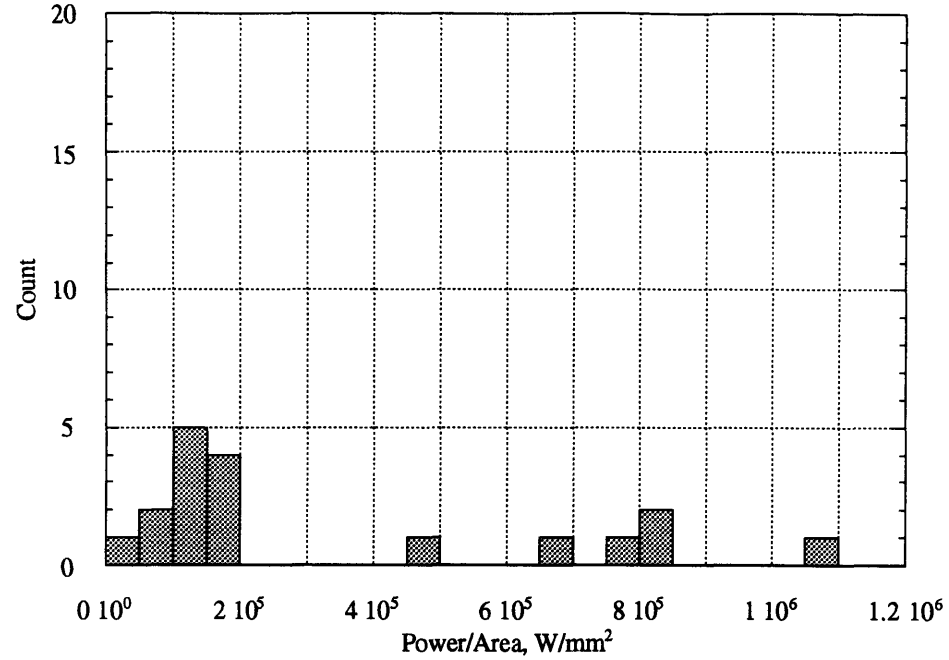

Figure 5.35: Arc Populations in Space Station Cells at -650V

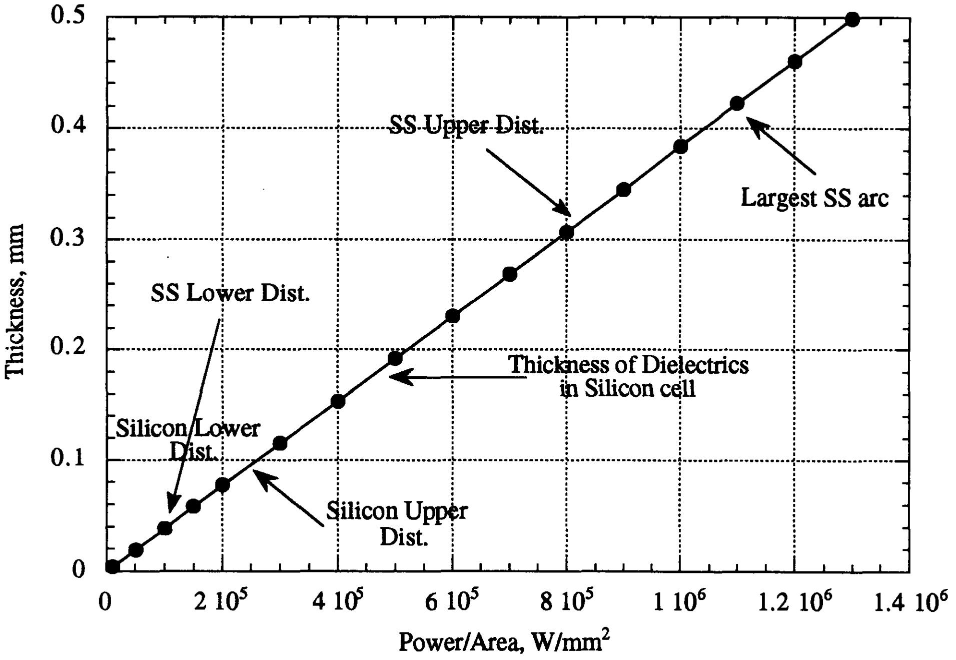

Figure 5.36: Depth of Dielectric Affected as a function of Power per Area

not be determined from the data, but the overhang seemed to reduce the arcing activity. Lastly, a comparison of the power per area obtained in the two type of cells indicated that the arcs incurred in the SS cells were stronger than those observed in the silicon cells.

Chapter 6

Conclusions

In the future, high power demands may require the operation of solar cells at higher voltages. The operation at high negative voltages in the ionospheric plasma, however, could lead to arcing. Arcing is detrimental to the operation of the cells by inducing power losses, cell damage, and EMI which may affect nearby experiments. Arcing has been observed in both ground and flight experiments. Recent flight experiments have been designed to study the interactions between different solar cells and the plasma environment. The SAMPIE experiment, sponsored by NASA, was flown in March 1994 on board the STS-62. This experiment studied the arcing behavior of different cells and materials likely to be exposed to the ionospheric plasma in future space missions. The samples biased included standard silicon, APSA, and the WTC cells to be used in the Space Station. A set of metal samples with Kapton strips was included to study the metal/insulator geometry found at the triple junction of conventional solar cells. Several arc mitigation strategies such as varying the overhang distance and the length of the side surface covered with adhesive, were also studied. The HVSA experiment conducted in May, 1995 was developed by ISAS to demonstrate the operation of high voltages in space. This experiment was the first designed to use its own array voltage instead of a power supply. This experiment biased two sets of standard silicon cells: one covered with a covered with the conventional coating and the other with a conductive coating.

Several theories have been proposed to explain the arcing mechanism in conventional geometry and WTC cells. Cho and Hastings [4] proposed an explanation for the arcing onset mechanism and simulated it using a particle in cell numerical code. Furthermore, Cho developed a theoretical analysis based on the idea of the arcs being driven by a build up of the electric field at the triple junction and the subsequent gas breakdown of desorbed neutrals. This analysis, complemented by the numerical results, yielded an expression for the time between arcs, τ_{chrg} given by Eqn. 2.27 and a neutral density at an emission site in the conductor given by Eqn. 2.28. A semi-analytical code was then developed by Cho and Hastings [4] based on these expressions and predicted accurately the arcing activity on the PIXII flight experiment. This code was then modified by Soldi and Hastings [39]who modeled the physics more accurately and included experimental limitations, such as the current threshold. Font [10] proposed an arcing mechanism for the WTC cells based on a build up of the electric field at the triple junction close to the substrate and breakdown of desorbed neutrals, similar to that of the conventional cells.

The code based on the semi-analytical model was used to simulate the arc rates in the silicon, APSA, and metal samples biased during the SAMPIE experiment. The environmental parameters used in these simulations and the data analysis were those recorded during the experiment. The plasma density and electron temperature values obtained from the Langmuir probe during the ram portion of the experiment did not agree with the values expected from a moderately sized probe in a flowing plasma. Both the plasma densities and temperatures were higher than expected. Therefore, correction factors for the ram orientation were calculated based on the agreement between the IRI-86 model and ionosonde measurements performed during the flight [8]. These corrected plasma densities and temperatures were used for the predictions during the ram portion of the experiment. The values for these parameters in the bay-to-deep space orientation were calculated using the IRI-86 model included in the EWB software package. In general, the predicted rates for the SAMPIE experiment modeled accurately the arcing activity at the lower voltages, below -300 V, while it underpredicted the arcing for some of the metal samples at the higher voltages.

In the operation of the HVSA experiment, the circuit is shorted once an arc occurs over a threshold value of 300 mA. In this case, the arcing activity is better represented as the probability of an arc occurring during a given time, rather than an arcing rate. The semi-analytical code was used to predict the arcing activity for the conventional coating cells for the different bias voltages. No arcing was predicted for at -60 V and -120 V. In conditions conducive to maximum arcing activity, the cells biased at -180 V and -240 V exhibited arcing.

In the data analysis of the SAMPIE experiment, correlations between the arc rate and material and geometric properties, environmental and operational parameters were studied. These correlations helped to verify the validity of the semi-analytical model. The limited data obtained for the Silicon, APSA, and WTC cells allowed only qualitative comparisons to be made. The relatively larger number of data points for the metal coupons allowed a quantitative analysis

Error bars were assigned to the data points assuming that the occurrence of arcs is unrelated. For arc counts lower than 10 the standard deviation was calculated using Poisson statistics. For arc counts higher than 10, whenever possible, the error bars were calculated assuming a Gaussian distribution.

Arcing was observed in the standard silicon, APSA, and WTC cells and in the metal samples. Although the data for the silicon and APSA cells was limited, the data suggests that the APSA cells will arc more. Assuming that the arc rate varies linearly with the cell area, the arcing activity in the WTC cells was much lower than that of the silicon cells. Therefore, even though the WTC cell design has not completely suppressed arcing, it seems to have reduced the arcing activity dramatically. A comparison of the strength of the arcs observed in the silicon an WTC cells showed that the arcs in the WTC cells cause more damage. The set of modified SS cells allowed the effect of cell area and of the overhang to the studied. No cell area dependence could be drawn from the data, but the overhang seemed to reduce the arc rate.

The dependencies of the arc rate on the various parameters were studied in the metal coupon data. No dependency on cell temperature was supported by the data. This is probably due to the limited range of cell temperatures. A cell temperature dependency has been observed in the PASP Plus experiment where the cell temperature range was much larger. The dependency on the ion flux and neutral density could not be studied separately because there were only two distinct populations: high values of ion flux and neutral density while in ram, and low values whille in the bay-to-deep-space orientation. The data supports the existence of a critical neutral density and ion flux, and that as both of these parameters increase the arc rate also increases. The critical ion flux shown by the data does not agree with that predicted from the model. Using the expression for this flux, the identical critical ion flux at -400 V and -500 V suggests that the voltage drop during an arc is constant for these voltages.

There is a clear dependency between the arc rate and bias voltage. The arc rate is zero for the lower voltages and at some voltage it increases sharply. The only difference between the metal coupons is the work function of the interconnector material. The model predicts the arcing rate will be lower for interconnectors with higher work functions and that this behavior is more pronounced at the lower voltages where the τ_{efee} term dominates. This predicted behavior is supported by the flight data at voltages below -270 V.

The arc rate as a function of bias voltage was fitted using three different functional forms. The power law functional form was previously used by Ferguson to study the PIX II flight data. The other functional forms were derived from the model: at the lower voltages the arc rate is expected to vary exponentially, and at the higher voltages where the ion charging time may no longer be neglected, the data was fit using the functional form suggested by

Eqn. 2.27. All the functional forms provided good fits. It is important to note that the last two forms showed an onset voltage at approximately -180 V which is supported by the data. The coefficients obtained from the fits suggested by the model could not be interpreted physically. Yet, if these coefficients were scaled with respect to work function or ion flux, they predict the arcing activity very well.

Thus, two different methods may be used to predict the arcing activity for a given solar cell. If experimental data is available for that cell at a different ion flux or with a different interconnector, the coefficients of the fitted data may be scaled to predict the arc rates. The second method is to use the semi-analytical code. The code can predict the arc rates for any conventional cell under varying environmental conditions. The code predicts the arc rates at the lower voltages accurately. However, it seems to underpredict the arc rates at the high voltages for some of the cells.

6.1 Suggestions for SAMPIE reflight

Based on the above data analysis several suggestions may be made for the SAMPIE reflight, scheduled in 1997.

(1) To repeat as many experiments as possible, thus increasing the statistical significance. A larger number of data points would allow a measure of the statistical fluctuations to be made, especially at the higher voltages. A larger number of runs would also allow the onset voltage to be determined with certainty.

(2) To decrease the experiment time at each voltage to about one or two minutes. The cells were biased at -120 V for 30 minutes and at -180 V for 20 minutes. These times are equivalent to about one third of the orbit, and the variation in the environmental conditions was large.

(3) To increase the range of cell temperatures to allow the dependency between the arc rate and this parameter to be studied. This may require the use of active temperature control.

(4) If possible, bias the cells at higher voltages. This will allow the decreasing slope of the Cho/Hastings fit at the high voltages to be verified.

Appendix A

SAMPIE Experimental Data

The following tables contain the data used in the arc rate predictions and data analysis of the cells biased during the SAMPIE experiment. Most of this data is the raw data from the experiment. The plasma density and temperatures in the ram orientation have already been corrected using the correction factors described in Chapter 4. Since the plasma density and temperatures in the bay-to-deep-space orientation were not available from the experiment, they were recreated using the EWB sofware package. Each table contains the following variables:

- MET Start Time from Day 6 in the Mission. Day 6 corresponds to March 10, 1994 at 8:57 am.
- Dwell Time: Time spent at a particular bias voltage
- Bias Voltage
- Cell Type:

siG0	Four 2 cm × 2 cm silicon solar cells
apsa	Twelve 2 cm × 4 cm APSA solar cells
coppk	1 inch square copper sample covered with strips of Kapton
tungk	1 inch square tungsten sample covered with strips of Kapton
goldk	1 inch square gold sample covered with strips of Kapton
alumk	1 inch square aluminum sample covered with strips of Kapton
silvk	1 inch square silver sample covered with strips of Kapton
SS	Baseline 8 cm × 8 cm Space Station cells
SSMIN1,4	Cut down SS cell, 3.5 cm × 3.5 cm. 32 mils of edge coating removed
SSMIN2	Four Cut down SS cells shorted together as a single experiment
SSMIN3,1	Cut down SS cell, 3.5 cm × 3.5 cm. No overhang
SSMIN3,4	Cut down SS cell, 3.5 cm × 3.5 cm. 11 mils of overhang

- Arc Count
- Arc Rate: Arc Count divided by the total dwell time at the bias voltage

- Exp #: Run number as given in timeline. The decimal portion indicates the number of times it was repeated.
- Angle of Attack: R Shuttle is oriented bay-to-ram
  W Shuttle is oriented bay-to-wake
  D Shuttle is oriented bay-to-deep-space
- Plasma Density
- Electron Temperature
- V-body Probe: Potential of Orbiter with respect to ambient plasma
- Sun Sensor Reading: $\sim$9.4 Volts cells in sunlight
  $\sim$0.0 Volts cells in eclipse
- Neutral Pressure
- Cell Temperature
- Goodness: B (bad) point is considered an outlier
  G (good) point was used for predictions and data analysis

Environmental Parameters for Negative Biasing for Silicon and APSA Cells

MET (min) from Day 6	Dwell (min)	Voltage	Cell type	Count	Arc Rate (arcs/s)	Exp #	AoA	e- Dens (/m^3)	Te (eV)	Vbody (V)	sun (V)	pressure (micro-Torr)	Cell Temp. C	Quality
1765	1	30	apsa	0	0.0000	31.01	R	1.06E+11	0.1253	-0.1709	9.4104	2.49	-3	G
1766	1	60	apsa	0	0.0000	31.01	R	1.32E+11	0.1769	-0.0244	9.4116	2.50	-3	G
1767	1	90	apsa	0	0.0000	31.01	R	1.85E+11	0.1603	0.0610	9.4092	2.52	-3	G
1768	3	120	apsa	0	0.0000	31.01	R	3.76E+11	0.1396	0.1221	9.4080	2.70		G
1771	3	120	apsa	0	0.0000	31.01	R	4.75E+11	0.1508	-0.0977	9.4092	2.64		G
1774	3	120	apsa	0	0.0000	31.01	R	5.69E+11	0.1605	-0.1465	9.4116	2.73		G
1777	3	120	apsa	0	0.0000	31.01	R	8.08E+11	0.1421	-0.1465	9.4128	2.77		G
1780	3	120	apsa	0	0.0000	31.01	R	1.12E+12	0.1381	-0.1465	9.4043	2.82		G
1783	3	120	apsa	0	0.0000	31.01	R	1.23E+12	0.1313	-0.0488	9.2554	2.85		G
1786	3	120	apsa	0	0.0000	31.01	R	1.58E+12	0.1200	0.0000	8.6658	2.64		G
1789	3	120	apsa	0	0.0000	31.01	R	1.68E+12	0.1302	0.0000	8.3655	2.70		G
1792	3	120	apsa	0	0.0000	31.01	R	1.37E+12	0.1304	0.0977	8.7732	2.70	N/A	G
1795	3	120	apsa	0	0.0000	31.01	R	1.20E+12	0.1307	0.2441	9.0479	0.00		G
1798	3	150	apsa	0	0.0000	31.01	R	1.57E+12	0.1231	0.5371	8.8367	2.49		G
1801	3	150	apsa	0	0.0000	31.01	R	1.69E+12	0.1295	0.4883	8.8245	2.82		G
1804	3	150	apsa	0	0.0000	31.01	R	9.10E+11	0.1295	0.4395	8.6340	2.77		G
1807	3	150	apsa	0	0.0000	31.01	R	3.72E+11	0.1861	0.3418	7.4780	2.68		G
1810	3	150	apsa	0	0.0000	31.01	R	3.39E+11	0.1356	0.2686	1.6626	2.55		G
1813	3	150	apsa	0	0.0000	31.01	R	2.94E+11	0.1113	0.1953	1.6772	2.46		G
1816	2	150	apsa	0	0.0000	31.01	R	3.80E+11	0.1067	0.2441	0.1025	2.64	3	G
1818	3	180	apsa	0	0.0000	31.01	R	2.47E+11	0.0979	0.3174	0.1025	2.36		G
1821	2	180	apsa	0	0.0000	31.01	R	2.15E+11	0.1050	0.3662	0.1025	2.82	1	G
1823	2	210	apsa	0	0.0000	31.01	R	2.02E+11	0.1179	0.4028	0.1001	2.35	1	G
1825	1	240	apsa	0	0.0000	31.01	R	2.25E+11	0.1156	0.4028	0.1013	2.34	0	G
1826	1	270	apsa	0	0.0000	31.01	R	2.26E+11	0.1036	0.4517	0.1025	2.32	0	G
1827	1	300	apsa	0	0.0000	31.01	R	2.12E+11	0.0878	0.4028	0.1025	2.35	0	G
1898	1	30	siG0	0	0.0000	33.01	R	1.19E+12	0.1168	0.5493	8.2837	2.65	8	G
1899	1	60	siG0	0	0.0000	33.01	R	6.48E+11	0.1501	0.5493	8.0444	2.61	7	G
1900	1	90	siG0	0	0.0000	33.01	R	4.07E+11	0.1946	0.5493	7.4902	2.59	7	G
1901	3	120	siG0	0	0.0000	33.01	R	2.90E+11	0.1410	0.3906	1.9714	2.51		G
1904	3	120	siG0	0	0.0000	33.01	R	2.35E+11	0.1005	0.1953	1.8127	2.55		G
1907	3	120	siG0	0	0.0000	33.01	R	2.55E+11	0.1050	0.1953	0.1025	2.61		G
1910	3	120	siG0	0	0.0000	33.01	R	2.41E+11	0.0991	0.2930	0.1025	2.57		G
1913	3	120	siG0	0	0.0000	33.01	R	1.80E+11	0.1316	0.3418	0.1025	2.51		G
1916	3	120	siG0	0	0.0000	33.01	R	1.66E+11	0.1170	0.4395	0.1025	2.51		G
1919	3	120	siG0	0	0.0000	33.01	R	1.89E+11	0.1360	0.4395	0.1025	2.51		G
1922	3	120	siG0	0	0.0000	33.01	R	2.29E+11	0.0888	0.3906	0.1025	2.52		G
1925	3	120	siG0	0	0.0000	33.01	R	4.24E+11	0.0818	0.3418	0.1025	2.54		G
1928	3	120	siG0	0	0.0000	33.01	R	4.21E+11	0.1053	0.0977	0.1025	0.00	N/A	G
1931	3	150	siG0	0	0.0000	33.01	R	1.16E+11	0.0651	-0.1221	0.1025	2.52		G
1934	3	150	siG0	0	0.0000	33.01	R	5.32E+10	0.0314	-0.3418	0.1025	2.54		G
1937	3	150	siG0	0	0.0000	33.01	R	5.27E+10	0.0632	-0.5005	0.1355	2.55		G
1940	3	150	siG0	0	0.0000	33.01	R	7.43E+10	0.0817	-0.6348	9.4287	2.54		G
1943	3	150	siG0	0	0.0000	33.01	R	1.26E+11	0.1829	-0.5371	9.4238	2.47		G
1946	3	150	siG0	0	0.0000	33.01	R	3.41E+11	0.1379	-0.3784	9.4226	2.49		G
1949	2	150	siG0	0	0.0000	33.01	R	4.93E+11	0.1344	-0.3418	9.4214	2.51	0	G
1951	3	180	siG0	0	0.0000	33.01	R	7.71E+11	0.1081	-0.1099	9.4202	2.60		G
1954	2	180	siG0	0	0.0000	33.01	R	1.01E+12	0.1271	-0.2319	9.4238	2.54	5	G
1956	2	210	siG0	0	0.0000	33.01	R	1.04E+12	0.1196	-0.0122	9.4189	2.67	7	G
1958	1	240	siG0	0	0.0000	33.01	R	1.21E+12	0.1158	0.0244	9.4189	2.69	8	G
1959	1	270	siG0	0	0.0000	33.01	R	1.36E+12	0.1039	0.0854	9.4189	2.70	10	G
1960	1	300	siG0	0	0.0000	33.01	R	1.63E+12	0.1039	0.1099	9.4141	2.72	11	G
2405	1	400	siG0	0	0.0000	48.01	R	3.26E+11	0.1782	0.0366	9.4214	1.84	1	G
2406	1	500	siG0	5	0.0833	48.01	R	4.58E+11	0.1434	0.0122	9.4226	1.87	2	G
2407	1	600	siG0	30	0.5000	48.01	R	4.73E+11	0.1287	0.0122	9.4214	1.91	4	G
2424	1	400	siG0	0	0.0000	54.01	R	6.42E+11	0.1050	0.2075	8.7830	2.58	15	G
2425	1	500	siG0	2	0.0333	54.01	R	5.91E+11	0.1257	0.2075	8.7695	2.58	15	G
2426	1	600	siG0	22	0.3667	54.01	R	6.18E+11	0.1382	0.2197	9.0112	2.58	14	G

Environmental Parameters for Negative Biasing for the Metal Coupons

MET Start Time (min from day 6)	Dwell Time	Voltage	Cell Type	Count	Arc Rate (arcs/s)	Exp #	AoA	e- Dens (/m^3)	Te (eV)	Vbody (V)	sun (V)	pressure (micro Torr)	Cell Temp. C	Quality
1830	1	30	coppk	0	0.0000	32.01	R	1.94E+11	0.1062	0.3296	0.1013	2.42	-1	G
1831	1	60	coppk	0	0.0000	32.01	R	1.96E+11	0.1116	0.2930	0.1025	2.44		G
1832	1	90	coppk	0	0.0000	32.01	R	1.94E+11	0.1100	0.2686	0.1025	2.47		G
1833	3	120	coppk	0	0.0000	32.01	R	1.70E+11	0.0999	0.1465	0.1025	2.49		G
1836	3	120	coppk	0	0.0000	32.01	R	1.24E+11	0.0989	-0.0488	0.1025	2.58		G
1839	3	120	coppk	0	0.0000	32.01	R	2.07E+11	0.0625	-0.1953	0.1025	2.56		G
1842	3	120	coppk	0	0.0000	32.01	R	1.87E+11	0.0556	-0.3418	0.1025	2.52		G
1845	3	120	coppk	0	0.0000	32.01	R	7.30E+10	0.0758	-0.4883	0.1099	2.46		G
1848	3	120	coppk	0	0.0000	32.01	R	8.98E+10	0.1024	-0.6104	4.9646	2.17		G
1851	3	120	coppk	0	0.0000	32.01	R	1.17E+11	0.1328	-0.6348	9.4189	1.20		G
1854	3	120	coppk	0	0.0000	32.01	R	2.84E+11	0.1849	-0.2930	9.4177	2.17		G
1857	3	120	coppk	0	0.0000	32.01	R	8.95E+11	0.1600	-0.1465	9.4177	2.39		G
1860	3	120	coppk	0	0.0000	32.01	R	5.66E+11	0.1278	-0.0977	9.4177	2.50	3	G
1863	3	150	coppk	0	0.0000	32.01	R	9.41E+11	0.1109	0.0488	9.4165	2.86		G
1866	3	150	coppk	0	0.0000	32.01	R	1.35E+12	0.1146	-0.0977	9.4177	2.73		G
1869	3	150	coppk	0	0.0000	32.01	R	1.44E+12	0.1085	-0.0488	9.3958	2.80		G
1872	3	150	coppk	0	0.0000	32.01	R	1.76E+12	0.1217	-0.0122	9.2517	2.84		G
1875	3	150	coppk	0	0.0000	32.01	R	1.66E+12	0.1325	0.0000	8.9905	2.84		G
1878	3	150	coppk	0	0.0000	32.01	R	1.31E+12	0.1107	0.0000	8.7756	2.85		G
1881	2	150	coppk	0	0.0000	32.01	R	1.28E+12	0.1220	0.0488	8.3521	1.20	13	G
1883	3	180	coppk	0	0.0000	32.01	R	1.37E+12	0.1227	0.3052	8.6353	2.81		G
1886	2	180	coppk	0	0.0000	32.01	R	1.46E+12	0.1248	0.2441	8.5767	2.73	11	G
1888	2	210	coppk	0	0.0000	32.01	R	2.13E+12	0.1219	0.4761	8.4155	2.78	10	G
1890	1	240	coppk	5	0.0833	32.01	R	2.61E+12	0.1193	0.5127	8.6230	2.76	10	G
1891	1	270	coppk	28	0.4667	32.01	R	3.12E+12	0.1060	0.5493	8.8037	2.74	9	G
1892	1	300	coppk	59	0.9833	32.01	R	2.65E+12	0.0991	0.5737	8.7280	2.72	9	G
2030	1	30	tungk	0	0.0000	38.01	R	1.34E+11	0.0575	-0.3662	0.3809	2.52		G
2031	1	60	tungk	0	0.0000	38.01	R	1.26E+11	0.1528	-0.3418	2.7319	2.50		G
2032	1	90	tungk	0	0.0000	38.01	R	1.33E+11	0.0738	-0.3174	8.6951	2.48		G
2033	3	120	tungk	0	0.0000	38.01	R	1.25E+11	0.1337	-0.3174	9.4238	2.84		G
2036	3	120	tungk	0	0.0000	38.01	R	1.97E+11	0.1285	-0.3906	9.4238	2.50		G
2039	3	120	tungk	0	0.0000	38.01	R	2.62E+11	0.1894	-0.2441	9.4250	2.55		G
2042	3	120	tungk	0	0.0000	38.01	R	6.08E+11	0.1337	-0.2441	9.4275	2.59		G
2045	3	120	tungk	0	0.0000	38.01	R	9.91E+11	0.1099	-0.1465	9.4226	2.68		G
2048	3	120	tungk	0	0.0000	38.01	R	1.43E+12	0.1161	-0.0977	9.4238	2.74		G
2051	3	120	tungk	0	0.0000	38.01	R	1.78E+12	0.1069	0.0000	9.3933	2.77		G
2054	3	120	tungk	0	0.0000	38.01	R	2.46E+12	0.1203	0.0000	9.2725	2.78		G
2057	3	120	tungk	0	0.0000	38.01	R	1.41E+12	0.1250	0.0488	8.5742	2.83		G
2060	3	120	tungk	0	0.0000	38.01	R	1.07E+12	0.1212	0.0488	8.3386	2.70		G
2063	3	150	tungk	0	0.0000	38.01	R	1.31E+12	0.1334	0.2563	8.4424	2.45		G
2066	3	150	tungk	0	0.0000	38.01	R	1.68E+12	0.1351	0.1953	8.3325	2.81		G
2069	3	150	tungk	0	0.0000	38.01	R	2.51E+12	0.1358	0.1709	8.3447	2.79		G
2072	3	150	tungk	0	0.0000	38.01	R	1.19E+12	0.0958	0.1953	8.6914	2.75		G
2075	3	150	tungk	0	0.0000	38.01	R	1.17E+12	0.0991	0.2930	8.6938	2.68		G
2078	3	150	tungk	0	0.0000	38.01	R	1.12E+12	0.1046	0.3906	6.9153	2.58		G
2081	2	150	tungk	0	0.0000	38.01	R	1.08E+12	0.0885	0.3784	2.7515	2.77		G
2083	3	180	tungk	1	0.0033	38.01	R	7.41E+11	0.1050	0.4395	1.7639	2.35		G
2086	2	180	tungk	1	0.0033	38.01	R	5.38E+11	0.0895	0.4395	0.1025	2.81	3	G
2088	2	210	tungk	15	0.1250	38.01	R	4.68E+11	0.0900	0.4028	0.1025	2.33	3	G
2090	1	240	tungk	44	0.7333	38.01	R	4.60E+11	0.0989	0.4395	0.1025	2.26	2	G
2091	1	270	tungk	114	1.9000	38.01	R	4.22E+11	0.1062	0.4395	0.1025	2.21	2	G
2092	1	300	tungk	120	2.0000	38.01	R	3.44E+11	0.1041	0.4395	0.1025	2.20	2	G
2163	1	30	goldk	0	0.0000	40.01	R	2.40E+12	0.0900	0.3662	8.4644	2.69	10	G
2164	1	60	goldk	0	0.0000	40.01	R	1.66E+12	0.1253	0.3540	8.4277	2.66	9	G
2165	1	90	goldk	0	0.0000	40.01	R	1.25E+12	0.0968	0.3784	8.3923	2.60	9	G
2166	3	120	goldk	0	0.0000	40.01	R	8.74E+11	0.1144	0.4395	8.5010	2.36		G
2169	3	120	goldk	0	0.0000	40.01	R	9.72E+11	0.0900	0.3418	7.4048	2.49		G
2172	3	120	goldk	0	0.0000	40.01	R	1.10E+12	0.0904	0.3418	1.6455	2.38		G
2175	3	120	goldk	0	0.0000	40.01	R	9.26E+11	0.0991	0.3906	0.8313	2.30		G
2178	3	120	goldk	0	0.0000	40.01	R	5.83E+11	0.0980	0.3418	0.1025	2.29		G
2181	3	120	goldk	0	0.0000	40.01	R	6.64E+11	0.0860	0.4395	0.1025	2.20		G
2184	3	120	goldk	0	0.0000	40.01	R	7.68E+11	0.0752	0.4761	0.1025	2.20		G
2187	3	120	goldk	0	0.0000	40.01	R	6.30E+11	0.0888	0.4883	0.1025	2.20		G
2190	3	120	goldk	0	0.0000	40.01	R	4.47E+11	0.0825	0.4395	0.1025	2.25		G
2193	3	120	goldk	0	0.0000	40.01	R	4.36E+11	0.0890	0.4517	0.1025	0.00	-1	G
2196	3	150	goldk	0	0.0000	40.01	R	5.12E+11	0.0912	0.4028	0.1025	2.13		G

MET Start Time (min from day 6)	Dwell Time	Voltage	Cell Type	Count	Arc Rate (arcs/s)	Exp #	AoA	e- Dens (/m^3)	Te (eV)	Vbody (V)	sun (V)	pressure (micro Torr)	Cell Temp. C	Quality
2199	3	150	goldk	0	0.0000	40.01	R	1.01E+12	0.0855	0.2930	0.1038	2.47		G
2202	3	150	goldk	0	0.0000	40.01	R	8.28E+11	0.0711	0.1099	0.1025	2.46		G
2205	3	150	goldk	0	0.0000	40.01	R	5.22E+11	0.0876	-0.0244	0.1025	2.50		G
2208	3	150	goldk	0	0.0000	40.01	R	1.42E+11	0.0859	-0.1953	0.1758	2.39		G
2211	3	150	goldk	0	0.0000	40.01	R	1.28E+11	0.0984	-0.3906	9.4312	2.23		G
2214	2	150	goldk	0	0.0000	40.01	R	1.18E+11	0.1342	-0.2930	9.4275	2.20	-4	G
2216	3	180	goldk	0	0.0000	40.01	R	2.32E+11	0.1556	-0.0610	9.4250	2.14		G
2219	2	180	goldk	0	0.0000	40.01	R	2.72E+11	0.1560	-0.2441	9.4263	2.47		G
2221	2	210	goldk	0	0.0000	40.01	R	3.31E+11	0.1384	-0.0610	9.4238	2.24		G
2223	1	240	goldk	4	0.0667	40.01	R	4.09E+11	0.1347	-0.0854	9.4238	2.29		G
2224	1	270	goldk	21	0.3500	40.01	R	5.37E+11	0.1389	-0.1343	9.4238	2.34	4	G
2225	1	300	goldk	65	1.0833	40.01	R	5.64E+11	0.1307	-0.1343	9.4238	2.39	5	G
2402	1	400	coppk	19	0.3167	47.01	R	1.85E+11	0.1297	0.0000	9.4202	1.85	-1	G
2403	1	500	coppk	106	1.7667	47.01	R	2.79E+11	0.1626	-0.0122	9.4214	1.84	0	G
2414	1	400	silvk	360	6.0000	51.01	R	1.10E+12	0.1099	-0.0122	9.4043	2.51		G
2415	1	500	silvk	1460	24.3333	51.01	R	1.40E+12	0.1010	0.0366	9.3787	2.55		G
2427	1	400	alumk	1269	21.1500	55.01	R	7.87E+11	0.1306	0.2563	9.1211	2.58	13	G
2428	1	500	alumk	84	1.4000	55.01	R	1.25E+12	0.1060	0.3052	9.0503	2.58	13	G
2466	1	400	tungk	299	4.9833	59.01	R	1.45E+12	0.0350	0.4028	0.1013	1.87	-1	G
2467	1	500	tungk	249	4.1500	59.01	R	9.36E+11	0.0879	0.3784	0.1013	2.00	-1	G
2479	1	400	goldk	205	3.4167	63.01	R	2.12E+11	0.0818	-0.1099	0.1025	2.12	4	G
2480	1	500	goldk	366	6.1000	63.01	R	2.19E+11	0.0488	-0.1587	0.1038	2.37	4	G
2544	1	30	silvk	0	0.0000	34.01	R	3.67E+11	0.1043	0.4761	0.1025	1.61		G
2545	1	60	silvk	0	0.0000	34.01	R	3.29E+11	0.0796	0.4883	0.1025	1.64		G
2546	1	90	silvk	0	0.0000	34.01	R	2.63E+11	0.0634	0.5005	0.1025	1.65		G
2547	3	120	silvk	0	0.0000	34.01	R	3.69E+11	0.0648	0.5249	0.1025	2.21		G
2550	3	120	silvk	0	0.0000	34.01	R	1.49E+11	0.0984	0.4395	0.1025	1.88		G
2553	3	120	silvk	0	0.0000	34.01	R	1.30E+12	0.0561	0.4883	0.1025	2.00		G
2556	3	120	silvk	0	0.0000	34.01	R	1.69E+12	0.0424	0.3906	0.1025	2.24		G
2559	3	120	silvk	0	0.0000	34.01	R	0.00E+00	0.0500	0.2563	0.1025	2.52		G
2562	3	120	silvk	0	0.0000	34.01	R	2.30E+11	0.0791	0.1465	0.1025	2.43		G
2565	3	120	silvk	0	0.0000	34.01	R	2.51E+11	0.0980	0.0000	0.1025	2.34		G
2568	3	120	silvk	0	0.0000	34.01	R	8.65E+10	0.0897	-0.2319	0.1025	2.34		G
2571	3	120	silvk	0	0.0000	34.01	R	1.18E+11	0.0707	-0.3418	0.8484	2.29		G
2574	3	120	silvk	0	0.0000	34.01	R	0.00E+00	0.1200	-0.3418	9.4287	2.40		G
2577	3	150	silvk	0	0.0000	34.01	R	2.06E+11	0.1805	0.0122	9.4226	2.51		G
2580	3	150	silvk	0	0.0000	34.01	R	3.04E+11	0.1742	-0.0977	9.4263	2.11		G
2583	3	150	silvk	0	0.0000	34.01	R	6.11E+11	0.1600	0.0000	9.4263	2.06		G
2586	3	150	silvk	0	0.0000	34.01	R	1.02E+12	0.1500	0.0488	9.4250	2.13		G
2589	3	150	silvk	0	0.0000	34.01	R	4.99E+11	0.1412	0.0977	9.4250	2.25		G
2592	3	150	silvk	0	0.0000	34.01	R	1.04E+12	0.0658	0.0488	9.4104	2.37		G
2595	2	150	silvk	0	0.0000	34.01	R	2.02E+12	0.0657	0.0122	9.3591	2.34		G
2597	3	180	silvk	11	0.0367	34.01	R	2.13E+12	0.0657	0.1831	8.5046	2.63		G
2600	2	180	silvk	11	0.0367	34.01	R	1.19E+12	0.0215	0.0366	8.2373	2.11		G
2602	2	210	silvk	90	0.7500	34.01	R	9.85E+11	0.0815	0.3174	8.3936	2.70		G
2604	1	240	silvk	137	2.2833	34.01	R	1.12E+12	0.0947	0.3540	8.4058	2.69		G
2605	1	270	silvk	182	3.0333	34.01	R	1.39E+12	0.0618	0.4028	8.4668	2.66		G
2606	1	300	silvk	217	3.6167	34.01	R	1.77E+12	0.0013	0.5005	8.3813	2.66		G
2677	1	30	alumk	0	0.0000	36.01	R	1.02E+12	0.0600	0.1465	9.4250	2.06		G
2678	1	60	alumk	0	0.0000	36.01	R	9.99E+11	0.1200	0.1953	9.4263	2.10		G
2679	1	90	alumk	0	0.0000	36.01	R	3.60E+11	0.1732	0.2075	9.4275	2.15		G
2680	3	120	alumk	0	0.0000	36.01	R	1.13E+12	0.1100	0.2930	9.4250	2.35		G
2683	3	120	alumk	0	0.0000	36.01	R	9.82E+11	0.0505	0.0488	9.4141	2.34		G
2686	3	120	alumk	0	0.0000	36.01	R	1.46E+12	0.1191	0.0488	9.3103	2.56		G
2689	3	120	alumk	0	0.0000	36.01	R	2.19E+12	0.0629	0.1221	8.8062	2.62		G
2692	3	120	alumk	0	0.0000	36.01	R	1.50E+12	0.0864	0.1953	8.7378	2.67		G
2695	3	120	alumk	0	0.0000	36.01	R	2.02E+12	0.0900	0.3418	8.2629	2.68		G
2698	3	120	alumk	0	0.0000	36.01	R	1.87E+12	0.1027	0.4395	8.5291	2.65		G
2701	3	120	alumk	0	0.0000	36.01	R	1.49E+12	0.1066	0.4761	8.7927	2.59		G
2704	3	120	alumk	0	0.0000	36.01	R	6.37E+11	0.0987	0.5127	8.3740	2.51		G
2707	3	120	alumk	0	0.0000	36.01	R	2.98E+11	0.2036	0.5249	8.4619	2.20		G
2710	3	150	alumk	0	0.0000	36.01	R	2.42E+11	0.1607	0.4150	7.6611	1.94		G
2713	3	150	alumk	0	0.0000	36.01	R	2.32E+11	0.1149	0.2197	2.4939	2.01		G
2716	3	150	alumk	0	0.0000	36.01	R	2.83E+11	0.1121	0.3052	0.9875	1.93		G
2719	3	150	alumk	0	0.0000	36.01	R	2.93E+11	0.0751	0.3418	0.1025	1.94		G
2722	3	150	alumk	0	0.0000	36.01	R	3.65E+11	0.0768	0.3906	0.1025	1.94		G
2725	3	150	alumk	0	0.0000	36.01	R	2.89E+11	0.0968	0.4883	0.1025	1.94		G
2728	2	150	alumk	0	0.0000	36.01	R	5.89E+11	0.0773	0.5859	0.1025	2.65		G

MET Start Time (min from day 6)	Dwell Time	Voltage	Cell Type	Count	Arc Rate (arcs/s)	Exp #	AoA	e- Dens (/m^3)	Te (eV)	Vbody (V)	sun (V)	pressure (micro Torr)	Cell Temp. C	Quality
2730	3	180	alumk	3	0.0100	36.01	R	0.00E+00	0.0600	0.5737	0.1025	2.12		G
2733	2	180	alumk	3	0.0100	36.01	R	1.31E+12	0.0551	0.5859	0.1025	2.01		G
2735	2	210	alumk	44	0.3667	36.01	R	1.36E+12	0.0770	0.5859	0.0977	2.05		G
2737	1	240	alumk	77	1.2833	36.01	R	1.24E+12	0.0448	0.5249	0.0977	2.07		G
2738	1	270	alumk	191	3.1833	36.01	R	9.90E+11	0.0862	0.4517	0.0989	2.08		G
2739	1	300	alumk	233	3.8833	36.01	R	1.06E+12	0.0711	0.4028	0.1025	2.04		G
2812	1	400	coppk	19	0.3167	47.02	R	1.91E+11	0.1227	0.2563	0.1025	1.87		G
2813	1	500	coppk	73	1.2167	47.02	R	1.69E+11	0.1252	0.3296	0.1025	1.88		G
2824	1	400	silvk	263	4.3833	51.02	R	2.72E+11	0.0704	0.5859	0.1025	1.92		G
2825	1	500	silvk	486	8.1000	51.02	R	2.62E+11	0.0691	0.5615	0.1025	1.95		G
2837	1	400	alumk	462	7.7000	55.02	R	4.18E+11	0.1182	0.2197	0.1025	2.24		G
2838	1	500	alumk	1009	16.8167	55.02	R	3.30E+11	0.0761	0.1953	0.1025	2.22		G
2850	1	400	tungk	37	0.6167	59.02	R	2.07E+11	0.1113	-0.1343	9.4263	2.14		G
2851	1	500	tungk	131	2.1833	59.02	R	2.18E+11	0.1490	-0.0977	9.4250	2.16		G
2862	1	400	goldk	425	7.0833	63.02	R	5.12E+11	0.1417	0.1953	9.4250	2.42		G
2863	1	500	goldk	408	6.8000	63.02	R	6.47E+11	0.1358	0.2441	9.4250	2.47		G
2940	1	400	coppk	0	0.0000	47.03	W	0.00E+00	0.0000	0.0000	0.5151	0.72		G
2941	1	500	coppk	0	0.0000	47.03	W	0.00E+00	0.0000	0.0000	1.2402	0.71		G
2952	1	400	silvk	0	0.0000	51.03	W	0.00E+00	0.0000	0.0000	9.4128	0.68		G
2953	1	500	silvk	0	0.0000	51.03	W	0.00E+00	0.0000	0.0000	9.4177	0.68		G
2965	1	400	alumk	0	0.0000	55.03	W	3.74E+10	0.2344	0.0000	9.4165	0.68		G
2966	1	500	alumk	18	0.3000	55.03	W	6.14E+10	0.1991	0.0000	9.4141	0.69		G
2978	1	400	tungk	13	0.2167	59.03	W	4.38E+10	0.2900	0.0000	9.4141	0.68		G
2979	1	500	tungk	28	0.4667	59.03	W	0.00E+00	0.0000	0.0000	9.4141	0.68		G
2990	1	400	goldk	0	0.0000	63.03	W	0.00E+00	0.0000	0.0000	9.4116	0.75		G
2991	1	500	goldk	0	0.0000	63.03	W	0.00E+00	0.0000	0.0000	8.9673	0.75		G
3344	1	400	coppk	0	0.0000	47.04	W	0.00E+00	0.0000	0.0000	9.2712	0.45		G
3345	1	500	coppk	0	0.0000	47.04	W	0.00E+00	0.0000	0.0000	9.2725	0.45		G
3356	1	400	silvk	0	0.0000	51.04	W	0.00E+00	0.0000	0.0000	0.1074	0.54		G
3357	1	500	silvk	0	0.0000	51.04	W	0.00E+00	0.0000	0.0000	0.1025	0.54		G
3369	1	400	alumk	0	0.0000	55.04	W	0.00E+00	0.0000	0.0000	0.1025	0.52		G
3370	1	500	alumk	0	0.0000	55.04	W	0.00E+00	0.0000	0.0000	0.1025	0.52		G
3382	1	400	tungk	0	0.0000	59.04	W	0.00E+00	0.0000	0.0000	0.1025	0.52		G
3383	1	500	tungk	0	0.0000	59.04	W	0.00E+00	0.0000	0.0000	0.1025	0.52		G
3394	1	400	goldk	0	0.0000	63.04	W	0.00E+00	0.0000	0.0000	5.1636	0.51		G
3395	1	500	goldk	0	0.0000	63.04	W	0.00E+00	0.0000	0.0000	7.4609	0.51		G
3500	1	400	coppk	0	0.0000	47.05	W	0.00E+00	0.0000	0.0000	9.3518	0.52		G
3501	1	500	coppk	0	0.0000	47.05	W	0.00E+00	0.0000	0.0000	9.2908	0.52		G
3512	1	400	silvk	0	0.0000	51.05	W	0.00E+00	0.0000	0.0000	9.3701	0.52		G
3513	1	500	silvk	0	0.0000	51.05	W	0.00E+00	0.0000	0.0000	9.3713	0.52		G
3525	1	400	alumk	0	0.0000	55.05	W	0.00E+00	0.0000	0.0000	9.3665	0.53		G
3526	1	500	alumk	0	0.0000	55.05	W	0.00E+00	0.0000	0.0000	9.3652	0.53		G
3538	1	400	tungk	0	0.0000	59.05	W	0.00E+00	0.0000	0.0000	0.1025	0.55		G
3539	1	500	tungk	0	0.0000	59.05	W	0.00E+00	0.0000	0.0000	0.1025	0.55		G
3550	1	400	goldk	0	0.0000	63.05	W	0.00E+00	0.0000	0.0000	0.1025	0.53		G
3551	1	500	goldk	0	0.0000	63.05	W	0.00E+00	0.0000	0.0000	0.1025	0.53		G
3642	1	400	coppk	0	0.0000	47.06	W	0.00E+00	0.0000	0.0000	0.1025	0.48		G
3643	1	500	coppk	0	0.0000	47.06	W	0.00E+00	0.0000	0.0000	0.1025	0.49		G
3654	1	400	silvk	0	0.0000	51.06	W	0.00E+00	0.0000	0.0000	0.1025	0.51		G
3655	1	500	silvk	0	0.0000	51.06	W	0.00E+00	0.0000	0.0000	0.1025	0.51		G
3667	1	400	alumk	0	0.0000	55.06	W	0.00E+00	0.0000	0.0000	8.1042	0.50		G
3668	1	500	alumk	0	0.0000	55.06	W	0.00E+00	0.0000	0.0000	8.8428	0.50		G
3680	1	400	tungk	0	0.0000	59.06	W	0.00E+00	0.0000	0.0000	9.3848	0.50		G
3681	1	500	tungk	0	0.0000	59.06	W	0.00E+00	0.0000	0.0000	9.3835	0.50		G
3692	1	400	goldk	0	0.0000	63.06	W	0.00E+00	0.0000	0.0000	9.3848	0.51		G
3693	1	500	goldk	0	0.0000	63.06	W	0.00E+00	0.0000	0.0000	9.3835	0.51		G
3730	1	400	coppk	0	0.0000	47.07	W	0.00E+00	0.0000	0.0000	0.1025	0.53		G
3731	1	500	coppk	0	0.0000	47.07	W	0.00E+00	0.0000	0.0000	0.1025	0.53		G
3742	1	400	silvk	0	0.0000	51.07	W	0.00E+00	0.0000	0.0000	0.1025	0.52		G
3743	1	500	silvk	0	0.0000	51.07	W	0.00E+00	0.0000	0.0000	0.1025	0.52		G
3755	1	400	alumk	0	0.0000	55.07	W	0.00E+00	0.0000	0.0000	1.6479	0.51		G
3756	1	500	alumk	0	0.0000	55.07	W	0.00E+00	0.0000	0.0000	5.3613	0.51		G
3768	1	400	tungk	0	0.0000	59.07	W	0.00E+00	0.0000	0.0000	9.3958	0.51		G
3769	1	500	tungk	0	0.0000	59.07	W	0.00E+00	0.0000	0.0000	9.3945	0.50		G
3780	1	400	goldk	0	0.0000	63.07	W	0.00E+00	0.0000	0.0000	9.3933	0.50		G
3781	1	500	goldk	0	0.0000	63.07	W	0.00E+00	0.0000	0.0000	9.3945	0.50		G
3821	1	400	coppk	0	0.0000	47.08	W	0.00E+00	0.0000	0.0000	0.1025	0.56		G
3822	1	500	coppk	2	0.0333	47.08	W	0.00E+00	0.0000	0.0000	0.1025	0.56		G

MET														
Start Time	Dwell	Voltage	Cell Type	Count	Arc Rate	Exp #	AoA	e- Dens	Te	Vbody	sun	pressure	Cell	Quality
(min from	Time				(arcs/s)			(/m^3)	(eV)	(V)	(V)	(micro	Temp.	
day 6)												Torr)	C	
3834	1	400	silvk	0	0.0000	51.08	W	0.00E+00	0.0000	0.0000	0.1013	0.56		G
3835	1	500	silvk	0	0.0000	51.08	W	0.00E+00	0.0000	0.0000	0.1013	0.56		G
3847	1	400	alumk	0	0.0000	55.08	W	0.00E+00	0.0000	0.0000	5.6921	0.55		G
3848	1	500	alumk	0	0.0000	55.08	W	0.00E+00	0.0000	0.0000	7.5964	0.55		G
3859	1	400	tungk	0	0.0000	59.08	W	0.00E+00	0.0000	0.0000	9.4031	0.55		G
3860	1	500	tungk	0	0.0000	59.08	W	0.00E+00	0.0000	0.0000	9.4019	0.55		G
3872	1	400	goldk	5	0.0833	63.08	W	0.00E+00	0.0000	0.0000	9.4006	0.54		G
3873	1	500	goldk	9	0.1500	63.08	W	0.00E+00	0.0000	0.0000	9.3994	0.55		G
5053	1	400	coppk	0	0.0000	47.09	W	0.00E+00	0.0000	0.0000	9.3262	0.41		G
5054	1	500	coppk	3	0.0500	47.09	W	0.00E+00	0.0000	0.0000	9.3201	0.41		G
5066	1	400	silvk	0	0.0000	51.09	W	0.00E+00	0.0000	0.0000	9.2981	0.44		G
5067	1	500	silvk	0	0.0000	51.09	W	0.00E+00	0.0000	0.0000	9.2981	0.44		G
5078	1	400	alumk	0	0.0000	55.09	W	0.00E+00	0.0000	0.0000	0.1025	0.46		G
5079	1	500	alumk	0	0.0000	55.09	W	0.00E+00	0.0000	0.0000	0.1025	0.46		G
5091	1	400	tungk	0	0.0000	59.09	W	0.00E+00	0.0000	0.0000	0.1025	0.46		G
5092	1	500	tungk	0	0.0000	59.09	W	0.00E+00	0.0000	0.0000	0.1025	0.46		G
5104	1	400	goldk	0	0.0000	63.09	W	0.00E+00	0.0000	0.0000	0.1025	0.46		G
5105	1	500	goldk	0	0.0000	63.09	W	0.00E+00	0.0000	0.0000	0.1025	0.46		G
5476	1	400	coppk	70	1.1667	47.10	D	1.99E+11	0.3128	0.0000	9.3384	0.89		B
5477	1	500	coppk	531	8.8500	47.10	D	4.09E+11	0.6042	0.0000	9.3945	1.31		B
5489	1	400	silvk	784	13.0667	51.10	D	2.04E+12	0.2878	0.0000	9.4043	1.95		B
5490	1	500	silvk	802	13.3667	51.10	D	2.08E+12	0.4962	0.0000	9.4031	1.91		B
5501	1	400	alumk	2114	35.2333	55.10	D	3.06E+12	0.2640	0.0000	9.1089	1.84		B
5502	1	500	alumk	3397	56.6167	55.10	D	2.56E+12	0.2385	0.0000	9.1309	1.70		B
5514	1	400	tungk	8	0.1333	59.10	D	1.85E+11	0.2962	0.0000	7.3840	0.66		B
5515	1	500	tungk	83	1.3833	59.10	D	3.72E+11	0.3228	0.0000	6.9177	0.85		B
5527	1	400	goldk	255	4.2500	63.10	D	5.62E+11	0.4082	0.0000	0.1038	2.52		B
5528	1	500	goldk	302	5.0333	63.10	D	9.47E+10	0.2944	0.0000	0.1025	2.75		B
6033	1	400	coppk	1	0.0167	47.11	D	1.61E+11	0.2019	0.0000	9.3030	0.83		G
6034	1	500	coppk	13	0.2167	47.11	D	1.47E+11	0.2070	0.0000	9.3066	0.91		G
6045	1	400	silvk	52	0.8667	51.11	D	2.10E+11	0.1276	0.0000	9.3213	1.27		B
6046	1	500	silvk	96	1.6000	51.11	D	2.39E+11	0.1159	0.0000	9.3201	1.24		B
6058	1	400	alumk	34	0.5667	55.11	D	9.12E+11	0.3041	0.0000	8.4155	1.13		B
6059	1	500	alumk	94	1.5667	55.11	D	1.08E+12	0.3432	0.0000	8.6292	1.13		B
6071	1	400	tungk	0	0.0000	59.11	D	1.56E+12	0.2578	0.0000	0.0977	1.26		B
6072	1	500	tungk	8	0.1333	59.11	D	1.56E+12	0.1773	0.0000	0.0977	1.24		B
6083	1	400	goldk	28	0.4667	63.11	D	6.30E+11	0.2086	0.0000	0.0977	1.40		B
6084	1	500	goldk	103	1.7167	63.11	D	5.77E+11	0.0000	0.0000	0.0977	1.39		B
6132	1	400	coppk	0	0.0000	47.12	D	1.50E+11	0.2296	0.0000	9.3518	0.72		G
6133	1	500	coppk	3	0.0500	47.12	D	1.71E+11	0.5600	0.0000	9.3506	0.72		G
6145	1	400	silvk	4	0.0667	51.12	D	1.96E+11	0.3038	0.0000	8.8440	0.67		G
6146	1	500	silvk	18	0.3000	51.12	D	5.80E+11	0.7079	0.0000	8.4473	0.67		G
6158	1	400	alumk	0	0.0000	55.12	D	6.25E+11	0.2333	0.0000	0.0977	0.66		G
6159	1	500	alumk	2	0.0333	55.12	D	9.73E+11	0.2324	0.0000	0.0977	0.67		G
6170	1	400	tungk	1	0.0167	59.12	D	7.37E+11	0.1780	0.0000	0.0977	0.68		G
6171	1	500	tungk	12	0.2000	59.12	D	9.17E+11	0.2181	0.0000	0.0977	0.69		G
6183	1	400	goldk	0	0.0000	63.12	D	8.37E+11	0.1904	0.0000	0.0977	0.66		G
6184	1	500	goldk	0	0.0000	63.12	D	3.10E+11	0.4929	0.0000	0.0977	0.65		G
6226	1	400	coppk	0	0.0000	47.13	D	2.80E+11	0.5509	0.0000	9.3640	0.68		G
6227	1	500	coppk	3	0.0500	47.13	D	2.41E+11	0.1992	0.0000	9.3628	0.68		G
6238	1	400	silvk	0	0.0000	51.13	D	2.81E+11	0.6399	0.0000	8.9636	0.66		G
6239	1	500	silvk	6	0.1000	51.13	D	8.16E+11	0.8354	0.0000	8.5181	0.66		G
6251	1	400	alumk	0	0.0000	55.13	D	8.95E+11	0.2343	0.0000	0.0977	0.66		G
6252	1	500	alumk	0	0.0000	55.13	D	1.09E+12	0.2441	0.0000	0.0977	0.66		G
6264	1	400	tungk	5	0.0833	59.13	D	8.85E+11	0.5382	0.0000	0.0977	0.67		G
6265	1	500	tungk	22	0.3667	59.13	D	7.28E+11	0.2018	0.0000	0.0977	0.68		G
6277	1	400	goldk	0	0.0000	63.13	D	6.71E+11	0.2300	0.0000	0.1611	0.66		G
6278	1	500	goldk	0	0.0000	63.13	D	2.44E+11	0.4779	0.0000	4.6973	0.66		G
6380	1	400	coppk	2	0.0333	47.14	D	2.24E+11	0.3010	0.0000	8.8501	0.65		G
6381	1	500	coppk	9	0.1500	47.14	D	5.14E+11	0.2886	0.0000	8.8989	0.65		G
6393	1	400	silvk	5	0.0833	51.14	D	5.82E+11	0.2630	0.0000	9.3787	0.47		G
6394	1	500	silvk	38	0.6333	51.14	D	2.99E+11	0.2591	0.0000	9.3738	0.50		G
6406	1	400	alumk	4	0.0667	55.14	D	2.49E+11	0.2535	0.0000	9.3628	0.65		G
6407	1	500	alumk	44	0.7333	55.14	D	2.51E+11	0.9149	0.0000	9.3640	0.65		G
6419	1	400	tungk	1	0.0167	59.14	D	2.93E+11	0.2058	0.0000	8.8147	0.64		G
6420	1	500	tungk	2	0.0333	59.14	D	9.33E+11	0.7152	0.0000	0.6396	0.64		G
6431	1	400	goldk	0	0.0000	63.14	D	1.04E+12	0.2638	0.0000	0.0977	0.64		G
6432	1	500	goldk	0	0.0000	63.14	D	4.42E+11	0.6023	0.0000	0.0977	0.64		G

MET														
Start Time	Dwell	Voltage	Cell Type	Count	Arc Rate	Exp #	AoA	e- Dens	Te	Vbody	sun	pressure	Cell	Quality
(min from	Time				(arcs/s)			(/m^3)	(eV)	(V)	(V)	(micro	Temp.	
day 6)												Torr)	C	
6501	1	400	coppk	0	0.0000	47.15	D	4.38E+11	0.2263	0.0000	9.3481	0.63		G
6502	1	500	coppk	1	0.0167	47.15	D	5.04E+11	0.2230	0.0000	9.0076	0.63		G
6514	1	400	silvk	0	0.0000	51.15	D	5.70E+11	0.7703	0.0000	0.0977	0.63		G
6515	1	500	silvk	0	0.0000	51.15	D	1.34E+12	0.2817	0.0000	0.0977	0.63		G
6526	1	400	alumk	8	0.1333	55.15	D	1.27E+12	0.5086	0.0000	0.0977	0.64		G
6527	1	500	alumk	56	0.9333	55.15	D	1.52E+12	0.1826	0.0000	0.0989	0.65		G
6539	1	400	tungk	0	0.0000	59.15	D	1.72E+12	0.1777	0.0000	0.0977	0.63		G
6540	1	500	tungk	4	0.0667	59.15	D	9.83E+11	0.7716	0.0000	0.0977	0.63		G
6552	1	400	goldk	3	0.0500	63.15	D	9.19E+11	0.2584	0.0000	8.0591	0.60		G
6553	1	500	goldk	15	0.2500	63.15	D	2.58E+11	0.2420	0.0000	8.3496	0.60		G
7300	1	400	coppk	559	9.3167	47.16	D	2.42E+11	0.3322	0.0000	8.5315	1.41		B
7301	1	500	coppk	714	11.9000	47.16	D	2.62E+12	0.3139	0.0000	8.4119	1.26		B
7313	1	400	silvk	464	7.7333	51.16	D	5.32E+11	0.3031	0.0000	0.8789	1.72		B
7314	1	500	silvk	576	9.6000	51.16	D	7.07E+11	0.4427	0.0000	0.1953	1.80		B
7325	1	400	alumk	226	3.7667	55.16	D	4.08E+11	0.2788	0.0000	0.1025	15.05		B
7326	1	500	alumk	820	13.6667	55.16	D	3.28E+11	0.2534	0.0000	0.1025	2.61		B
7338	1	400	tungk	154	2.5667	59.16	D	1.41E+12	0.2488	0.0000	0.1074	2.79		B
7339	1	500	tungk	641	10.6833	59.16	D	2.43E+12	0.3098	0.0000	0.1074	2.84		B
7351	1	400	goldk	60	1.0000	63.16	D	2.68E+11	0.3611	0.0000	0.2332	2.40		B
7352	1	500	goldk	160	2.6667	63.16	D	3.67E+11	0.2572	0.0000	2.5208	2.37		B
8330	1	400	coppk	2	0.0333	47.17	D	6.89E+10	0.2593	0.0000	0.1038	6.65		B
8331	1	500	coppk	9	0.1500	47.17	D	1.27E+11	0.7272	0.0000	0.1025	6.47		B
8343	1	400	silvk	17	0.2833	51.17	D	7.56E+08	0.1128	0.0000	7.3425	2.87		B
8344	1	500	silvk	114	1.9000	51.17	D	1.32E+09	0.0906	0.0000	7.7686	1.03		B
8355	1	400	alumk	22	0.3667	55.17	D	0.00E+00	0.0000	0.0000	9.3005	0.63		G
8356	1	500	alumk	38	0.6333	55.17	D	0.00E+00	0.0000	0.0000	9.3018	0.62		G

Environmental Parameters for Negative Biasing for the WTC Cells

MET Start Time (min) from Day 6	Dwell Time	Voltage (-V)	Cell Type	Count	Arc Rate (arcs/s)	Exp #	AoA	e- Dens (/m^3)	Te (eV)	Vbody (V)	sun (V)	pressure (micro Torr)	Cell Temp. C	Quality
1831	1	30	SS	0	0.0000	32.01	R	1.94E+11	0.1062	0.330	0.101	2.42		G
1832	1	60	SS	0	0.0000	32.01	R	1.96E+11	0.1116	0.293	0.103	2.44		G
1833	1	90	SS	0	0.0000	32.01	R	1.94E+11	0.1100	0.269	0.103	2.47		G
1837	3	120	SS	0	0.0000	32.01	R	1.70E+11	0.0999	0.147	0.103	2.49		G
1840	3	120	SS	0	0.0000	32.01	R	1.24E+11	0.0989	-0.049	0.103	2.58		G
1843	3	120	SS	0	0.0000	32.01	R	2.07E+11	0.0625	-0.195	0.103	2.56		G
1846	3	120	SS	0	0.0000	32.01	R	1.87E+11	0.0556	-0.342	0.103	2.52		G
1849	3	120	SS	0	0.0000	32.01	R	7.30E+10	0.0758	-0.488	0.110	2.46		G
1852	3	120	SS	0	0.0000	32.01	R	8.98E+10	0.1024	-0.610	4.965	2.17		G
1855	3	120	SS	0	0.0000	32.01	R	1.17E+11	0.1328	-0.635	9.419	1.20		G
1858	3	120	SS	0	0.0000	32.01	R	2.84E+11	0.1849	-0.293	9.418	2.17		G
1861	3	120	SS	0	0.0000	32.01	R	8.95E+11	0.1600	-0.147	9.418	2.39		G
1864	3	120	SS	0	0.0000	32.01	R	5.66E+11	0.1278	-0.098	9.418	0.00		G
1867	3	150	SS	0	0.0000	32.01	R	9.41E+11	0.1109	0.049	9.417	2.86		G
1870	3	150	SS	0	0.0000	32.01	R	1.35E+12	0.1146	-0.098	9.418	2.73		G
1873	3	150	SS	0	0.0000	32.01	R	1.44E+12	0.1085	-0.049	9.396	2.80		G
1876	3	150	SS	0	0.0000	32.01	R	1.76E+12	0.1217	-0.012	9.252	2.84		G
1880	3	150	SS	0	0.0000	32.01	R	1.66E+12	0.1325	0.000	8.991	2.84		G
1883	3	150	SS	0	0.0000	32.01	R	1.31E+12	0.1107	0.000	8.776	2.85		G
1885	2	150	SS	0	0.0000	32.01	R	1.28E+12	0.1220	0.049	8.352	1.20		G
1888	3	180	SS	0	0.0000	32.01	R	1.37E+12	0.1227	0.305	8.635	2.81		G
1890	2	180	SS	0	0.0000	32.01	R	1.46E+12	0.1248	0.244	8.577	2.73		G
1892	2	210	SS	0	0.0000	32.01	R	2.13E+12	0.1219	0.476	8.416	2.78		G
1893	1	240	SS	0	0.0000	32.01	R	2.61E+12	0.1193	0.513	8.623	2.76		G
1894	1	270	SS	0	0.0000	32.01	R	3.12E+12	0.1060	0.549	8.804	2.74		G
1895	1	300	SS	0	0.0000	32.01	R	2.65E+12	0.0991	0.574	8.728	2.72		G
2031	1	30	SSMIN1,1	0	0.0000	38.01	R	1.34E+11	0.0575	-0.366	0.381	2.52		G
2032	1	60	SSMIN1,1	0	0.0000	38.01	R	1.26E+11	0.1528	-0.342	2.732	2.50		G
2033	1	90	SSMIN1,1	0	0.0000	38.01	R	1.33E+11	0.0738	-0.317	8.695	2.48		G
2036	3	120	SSMIN1,1	0	0.0000	38.01	R	1.25E+11	0.1337	-0.317	9.424	2.84		G
2039	3	120	SSMIN1,1	0	0.0000	38.01	R	1.97E+11	0.1285	-0.391	9.424	2.50		G
2042	3	120	SSMIN1,1	0	0.0000	38.01	R	2.62E+11	0.1894	-0.244	9.425	2.55		G
2045	3	120	SSMIN1,1	0	0.0000	38.01	R	6.08E+11	0.1337	-0.244	9.428	2.59		G
2048	3	120	SSMIN1,1	0	0.0000	38.01	R	9.91E+11	0.1099	-0.147	9.423	2.68		G
2051	3	120	SSMIN1,1	0	0.0000	38.01	R	1.43E+12	0.1161	-0.098	9.424	2.74		G
2054	3	120	SSMIN1,1	0	0.0000	38.01	R	1.78E+12	0.1069	0.000	9.393	2.77		G
2057	3	120	SSMIN1,1	0	0.0000	38.01	R	2.46E+12	0.1203	0.000	9.273	2.78		G
2061	3	120	SSMIN1,1	0	0.0000	38.01	R	1.41E+12	0.1250	0.049	8.574	2.83		G
2064	3	120	SSMIN1,1	0	0.0000	38.01	R	1.07E+12	0.1212	0.049	8.339	0.00		G
2067	3	150	SSMIN1,1	N/A	N/A	38.01	R	1.31E+12	0.1334	0.256	8.442	2.45		G
2070	3	150	SSMIN1,1	N/A	N/A	38.01	R	1.68E+12	0.1351	0.195	8.333	2.81		G
2073	3	150	SSMIN1,1	N/A	N/A	38.01	R	2.51E+12	0.1358	0.171	8.345	2.79		G
2076	3	150	SSMIN1,1	N/A	N/A	38.01	R	1.19E+12	0.0958	0.195	8.691	2.75		G
2079	3	150	SSMIN1,1	N/A	N/A	38.01	R	1.17E+12	0.0991	0.293	8.694	2.68		G
2082	3	150	SSMIN1,1	N/A	N/A	38.01	R	1.12E+12	0.1046	0.391	6.915	2.58		G
2084	2	150	SSMIN1,1	N/A	N/A	38.01	R	1.08E+12	0.0885	0.378	2.752	2.77		G
2087	3	180	SSMIN1,1	N/A	N/A	38.01	R	7.41E+11	0.1050	0.440	1.764	2.35		G
2089	2	180	SSMIN1,1	N/A	N/A	38.01	R	5.38E+11	0.0895	0.440	0.103	2.81	3	G
2091	2	210	SSMIN1,1	0	0.0000	38.01	R	4.68E+11	0.0900	0.403	0.103	2.33	2	G
2092	1	240	SSMIN1,1	0	0.0000	38.01	R	4.60E+11	0.0989	0.440	0.103	2.26	3	G
2094	1	270	SSMIN1,1	0	0.0000	38.01	R	4.22E+11	0.1062	0.440	0.103	2.21	2	G
2095	1	300	SSMIN1,1	0	0.0000	38.01	R	3.44E+11	0.1041	0.440	0.103	2.20	2	G
2097	1	30	SSMIN1,4	0	0.0000	39.01	R	3.34E+11	0.0900	0.488	0.103	2.19	1	G
2098	1	60	SSMIN1,4	0	0.0000	39.01	R	2.81E+11	0.0806	0.488	0.103	2.21	1	G
2099	1	90	SSMIN1,4	0	0.0000	39.01	R	3.11E+11	0.0822	0.488	0.101	2.27	0	G
2102	3	120	SSMIN1,4	N/A	N/A	39.01	R	3.53E+11	0.0775	0.525	0.101	2.33		G
2106	3	120	SSMIN1,4	N/A	N/A	39.01	R	3.57E+11	0.0841	0.586	0.103	2.51		G
2109	3	120	SSMIN1,4	N/A	N/A	39.01	R	3.82E+11	0.0942	0.440	0.103	2.60		G
2112	3	120	SSMIN1,4	N/A	N/A	39.01	R	7.83E+11	0.0777	0.293	0.103	2.54		G
2115	3	120	SSMIN1,4	N/A	N/A	39.01	R	7.66E+11	0.0820	0.110	0.103	2.54		G
2118	3	120	SSMIN1,4	N/A	N/A	39.01	R	4.49E+11	0.0759	-0.049	0.103	2.51		G
2121	3	120	SSMIN1,4	N/A	N/A	39.01	R	1.19E+11	0.0745	-0.195	0.118	2.43		G
2124	3	120	SSMIN1,4	N/A	N/A	39.01	R	1.30E+11	0.0723	-0.391	9.081	2.38		G
2127	3	120	SSMIN1,4	N/A	N/A	39.01	R	1.53E+11	0.1339	-0.378	9.426	2.36		G
2130	3	120	SSMIN1,4	N/A	N/A	39.01	R	2.32E+11	0.1582	-0.342	9.428	0.00	N/A	G

2133	3	150	SSMIN1,4	N/A	N/A	39.01	R	3.34E+11	0.1612	-0.110	9.423	2.72		G
2136	3	150	SSMIN1,4	N/A	N/A	39.01	R	4.54E+11	0.1408	-0.244	9.428	2.41		G
2139	3	150	SSMIN1,4	N/A	N/A	39.01	R	6.29E+11	0.1290	-0.147	9.428	2.50		G
2142	3	150	SSMIN1,4	N/A	N/A	39.01	R	1.17E+12	0.0999	-0.073	9.424	2.61		G
2145	3	150	SSMIN1,4	N/A	N/A	39.01	R	1.71E+12	0.1142	0.024	9.377	2.69		G
2149	3	150	SSMIN1,4	N/A	N/A	39.01	R	1.49E+12	0.1146	0.049	9.096	2.71		G
2151	2	150	SSMIN1,4	N/A	N/A	39.01	R	9.34E+11	0.1381	0.098	8.629	2.43	15	G
2154	3	180	SSMIN1,4	0	0.0000	39.01	R	9.02E+11	0.1495	0.256	8.440	2.72		G
2156	2	180	SSMIN1,4	0	0.0000	39.01	R	9.85E+11	0.1241	0.110	8.414	2.41	24	G
2158	2	210	SSMIN1,4	0	0.0000	39.01	R	1.19E+12	0.1012	0.256	8.932	2.77	13	G
2159	1	240	SSMIN1,4	0	0.0000	39.01	R	1.33E+12	0.1248	0.256	8.743	2.77	12	G
2160	1	270	SSMIN1,4	0	0.0000	39.01	R	1.81E+12	0.1066	0.269	8.774	2.77	11	G
2161	1	300	SSMIN1,4	5	0.0833	39.01	R	2.30E+12	0.1142	0.256	8.673	2.76	11	G
2164	1	30	SSMIN3,1	0	0.0000	40.01	R	2.40E+12	0.0900	0.366	8.464	2.69	10	G
2165	1	60	SSMIN3,1	0	0.0000	40.01	R	1.66E+12	0.1253	0.354	8.428	2.66	9	G
2166	1	90	SSMIN3,1	0	0.0000	40.01	R	1.25E+12	0.0968	0.378	8.392	2.60	9	G
2169	3	120	SSMIN3,1	N/A	N/A	40.01	R	8.74E+11	0.1144	0.440	8.501	2.36		G
2172	3	120	SSMIN3,1	N/A	N/A	40.01	R	9.72E+11	0.0900	0.342	7.405	2.49		G
2175	3	120	SSMIN3,1	N/A	N/A	40.01	R	1.10E+12	0.0904	0.342	1.646	2.38		G
2178	3	120	SSMIN3,1	N/A	N/A	40.01	R	9.26E+11	0.0991	0.391	0.831	2.30		G
2181	3	120	SSMIN3,1	N/A	N/A	40.01	R	5.83E+11	0.0980	0.342	0.103	2.29		G
2184	3	120	SSMIN3,1	N/A	N/A	40.01	R	6.64E+11	0.0860	0.440	0.103	2.20		G
2187	3	120	SSMIN3,1	N/A	N/A	40.01	R	7.68E+11	0.0752	0.476	0.103	2.20		G
2190	3	120	SSMIN3,1	N/A	N/A	40.01	R	6.30E+11	0.0888	0.488	0.103	2.20		G
2193	3	120	SSMIN3,1	N/A	N/A	40.01	R	4.47E+11	0.0825	0.440	0.103	2.25		G
2197	3	120	SSMIN3,1	N/A	N/A	40.01	R	4.36E+11	0.0890	0.452	0.103	0.00	-1	G
2200	3	150	SSMIN3,1	N/A	N/A	40.01	R	5.12E+11	0.0912	0.403	0.103	2.13		G
2203	3	150	SSMIN3,1	N/A	N/A	40.01	R	1.01E+12	0.0855	0.293	0.104	2.47		G
2206	3	150	SSMIN3,1	N/A	N/A	40.01	R	8.28E+11	0.0711	0.110	0.103	2.46		G
2209	3	150	SSMIN3,1	N/A	N/A	40.01	R	5.22E+11	0.0876	-0.024	0.103	2.50		G
2212	3	150	SSMIN3,1	N/A	N/A	40.01	R	1.42E+11	0.0859	-0.195	0.176	2.39		G
2215	3	150	SSMIN3,1	N/A	N/A	40.01	R	1.28E+11	0.0984	-0.391	9.431	2.23		G
2217	2	150	SSMIN3,1	N/A	N/A	40.01	R	1.18E+11	0.1342	-0.293	9.428	2.20	-4	G
2220	3	180	SSMIN3,1	0	0.0000	40.01	R	2.32E+11	0.1556	-0.061	9.425	2.14		G
2222	2	180	SSMIN3,1	0	0.0000	40.01	R	2.72E+11	0.1560	-0.244	9.426	2.47		G
2224	2	210	SSMIN3,1	0	0.0000	40.01	R	3.31E+11	0.1384	-0.061	9.424	2.24		G
2225	1	240	SSMIN3,1	1	0.0167	40.01	R	4.09E+11	0.1347	-0.085	9.424	2.29		G
2226	1	270	SSMIN3,1	2	0.0333	40.01	R	5.37E+11	0.1389	-0.134	9.424	2.34	4	G
2228	1	300	SSMIN3,1	1	0.0167	40.01	R	5.64E+11	0.1307	-0.134	9.424	2.39	5	G
2230	1	30	SSMIN3,4	0	0.0000	41.01	R	8.22E+11	0.1260	-0.159	9.424	2.48	7	G
2231	1	60	SSMIN3,4	0	0.0000	41.01	R	8.92E+11	0.1132	-0.134	9.424	2.53	9	G
2232	1	90	SSMIN3,4	0	0.0000	41.01	R	1.03E+12	0.1066	-0.073	9.424	2.58	10	G
2235	3	120	SSMIN3,4	N/A	N/A	41.01	R	1.60E+12	0.1133	0.085	9.370	2.34		G
2238	3	120	SSMIN3,4	N/A	N/A	41.01	R	1.62E+12	0.1142	0.000	8.688	2.68		G
2242	3	120	SSMIN3,4	N/A	N/A	41.01	R	1.03E+12	0.1158	0.134	8.599	2.68		G
2245	3	120	SSMIN3,4	N/A	N/A	41.01	R	9.64E+11	0.1166	0.098	8.682	2.69		G
2248	3	120	SSMIN3,4	N/A	N/A	41.01	R	1.51E+12	0.1156	0.134	8.423	2.69		G
2251	3	120	SSMIN3,4	N/A	N/A	41.01	R	2.64E+12	0.1264	0.122	8.828	2.71		G
2254	3	120	SSMIN3,4	N/A	N/A	41.01	R	1.96E+12	0.1158	0.195	8.661	2.70		G
2257	3	120	SSMIN3,4	N/A	N/A	41.01	R	8.90E+11	0.0999	0.195	8.485	2.65		G
2260	3	120	SSMIN3,4	N/A	N/A	41.01	R	8.25E+11	0.1012	0.293	8.608	2.54		G
2263	3	120	SSMIN3,4	N/A	N/A	41.01	R	8.30E+11	0.0996	0.342	7.471	0.00	6	G
2266	3	150	SSMIN3,4	N/A	N/A	41.01	R	7.89E+11	0.0818	0.342	1.641	2.14		G
2269	3	150	SSMIN3,4	N/A	N/A	41.01	R	7.19E+11	0.0973	0.391	0.103	2.10		G
2272	3	150	SSMIN3,4	N/A	N/A	41.01	R	7.33E+11	0.0818	0.488	0.103	2.14		G
2275	3	150	SSMIN3,4	N/A	N/A	41.01	R	8.77E+11	0.0919	0.488	0.103	1.99		G
2278	3	150	SSMIN3,4	N/A	N/A	41.01	R	1.31E+12	0.0716	0.537	0.103	1.92		G
2281	3	150	SSMIN3,4	N/A	N/A	41.01	R	1.91E+12	0.0944	0.440	0.103	1.98		G
2284	2	150	SSMIN3,4	N/A	N/A	41.01	R	1.88E+12	0.0707	0.440	0.104	2.70	-1	G
2287	3	180	SSMIN3,4	0	0.0000	41.01	R	1.06E+12	0.0714	0.391	0.103	2.39		G
2289	2	180	SSMIN3,4	0	0.0000	41.01	R	8.30E+11	0.0784	0.317	0.105	2.10	-2	G
2291	2	210	SSMIN3,4	0	0.0000	41.01	R	7.55E+11	0.0799	0.281	0.103	2.37	-2	G
2292	1	240	SSMIN3,4	0	0.0000	41.01	R	7.98E+11	0.0782	0.244	0.103	2.35	-3	G
2293	1	270	SSMIN3,4	0	0.0000	41.01	R	7.65E+11	0.0897	0.208	0.103	2.33	-3	G
2294	1	300	SSMIN3,4	0	0.0000	41.01	R	6.64E+11	0.0618	0.147	0.103	12.95	-3	G
2297	1	30	SS	0	0.0000	42.01	R	4.70E+11	0.0681	0.037	0.103	2.64	-4	G
2298	1	60	SS	0	0.0000	42.01	R	3.99E+11	0.0895	-0.061	0.103	3.00	-4	G
2299	1	90	SS	0	0.0000	42.01	R	2.68E+11	0.0730	-0.110	0.103	1.56	-4	G
2302	3	120	SS	N/A	N/A	42.01	R	1.02E+11	0.1050	-0.256	0.173	2.54		G
2305	3	120	SS	N/A	N/A	42.01	R	8.51E+10	0.0909	-0.342	9.432	2.33		G
2308	3	120	SS	N/A	N/A	42.01	R	1.02E+11	0.1347	-0.195	9.429	2.13		G
2311	3	120	SS	N/A	N/A	42.01	R	2.28E+11	0.1584	-0.147	9.426	2.96		G

2314	3	120	SS	N/A	N/A	42.01	R	3.05E+11	0.1544	-0.159	9.429	1.78		G
2317	3	120	SS	N/A	N/A	42.01	R	3.08E+11	0.1713	-0.049	9.428	1.80		G
2320	3	120	SS	N/A	N/A	42.01	R	4.62E+11	0.1297	-0.147	9.429	2.04		G
2323	3	120	SS	N/A	N/A	42.01	R	6.20E+11	0.1255	-0.098	9.426	2.27		G
2326	3	120	SS	N/A	N/A	42.01	R	1.24E+12	0.1133	-0.012	9.395	2.43		G
2329	3	120	SS	N/A	N/A	42.01	R	1.14E+12	0.0932	-0.049	9.098	0.00	15	G
2333	3	150	SS	N/A	N/A	42.01	R	8.55E+11	0.1088	0.195	8.613	2.57		G
2336	3	150	SS	N/A	N/A	42.01	R	9.44E+11	0.1120	0.073	8.826	2.75		G
2339	3	150	SS	N/A	N/A	42.01	R	2.20E+12	0.1029	0.147	8.917	2.73		G
2342	3	150	SS	N/A	N/A	42.01	R	1.41E+12	0.1166	0.195	8.594	2.74		G
2345	3	150	SS	N/A	N/A	42.01	R	6.53E+11	0.1259	0.195	8.535	2.71		G
2348	3	150	SS	N/A	N/A	42.01	R	5.78E+11	0.1050	0.244	8.364	2.66		G
2350	2	150	SS	N/A	N/A	42.01	R	5.89E+11	0.0966	0.330	8.322	2.04	8	G
2353	3	180	SS	0	0.0000	42.01	R	6.67E+11	0.1064	0.501	7.068	2.32		G
2355	2	180	SS	0	0.0000	42.01	R	8.36E+11	0.0737	0.440	2.460	2.75	6	G
2357	2	210	SS	0	0.0000	42.01	R	8.17E+11	0.0846	0.415	1.659	2.26	5	G
2358	1	240	SS	0	0.0000	42.01	R	7.80E+11	0.1013	0.415	1.758	2.20	5	G
2359	1	270	SS	0	0.0000	42.01	R	7.38E+11	0.0879	0.391	0.103	2.21	4	G
2361	1	300	SS	0	0.0000	42.01	R	6.21E+11	0.0972	0.391	0.103	2.24	4	G
2399	1	400	SS	0	0.0000	46.01	R	9.19E+10	0.1741	-0.024	9.421	1.84	-4	G
2400	1	500	SS	0	0.0000	46.01	R	2.72E+11	0.1800	0.000	9.423	1.85	-3	G
2401	1	600	SS	1	0.0167	46.01	R	1.48E+11	0.1932	0.024	9.421	1.84	-3	G
2418	1	400	SS	5	0.0833	52.01	R	2.45E+12	0.1088	0.037	9.291	2.56		G
2419	1	500	SS	15	0.2500	52.01	R	1.84E+12	0.1132	0.085	9.175	2.58		G
2420	1	600	SS	18	0.3000	52.01	R	1.19E+12	0.1106	0.098	8.682	2.60		G
2464	1	400	SSMIN1,1	288	4.8000	58.01	R	9.53E+11	0.0719	0.488	0.103	1.67	0	B
2465	1	500	SSMIN1,1	1313	21.8833	58.01	R	1.56E+12	0.0603	0.488	0.103	1.71	-1	B
2466	1	600	SSMIN1,1	1547	25.7833	58.01	R	0.00E+00	0.0300	0.440	0.100	1.77	-1	B
2470	1	400	SSMIN1,4	182	3.0333	60.01	R	8.52E+11	0.0117	0.269	0.103	2.01	-2	B
2471	1	500	SSMIN1,4	1709	28.4833	60.01	R	6.29E+11	0.1053	0.232	0.103	2.05	-2	B
2472	1	600	SSMIN1,4	1778	29.6333	60.01	R	4.13E+11	0.0959	0.183	0.103	2.04	-2	B
2476	1	400	SSMIN3,1	1334	22.2333	62.01	R	5.18E+11	0.0400	0.024	0.103	2.09	-3	B
2477	1	500	SSMIN3,1	1140	19.0000	62.01	R	2.29E+11	0.0175	-0.037	0.103	2.10	-2	B
2478	1	600	SSMIN3,1	1055	17.5833	62.01	R	2.06E+11	0.0923	-0.085	0.103	2.08	4	B
2483	1	400	SSMIN3,4	879	14.6500	64.01	R	1.42E+11	0.0822	-0.208	0.117	2.29	4	B
2484	1	500	SSMIN3,4	725	12.0833	64.01	R	3.55E+11	0.0800	-0.195	0.710	2.24	-5	B
2485	1	600	SSMIN3,4	1126	18.7667	64.01	R	1.12E+11	0.0977	-0.110	3.759	2.19	-5	B
2489	1	400	SS	955	15.9167	66.01	R	1.14E+11	0.1925	-0.012	9.424	2.15	-4	B
2490	1	500	SS	38	0.6333	66.01	R	1.64E+11	0.1817	0.024	9.423	2.15		B
2491	1	600	SS	1633	27.2167	66.01	R	1.88E+11	0.1318	0.024	9.420	2.14		B
2493	1	400	SSMIN2	0	0.0000	67.01	R	1.93E+11	0.1563	0.037	9.424	2.08		G
2494	1	500	SSMIN2	2	0.0333	67.01	R	2.06E+11	0.1956	0.061	9.420	2.09		G
2505	1	400	SSMIN2	1	0.0167	71.01	R	1.33E+12	0.0735	0.012	9.412	2.57	11	G
2506	1	500	SSMIN2	8	0.1333	71.01	R	1.57E+12	0.0695	0.037	9.385	2.59		G
2612	1	30	SS	0	0.0000	35.01	R	1.75E+12	0.1142	0.562	8.518	2.65		G
2613	1	60	SS	0	0.0000	35.01	R	1.61E+12	0.1800	0.610	8.898	2.63		G
2614	1	90	SS	0	0.0000	35.01	R	1.54E+12	0.0735	0.598	8.752	2.62		G
2617	3	120	SS	N/A	N/A	35.01	R	7.90E+11	0.1008	0.598	8.438	2.20		G
2620	3	120	SS	N/A	N/A	35.01	R	2.68E+11	0.1972	0.476	8.268	2.39		G
2623	3	120	SS	N/A	N/A	35.01	R	2.84E+11	0.1146	0.293	8.002	2.15		G
2626	3	120	SS	N/A	N/A	35.01	R	3.18E+11	0.1227	0.403	4.922	2.04		G
2629	3	120	SS	N/A	N/A	35.01	R	4.24E+11	0.0794	0.403	1.608	1.92		G
2632	3	120	SS	N/A	N/A	35.01	R	6.02E+11	0.0916	0.440	0.103	1.84		G
2635	3	120	SS	N/A	N/A	35.01	R	7.23E+11	0.0568	0.452	0.103	1.88		G
2638	3	120	SS	N/A	N/A	35.01	R	7.36E+11	0.0725	0.488	0.103	1.95		G
2641	3	120	SS	N/A	N/A	35.01	R	8.18E+11	0.0916	0.586	0.103	1.95		G
2644	3	120	SS	N/A	N/A	35.01	R	1.18E+12	0.0521	0.635	0.099	2.58		G
2648	3	150	SS	N/A	N/A	35.01	R	1.49E+12	0.0765	0.586	0.096	2.15		G
2651	3	150	SS	N/A	N/A	35.01	R	1.18E+12	0.0493	0.513	0.098	2.48		G
2654	3	150	SS	N/A	N/A	35.01	R	0.00E+00	0.0600	0.342	0.103	2.49		G
2657	3	150	SS	N/A	N/A	35.01	R	2.53E+11	0.0808	0.195	0.103	2.48		G
2660	3	150	SS	N/A	N/A	35.01	R	2.83E+11	0.0618	0.049	0.103	2.42		G
2663	3	150	SS	N/A	N/A	35.01	R	3.40E+11	0.0899	-0.147	0.106	2.31		G
2665	2	150	SS	N/A	N/A	35.01	R	3.34E+11	0.1010	-0.232	0.676	1.88		G
2668	3	180	SS	0	0.0000	35.01	R	1.92E+11	0.1179	-0.293	9.428	1.97		G
2670	2	180	SS	0	0.0000	35.01	R	1.65E+11	0.1619	-0.342	9.430	2.48		G
2672	2	210	SS	0	0.0000	35.01	R	2.07E+11	0.1943	-0.012	9.424	2.01		G
2673	1	240	SS	0	0.0000	35.01	R	5.41E+11	0.1800	-0.037	9.424	2.05		G
2674	1	270	SS	0	0.0000	35.01	R	5.49E+11	0.1700	0.012	9.425	2.06		G
2675	1	300	SS	0	0.0000	35.01	R	2.67E+11	0.1675	0.037	9.425	2.02		G
2828	1	400	SS	0	0.0000	52.02	R	1.00E+11	0.0838	0.501	0.103	1.94		G
2829	1	500	SS	0	0.0000	52.02	R	4.63E+11	0.1033	0.513	0.101	1.99		G

2830	1	600	SS	0	0.0000	52.02	R	6.85E+11	0.0540	0.537	0.099	2.12		G
2847	1	400	SSMIN1,1	0	0.0000	58.02	R	1.34E+11	0.0999	-0.085	3.648	2.11		G
2848	1	500	SSMIN1,1	0	0.0000	58.02	R	1.87E+11	0.1198	-0.085	9.429	2.04		G
2849	1	600	SSMIN1,1	0	0.0000	58.02	R	1.84E+11	0.1133	-0.159	9.428	2.05		G
2853	1	400	SSMIN1,4	0	0.0000	60.02	R	2.00E+11	0.1814	-0.110	9.426	2.22		G
2854	1	500	SSMIN1,4	0	0.0000	60.02	R	1.98E+11	0.2127	-0.122	9.426	2.20		G
2855	1	600	SSMIN1,4	0	0.0000	60.02	R	2.21E+11	0.1709	-0.110	9.428	2.17		G
2860	1	400	SSMIN3,1	0	0.0000	62.02	R	1.24E+12	0.1800	-0.098	9.426	2.22		G
2861	1	500	SSMIN3,1	0	0.0000	62.02	R	4.78E+11	0.1695	-0.012	9.426	2.31		G
2862	1	600	SSMIN3,1	0	0.0000	62.02	R	4.67E+11	0.1673	0.110	9.424	2.35		G
2866	1	400	SSMIN3,4	0	0.0000	64.02	R	6.38E+11	0.1156	0.256	9.423	2.50		G
2867	1	500	SSMIN3,4	0	0.0000	64.02	R	7.58E+11	0.1212	0.293	9.414	2.47		G
2868	1	600	SSMIN3,4	0	0.0000	64.02	R	8.02E+11	0.1079	0.305	9.404	2.47		G
2872	1	400	SS	0	0.0000	66.02	R	1.30E+12	0.0900	0.403	8.604	2.55		G
2873	1	500	SS	0	0.0000	66.02	R	1.10E+12	0.0841	0.464	8.638	2.56		G
2874	1	600	SS	0	0.0000	66.02	R	1.04E+12	0.0912	0.476	8.672	2.55		G
2876	1	400	SSMIN2	1	0.0167	67.02	R	1.17E+12	0.0970	0.513	8.732	2.53		G
2877	1	500	SSMIN2	3	0.0500	67.02	R	1.19E+12	0.0820	0.549	8.682	2.46		G
2889	1	400	SSMIN2	0	0.0000	71.02	R	1.05E+12	0.0984	0.659	8.735	2.31		G
2890	1	500	SSMIN2	2	0.0333	71.02	R	8.89E+11	0.1039	0.647	8.324	2.22		G
2937	1	400	SS	0	0.0000	46.02	R	0.00E+00	N/A	1.013	0.103	0.73		G
2938	1	500	SS	0	0.0000	46.02	R	0.00E+00	N/A	1.074	0.103	0.73		G
2939	1	600	SS	0	0.0000	46.02	R	0.00E+00	N/A	1.209	0.459	0.72		G

Bibliography

[1] P. R. Bevington, D. K. Robinson, *Data Reduction and Error Analysis for the Physical Sciences*, McGraw-Hill, New York, 1992.

[2] W. S. Boyle, P. Kisliuk, and L. H. Gerner."Electrical Breakdown in high vacuum", Journal of Applied Physics, Vol. 26, pp. 720-725, 1955.

[3] M. R. Carruth, J. A. Vaughn, and P. A. Gray, "Experimental Studies on Spacecraft Arcing", presented at the 30th Aerospace Sciences Meeting and Exhibit, AIAA 92-0820, January 1992.

[4] M. Cho, "Arcing on High Voltage Solar Arrays in Low Earth Orbit: Theory and Computer Particle Simulation", Ph.D. Thesis, M.I.T., 1992.

[5] M. Cho and D. E. Hastings, "Dielectric Charging Processes and Arcing Rates of High Voltage Solar Arrays", Journal of Spacecraft and Rockets, Vol. 28, pp. 698-706, 1991.

[6] M. J. Drinkwine and D. Lichtman. "Electron stimulated desorption: a critical review", Prog. in Surf. Sci. Vol. 8, pp. 123-142, 1977.

[7] D. C. Ferguson, "The Voltage Threshold for Arcing for Solar Cells in LEO-Flight and Ground Test Results", NASA TM-87259, March 1986.

[8] D. C. Ferguson and G. B. Hillard, "In-Space Measurement of Electron Current Collection by Space Station Solar Arrays", presented at the 33rd Aerospace Sciences Meeting and Exhibit, AIAA 95-0486, January 1995.

[9] V. S. Fomenko, *Handbook of Thermoionic Properties*, Plenum Press, New York, 1966.

[10] G. I. Font, J. D. Soldi, C. Perez de la Cruz, and D. E. Hastings, "Arcing Mechanism of Wrap-Through-Contact Solar Cells", presented at the 33rd Aerospace Sciences Meeting and Exhibit, AIAA 95-0597, January 1995.

[11] H. Fujii, Y. Shibuya, T. Abe, K. Ijichi, R. Kasai, and K. Kuriki, "Laboratory Simulation of Plasma Interaction with High Voltage Solar Arrays", Proceedings of the 15th International Symposium on Space Technology Science, Kanagawa, Japan, 1986.

[12] N. T. Grier and N. John Stevens, "Plasma Interaction Experiment (PIX) Flight Results", Spacecraft Charging Technology, NASA CP-2071, pp. 295-314, 1978.

[13] O. Hachenberg and W. Brauer, "Secondary Electron Emission from Solids", Advancement in Electronics and Electron Physics, Vol. 11, pp. 413-499, 1959.

[14] D. E. Hastings and M. Cho, "Ion Drag for a Negatively Biased Solar Array in Low Earth Orbit", Journal of Spacecraft and Rockets, Vol. 27, pp. 279-284, 1990.

[15] D. E. Hastings, M. Cho, and H. Kuninaka, "The Arcing Rate for a High Voltage Solar Array: Theory, Experiments and Predictions", Journal of Spacecraft and Rockets, Vol. 29, pp. 538-554, 1992.

[16] D. E. Hastings, G. Weyl and D. Kaufman, "The Threshold Voltage for Arcing on Negatively Biased Solar Arrays", Journal of Spacecraft and Rockets, Vol. 27, pp. 539-544, 1990.

[17] D. E. Hastings, Personal Communication, 1995.

[18] B. G. Herron, J. R. Bayless and J. D. Worden, "High Voltage Solar Array Technology", Journal of Spacecraft and Rockets, Vol. 10, pp. 457, 1973.

[19] G. B. Hillard and D. C. Ferguson, "The SAMPIE Flight Experiment Final Technical Requirements Document", NASA TM-106224, 1993.

[20] G. B. Hillard and D. C. Ferguson, "The Solar Array Module Plasma Interactions Experiment (SAMPIE): Science and Technology Objectives", Journal of Spacecraft and Rockets, Vol. 30, No. 4, pp. 484-494, 1993.

[21] R. W. Hockney and J. W. Eastwood, *Computer Simulation Using Particles*, McGraw-Hill, USA, 1981.

[22] G. T. Inouye and R. C. Chaky, "Enhanced Electron Emission from Positive Dielectric/Negative Metal Configurations on Spacecraft", IEEE Trans. Nuc. Sci., Vol. NS-29, No. 6, pp. 1589-1593, 1982.

[23] G. A. Jongeward, I. Katz, M. J. Mandell and D. E. Parks, "The Role of Unneutralized Surface Ions in Negative Potential Arcing", presented at the 1985 IEEE 22nd Annual Conference, NSRE.

[24] H. Kuninaka, "Qualitative experiment of arc discharge on negatively biased solar cells", Journal of Spacecraft and Rockets, Vol. 27, pp. 665-668, 1990.

[25] H. Kuninaka and K. Kuriki. "Numerical Analysis of the interaction of a high-voltage solar array with ionospheric plasma". Journal of Spacecraft and Rockets, Vol. 24, pp. 512-517, 1987.

[26] H. Kuninaka, "Space Experiment on Plasma Interaction Caused by High Voltage Photovoltaic Power Generation", presented at the 25th Plasmadynamics and Lasers Conference, AIAA 94-2450, June 1994.

[27] P. Leung, "Characterization of EMI Generated by the Discharge of a 'Volt' Solar Array", Technical Report CR-176537, NASA, November 1985.

[28] D. R. Lide, *CRC Handbook of Chemistry and Physics 75th edition*, CRC Press, Inc., Boca Raton, 1994/95.

[29] L. Malter, Thin Film Field Emission. Phys. Rev., 50:48-58, 1936.

[30] W. L. Miller, "An Investigation of Arc Discharging on Negatively Biased Dielectric-Conductor Samples in a Plasma", Spacecraft Environment Interactions Technology Conference, 1983, NASA CP-2359, pp. 333-348.

[31] R. L. Mong, "Arcing Mitigation and Predictions for High Voltage Solar Arrays", S.M. Thesis, M.I.T., 1993.

[32] T. L. Morton, "Ionospheric Plasma Densitites and Temperatures Measured by SAMPIE", presented at the 33rd Aerospace Sciences Meeting and Exhibit, AIAA 95-0841, January 1995.

[33] H. K. Nahra, M. C. Felder, B. L. Sater, J. V. Staskus,"The Space Station Photovoltaic Panels Plasma Interaction Test Program: Test plan and results", presented at the 28th Aerospace Sciences Meeting and Exhibit, AIAA 90-0722, January 1990.

[34] D. E. Parks, G. Jongeward, I. Katz and V. A. Davis, "Threshold-Determining Mechanisms for Discharges in High-Voltage Solar Arrays", Journal of Spacecraft and Rockets, Vol. 24, pp. 367-371, 1987.

[35] P. A. Redhead, J. P. Hobson, and E. V. Kornelsen, *The Physical Basis of Ultra High Vacuum*, Chapman Hall Ltd. London, 1968.

[36] P. S. Severance and D. A. Guidice, "Investigation of Space Environmental Effects on Advanced Solar Arrays", Phillips Laboratory, US Air Force.

[37] D. B. Snyder, "Discharges on a Negatively Biased Solar Cell Array in a Charged Particle Environment", Spacecraft Environment Interactions Technology Conference, 1983, NASA CP-2359, pp. 379-388.

[38] D. B. Snyder and E. Tyree, "The Effect of Plasma on Solar Cell Array Arc Characteristics", Technical Report TM-86887, NASA, 1985.

[39] J. D. Soldi and D. E. Hastings, "Arcing Predictions for PASP PLUS Solar Arrays", Scientific Report PL-TR-94-2234, Phillips Laboratory, 1994.

[40] J.D. Soldi and D.E. Hastings, "Arc Rate Predictions and Flight Data Analysis for the PASP Plus Experiment", presented at the Space Power Workshop, Albuqurque NM, April 1995.

[41] N. J. Stevens, "Review of Interactions of Large Space Structures with the Environment, Space Systems and their Interactions with Earth's Space Environment", Progress in Aeronautics and Astronautics", Vol. 71, AIAA, Washington D. C., pp. 437-454, 1980.

[42] H. Thiemann and K. Bogus, "Anomalous Current Collection and Arcing of Solar-Cell Modules in a Simulated High-Density Low-Earth-Orbit Plasma, ESA Journal, Vol. 10, pp. 43-57, 1986.

[43] H. Thieman, R. W. Schunk and K. Bogus, "Where do negatively biased solar arrays arc?", Journal of Spacecraft and Rockets, Vol. 27, pp. 563-565, 1990.

[44] G. F. Turner and S. C. Debrock. "Large solar array design", Space Power, Vol. 8, No. 1-2, pp. 11-22, 1989.

[45] B. L. Upschulte, G. M. Weyl, W. J. Marinelli, E. Aifer, D. E. Hastings, and D. Snyder. "Significant reduction in arc frequency of negatively biased solar cells: Observations diagnostics and mitigation techniques. In SPRAT Conference, Cleveland, Ohio, May 1990. see also AIAA Paper 92-0578

[illegible]